Dynamics of open and closed classical and quantum-mechanical spin systems

Dissertation
zur Erlangung des Doktorgrades
an der Fakultät für Mathematik, Informatik und Naturwissenschaften
Fachbereich Physik
der Universität Hamburg

vorgelegt von
David Vincent Altwein

Hamburg
28.11.2021

Gutachter/innen der Dissertation:	PD. Dr. Elena Y. Vedmedenko Prof. Dr. Alexander Lichtenstein
Zusammensetzung der Prüfungskommission:	Prof. Dr. Elena Y. Vedmedenko Prof. Dr. Alexander Lichtenstein Prof. Dr. Roland Wiesendanger Dr. Thore Posske Prof. Dr. Günter Sigl
Vorsitzender der Prüfungskommission:	Prof. Dr. Günter Sigl
Datum der Disputation:	26.04.2022
Vorsitzender Fach-Promotionsausschusses PHYSIK:	Prof. Dr. Wolfgang Hansen
Leiter des Fachbereichs PHYSIK:	Prof. Dr. Michael Potthoff
Dekan der Fakultät MIN:	Prof. Dr. Heinrich Graener

Contents

Abstract

This thesis is dedicated to the theoretical and practical understanding of different influences of interactions on the statical and dynamical properties of classical and quantum spin systems. Systems of interest have been finite temperature arrays of dipolarly coupled superparamagnetic nanoparticles with uniaxial anisotropy, spin chains with short and long range exchange or dipolar interactions, as well as coupled and diagonalized quantum spins in an infinitely large environment at zero temperature, leading to relaxation behavior for the spin system.

For the case of the coupled nanoparticles, finite temperature Langevin spin dynamics in the form of stochastic Landau-Lifshitz-Gilbert-Equation simulations were employed and supplemented with analytic modelling of the phase space. The investigation of the spin chains was realized by both spin dynamical and Monte Carlo simulations as well as analytical calculations for the prediction of collinear and non-collinear ground states of the chains. Finally, the study of the relaxation behavior of isolated and coupled quantum spins in a thermal environment was described by a non-Hermitian Hamiltonian generator for the dynamics of pure quantum states.

Zusammenfassung

Diese Dissertation ist dem theoretischen und praktischen Verständnis von verschiedenen Wechselwirkungseffekten auf statische und dynamische Eigenschaften von klassischen und quantenmechanischen Spinsystemen gewidmet. Als interessante Systeme wurden dipolar gekoppelte Nanoteilchen in einem Temperaturbad, Spinketten mit kurz- und langreichweitiger Austausch- und Dipol-Dipol-Wechselwirkung sowie austauschgekoppelte, anisotrope Quantenspins in einer Energierelaxation auslösenden Umgebung studiert.

Für den Fall der gekoppelten Nanoteilchen wurde dabei ein Langevin-Algorithmus zur Implementierung von stochastischen Landau-Lifshitz-Gilbert-Gleichungen (LLG) bei endlicher Temperatur verwendet und durch analytische Betrachtungen für den Phasenraum und die Energielandschaft komplementiert. Die Untersuchung der Spinketten wurde ebenfalls mit einer stochastischen LLG sowie mit Monte-Carlo-Simulationen und analytischen Betrachtungen für die Vorhersage kollinearer und nichtkollinearer Grundzustände unterfüttert. Desweiteren wurde das Relaxationsverhalten isolierter und austauschgekoppelter Quantenspins in einer thermischen Umgebung mit einem neuartigen nichthermiteschen Erzeuger für die Zeitentwicklung reiner Zustände modelliert.

Chapter 1

Introduction

In today's age of computerized societies and economies there is a great need for improvement in the capacity and stability of digital data storage and adaptability of information processing devices, famously formulated in the form of Moore's law. Its content predicts an exponential growth of the density of transistors on integrated circuits [65].

Not very long ago, most available information has been represented and stored on paper for books or on vinyl records for audio related content. The introduction of digital computers and the invention of digital information based storage like magnetic hard drives, led to storage platforms using magnetic grains as fundamental units of classical bits, being manipulated via magnetic fields. Great progress has been made by employing magnetoresistive devices, such as the giant magnetoresistance effect [67], to create sensitive magnetic field sensors for a better read-out of magnetic bits. Challenges of the more recent past include increase of the density of magnetic grains in modern magnetic data storage devices.

As the density of magnetic grains on a hard drive becomes higher, one inevitably faces the problem of interactions between the individual particles of the array. This fact calls into question whether the magnetic particles can still be used as bits of information to be stored for a very long time ($\approx$ 10 years). These interactions manifest in the form of multipolar potential terms of which usually dipolar terms form a very good leading order approximation. These interactions must be considered as additional perturbations for the stability of magnetic grains other than thermodynamically unavoidable thermal fluctuations.

Another striking challenge in this rapidly expanding research field is the stability as well as the controlled creation or annihilation of particular bit states in increasingly narrow spatial arrangements. Fur this purpose, non-collinear magnetic ground state configurations have been proposed such as magnetic vortices, magnetic spirals, or magnetic skyrmions [45, 46, 47]. The latter two magnetic states attract additional interest because one can associate a nontrivial topological winding to the magnetization field of each system when the continuum limit of an infinite crystal lattice is considered.

A further challenge lies in the accurate theoretical description of experimentally investigated small magnetic systems that form the basis for understanding of the above mentioned devices of information technology. These systems are comprised of elementary quantum spins and while classical spin precession and relaxation (more correctly monodomain macrospins) can be conveniently described by the classical Landau-Lifshitz-Gilbert-Equation quantum spins generically follow the stochastic predictions of the time-dependent Schrödinger Equation for probability amplitudes. Luckily, in many applications the quantum coherent nature of the spins is removed due to quantum entanglement with an environment and is replaced by a classical probabilistic evolution law, described by a master equation [110].

In this thesis, the primary focus lies on how boundary conditions, internal interactions and coupling to environmental degrees of freedom affect one and two dimensional spin systems both structurally and dynamically in different settings. I used both classical and quantum mechanical approximation methods to explain my results and whenever necessary, I added analytical modelling and calculations to the numerical results. As an additional pillar, I was engaged in methodological work for developing and testing a dissipative wave equation and this will be discussed and highlighted in the second half of my thesis.

In order to give a comprehensive overview over the topics covered and methods that have been utilized, I will start with a theory chapter. This will deal with theories important for this thesis and introduce the numerical techniques, used in each chapter.

In chapter 3, the impact of long-range dipolar interactions on the dynamical behavior of disordered ferromagnetic nanoparticles, motivated by experimental research on small arrays of cobalt-platinum ferromagnetic nanodots [15], have been investigated. I used a system of coupled stochas-

tic Landau-Lifshitz-Gilbert Equations (SLLG) to model the impact of an effective magnetic field on each nanoparticle, assuming the validity of a macrospin approximation. The SLLG calculations revealed a crucial influence of dipolar interactions on the switching behavior of individual nanoparticles, leading to collective switching behavior, as well as a sensitive interplay of different parameters of the system, partially unobtainable via experiment. To complement the dynamical analysis, I performed additional calculations on the energy landscape and phase space of the system. Furthermore, an action-based model was added to bring together structural and dynamical findings of the system to a satisfying conclusion. The results of this work have been published in [1]. In addition, the correlation behavior of coupled nanoparticles have been calculated and quantified as a function of distance and based on elementary arguments a classical dynamical phase transition was proposed.

Chapter 4 deals with the proposition and realization of a physical model for energy storage and release, based on a chain of magnetic particles with chiral and topological excitations. Results were published in [53] and produced in close collaboration with E. Vedmedenko. We explored the critical role of external influences on terminal objects of the chain toward the entire chain, leading the path to a systematic, parameter-controlled manipulation of the chain and a conversion of metastable states in an unconstrained system towards stable states in a constrained system. These findings were, among other things, motivated and preceded by results from energy and phase space analysis on magnetic configurations, dealt with in chapter 3. In this context, chapter 4 picks up and evolves questions that emerged in 3 while the focus is changed from a more dynamical perspective towards a structural. External control and dynamical aspects are still present and crucial.

After discussing dynamical and structural properties of open classical spin systems in the first part of the thesis, an implementation of a numerical method for a quantum counterpart of open spin systems was intended. Chapter (5) is dedicated to the general dynamical modelling of open quantum spin systems, based on a numerically improved and linearized version of a nonlinear Schrödinger Equation (SGE), introduced by Gisin [85]. This work brings together conceptual aspects of the foundations of quantum wave equations, their numerical efficiency in different representational forms and the possibility of using them for concrete quantum spin systems, as discussed in the previous chapters.

Chapter 2

Theory

This chapter is dedicated to introduce the theoretical concepts and models on which this thesis is based. First of all, a short phenomenological description of the different manifestations of macroscopic magnetism is provided. After that, the different underlying classical and quantum mechanical interaction laws are discussed which lead to the known phenomena of magnetic order on different length scales.

Secondly, a brief introduction to non-collinear states and topological protection in magnetic systems is given. This will help to understand the notions of topological order, appearing in the context of chapter 4 of this thesis. Finally, the basic ideas of closed and open quantum systems will be introduced in order to have some background for the results of chapter 5 of this thesis.

2.1 Magnetic order in atomic and nano-sized physical systems

Research on magnetism delivered ground breaking knowledge in different parts of physics in the last 200 years, ranging from atomic and molecular physics towards astrophysics and cosmology. At the fundamental level of elementary particles magnetic phenomena are described by Maxwell's equations and the Pauli exclusion principle.

The advent of experimental and theoretical methods in the course of the 20th century enabled to investigate magnetism at the nanoscale when quantum effects become important and govern the magnetic interactions between elementary spin degrees of freedom.

Magnetic order manifests in nature in different forms. Usually, one differentiates five classes of magnetic phases: *Ferromagnetism*, *Antiferromagnetism*, *Paramagnetism*, *Diamagnetism* and *Superparamagnetism*. Paramagnetism is defined by the property of solids, small particles, isolated atoms or ions to have a vanishing time-averaged expectation value of magnetization $\langle M \rangle_t = \sum_i \frac{\vec{\mu_i}}{V}$ (for volume V and magnetic moment $\vec{\mu}$). This effect is caused by thermal fluctuations that prevent a time averaged orientation from forming. The theoretical description is given by the Langevin formalism which assumes no residual interactions between adjacent magnetic moments that form a paramagnet [24].

A solid will be refered to as ferromagnetic, if the atomic magnetic moments align in small compartments in the same direction. These regions are known as magnetic domains and were introduced by Weiss for the first time [141]. A ferromagnet is characterized by a characteristic magnetization curve which tracks the magnitude of the magnetization as a function of applied external magnetic field. Due to its importance for understanding ferromagnetic and superparamagnetic particles, this magnetization curve is described in more detail below:

First of all, the ferromagnet with saturation magnetization M_S will be completely demagnetized during a time interval $t = \tau_{demag.}$ by undergoing repeated magnetization cycles with decreasing area in the plane, spanned by external magnetic field and magnetization. This can be managed by a time-dependent, oscillating magnetic field $B_{ext} = B_0 \sin(\omega t) f(t)$ with amplitude $B_0 \geq B_c$ and a decaying function $f = f(t) \to 0$ (for $t \approx \tau_{demag.}$) which steadily decreases both total magnitude $M_{max} = M_{max}(t)$ and residual/remanence value of the magnetization of the ferromagnet $M_R = M_R(t)$.

Then the curve starts at the origin $(\vec{M}, \vec{B}) = (0, 0)$. The increase of the external magnetic field value creates domain wall motion in the ferromagnet which leads to the decrease of the size of domains with anti-parallel alignment to the magnetic field $\vec{M}_{domain} \| \vec{B} = \mu_0 \vec{H}$, resulting in the minimization of the Zeeman energy

$$-g\mu_B \vec{H} \vec{S}_i. \tag{2.1}$$

Its magnitude is directly proportional to the external field. The scattering of domain walls on impurities impedes the growth of the energetically favorable domains and behind the impurities a

bubble of magnetic moments arises, preserving the orientation of several magnetic moments in the vicinity until the direction is suddenly flipped in a collective manner. This phenomenon is coined "Barkhausen jump" and once all bubbles have flipped parallel to the magnetic field direction the magnetization converges to the saturation magnetization $\vec{M}_S$ for field values values $H \geq H_S$. As the magnitude of the external field is reduced, the magnetization decreases and reaches a finite value in zero field, called remanence M_R. This can be traced back to an irreversible shifting of domain walls under the influence of the impurities. When a critical negative field value is reached the magnetization finally passes the zero level again and it will reach the negative magnetization saturation for even larger negative field value. Upon remagnetizing the ferromagnet, the system will eventually reach $\vec{M}_S$ for H_S and a new loop is initiated. The cycle is called hysteresis, reflecting that the evolution of the magnetization magnitude depends on the history of the system while each point in the loop corresponds to a time averaged value. The area that is enclosed by the magnetization curve is a measure for the produced heat

$$Q = \int_{-H_S}^{H_S} \vec{M} dH \tag{2.2}$$

which converts into an increase in entropy S by an amount of $\Delta S = \frac{\Delta Q}{T}$.

2.1.1 Magnetic interactions

According to classical electrodynamics, a magnetic moment $\vec{\mu}_i$ generates a magnetic field of flux density $\vec{B}_{\mu_j(\vec{r})}$ at location $\vec{r}$, where another magnetic moment $\vec{\mu}_i$ aligns parallel to that generated field. The interaction energy of N moments is calculated by

$$E_{dd} = \frac{1}{2} \cdot \frac{\mu_0}{4\pi} \sum_{ij, i \neq j}^{N} \Big(\frac{\vec{\mu_i}\vec{\mu_j}}{r_{ij}^3} - \frac{3 \cdot (\vec{\mu_i} \cdot \vec{r_{ij}})(\vec{\mu_j} \cdot \vec{r_{ij}})}{r_{ij}^5} \Big) \tag{2.3}$$

$$E_{b,i} = -\frac{1}{2} \sum_{ij, i \neq j}^{N} \vec{\mu_i} \cdot \vec{B}_j(\vec{r_{ij}}) \tag{2.4}$$

with the effective dipolar fields of the moments $\vec{\mu_j}$ onto the moment $\vec{\mu_i}$. The factor 1/2 ensures that the interaction energy is not counted twice. As the dipolar interaction only decreases proportional to the inverse cube of the particle distance, it is considered long-range. A system with only two

magnetic dipoles already has an energy landscape with several saddle points and a global minimum parallel to the connecting line between the particles. This will be the starting point of analytical predictions in chapter 5.

Especially for strong anisotropic energies perpendicular to the film plane, there is a tendency toward antiferromagnetic coupling behavior which is important for chapter 4. Despite its frequent occurence, the dipolar energy doesn't explain the emergence of ferromagnetism between atomic magnetic moments, as for parallel alignment the dipolar energy E_{dd} would be just 0.1 meV for a typical lattice constant of a$\approx$ 0.3 nm. This would not be a robust energy scale against thermal fluctuations at room temperature. Nevertheless, transition metals such as iron, cobalt or nickel are observed in the ferromagnetic state at room temperature.

The key to the understanding of ferromagnetic coupling lies in the short-range exchange interaction between neighboring spins. It is of quantum mechanical origin, favors either ferromagnetic or antiparallel alignment and is quantified via a scalar product

$$E_{exchange} = - \sum_{\langle i,j \rangle i \neq j, |i-j|=1} J_{ij} \vec{S}_i \cdot \vec{S}_j \tag{2.5}$$

$$J_{ij} \propto \int_{V_1} \int_{V_2} \Psi^*(\vec{r_1}, \vec{r_2}) H \Psi(\vec{r_1}, \vec{r_2}) \mathrm{d}r_1 \mathrm{d}r_2. \tag{2.6}$$

J_{ij} is the exchange integral and Ψ is a completely antisymmetric wavefunction formed by a spin and position wavefunction part, respectively [119]. This integral typically has significant non-zero value for nearest neighbors, but occasionally extends to more neighbors. Dependent on the model, the spins $\vec{S}_i$ and $\vec{S}_j$ can be modelled either as classical vectors or with the help of raising and lowering operators $\hat{S}^{\pm}_{i,j} = \hat{S}_{i,j,x} \pm i\hat{S}_{i,j,y}$ as quantum mechanical observables.

A special form of the exchange interaction is described by the Rudermann-Kittel-Kasuya-Yoshida interaction (short: RKKY interaction) [150] which is mediated indirectly through polarized s-electrons, causing the interaction to be long-ranged, similar to the dipole-dipole interaction. Furthermore, the amplitude of the interaction oscillates periodically between ferromagnetic and antiferromagnetic coupling while its value decreases with an inverse cube law. This behavior is

straightforwardly explained by a Fourier representation in dual k-space where the interaction energy is constant, as the quasi-free conduction electrons $E(\vec{k}) \approx \frac{\hbar^2 k^2}{2m}$ lie in the vicinity of the Fermi edge. A Fourier transformation into real space results in the sinusoidal coupling pattern:

$$J_{ij} = \sum_{\vec{k}} J(\vec{k}) \exp(-i\vec{k}(\vec{R}_i - \vec{R}_j) \tag{2.7}$$

$$J_{ij} = \frac{-J^2 k_F^6 (\sin(2k_F R_{ij}) - 2k_F R_{ij} \cos(2k_F R_{ij}))}{E_F (2k_F R_{ij})^4} \tag{2.8}$$

The exchange interaction J_{ij} leads to a favorable angle of nearest neighbor spins of $\theta = 0$ or θ=π, but there is no prefered direction in space for this alignment in the absence of an external field. This isotropy should therefore lead to a vanishing magnetization average $\langle M \rangle_t = 0$ based on symmetry considerations. A spontaneous magnetization along a crystallographic axis therefore has to be attributed to a symmetry breaking that originates in the relativistic spin-orbit coupling which is known as magnetocrystalline anisotropy.

In a crystalline environment, a magnetic moment experiences a crystal field from surrounding point charges which usually leads to an easy axis along which electrostatic energy is minimized. This creates a minimal overlap for the atomic orbitals of the considered ion with the surrounding charges which are also known as ligands. The possible prefered directions depend on the symmetry of the crystal field and will be described as the easy axis of the system. As the rotating charge can be considered as an orbital angular momentum $\vec{L}$ of the electron with spin angular momentum $\vec{S}$, the anisotropy is finally reduced to the spin-orbit-coupling.

If only one easy axis exists in the system, one speaks of uniaxial anisotropy. For an easy axis parallel to the z-axis, one has

$$E_{\mathrm{K}_\perp} = -\sum_i K \cdot \mu_i \cos^2\theta \ \ (\text{for } \theta = 0 \ldots \pi) \ \text{ or } \ E_{\mathrm{K}_\perp} = -\sum_i K \mu_i \sin^2\theta \ \ (\text{for } \theta = -\pi/2 \ldots \pi/2) \tag{2.9}$$

$$E_{K_\perp} = -\sum_i K \cdot S_{z,i}^2 \quad (\text{cartesian coordinates}) \tag{2.10}$$

For an easy axis in the plane, we have least energy for a spin configuration in the x-y plane.

2.1.2 Superparamagnetism

Superparamagnetism describes the magnetic behavior of a very small particle of a ferromagnet which doesn't form more than one magnetic domain due to its small volume and the cost for domain wall creation. The atomic magnetic moments of the domain compartment are aligned collinearly, but the total magnetization behaves paramagnetic (as a function of time) below a critical size of the particle. This special form of paramagnetic behavior is also known as *superparamagnetic* behavior.

The switching process of such particles is described through coherent rotation or by domain wall propagation. For later considerations in chapter 4 domain wall propagation is ruled out as a dynamical reversal process. These particles do not undergo hysteresis while completing a magnetization curve loop, as there is no irreversible behavior expected for the polarization process of the magnetization. The curve describes an s-shape which can be derived from elementary considerations in statistical mechanics.

The statistical mechanical expectation value of a superparamagnetic particle can be determined via the well known canonic ensemble. We start with a Hamiltonian of the form

$$\mathcal{H} = -\mu_0 \mu_S \vec{S}\vec{B} \tag{2.11}$$

and assume an Ising-model with two stable states of energy E_1 and E_2 in $\pm$-z direction, leading to an expectation value with the canonical partition sum $\mathcal{Z} = \sum_{i=1}^{2} exp(\beta E_i)$ as

$$\langle M_z \rangle = M_0 \frac{\exp(-\beta\mathcal{H})}{\mathcal{Z}} = M_0 \frac{\exp(-\beta(E_2 - E_1)}{\mathcal{Z}} \tag{2.12}$$

$$= M_0 \frac{\exp(+\beta\mu_o\mu_S\vec{S}\vec{B}) - \exp(-\beta\mu_o\mu_S\vec{S}\vec{B})}{\exp(+\beta(\mu_o\mu_S\vec{S}\vec{B})) + \exp(-\beta\mu_o\mu_S\vec{S}\vec{B})} \tag{2.13}$$

$$= M_0 \frac{\sin(\beta\mu_0\mu_s S_z B_z)}{\cos(\mu_0\mu_s S_z B_z)} = M_0 \tan(\beta\mu_0\mu_s S_z B_z). \tag{2.14}$$

The magnetization curve, belonging to $\vec{M}$(B) is s-shaped and has a reversible character as mentioned before.

2.1.3 Néel-Brown-Law und Stoner-Wohlfarth-Approximation

The different contributions of the magnetostatic stray field energy, the exchange energy and the magnetocrystalline anisotropy decide whether magnetic particles form one or multiple single domain states. For sufficiently small volumes the second case will be realized because exchange coupling would prevail in this scenario. A particle with saturation moment $|\vec{\mu_s}| \geq \mu_B$, uniaxial anisotropy constant K, external field $\mu_0\vec{H}$ and vanishing residual interactions will be described by a Hamiltonian of the following kind:

$$\mathcal{H} = -J\sum_{\langle i,j\rangle}\vec{S}_i\vec{S}_j - K\sum_i S_{z,i}^2 - E_{\text{dd}} - \mu_0\vec{\mu_s}g\vec{S}_i\vec{H}. \tag{2.15}$$

The switching of the saturation moment, also coined macrospin, has two basic distinguishable modes: The first possibility is provided by a coherent rotation of all N spins of the particle and the second possibility is a propagation of a domain wall across the particle. The nucleation of a domain wall with area S_{dw} requires an energy amount of

$$E_{\text{dw}} = 2S_{\text{dw}}\sqrt{A\cdot K}. \tag{2.16}$$

In the past, the possibility of the nucleation of one or more domain walls for high anisotropy magnetic particles was shown in [146].

If the Hamiltonian function of the macrospins (2.15) satisfies the conditions for coherent rotations, one speaks of a Stoner Wohlfarth-particle [145]. The interaction with an external field and the alignment in an anisotropy field is described through

$$E = KV\sin^2\theta - \mu_0\mu_s BS_i\cos\phi \tag{2.17}$$

with the angles θ=$\angle(\vec{B}_{\text{text}}, \vec{M})$ and $\phi = (\vec{K}, \vec{M})$. By demanding minimization of E with respect to a variation of the angle θ, one arrives at the extremal value problem

$$\frac{\partial E}{\partial \theta} = \sin\theta(2KV\cos\theta + \mu H) = 0 \tag{2.18}$$

$$\frac{\partial^2 E}{\partial \theta^2} < 0 \quad \text{(Maximum)} \tag{2.19}$$

$$\frac{\partial^2 E}{\partial \theta^2} > 0 \quad \text{(Minimum)} \tag{2.20}$$

with extreme positions

$$E_{min,1} = -\mu H \tag{2.21}$$

$$E_{min,2} = +\mu H \tag{2.22}$$

$$E_{max} = KV + \frac{(\mu H)^2}{4KV} = KV\Big[1 + \Big(\frac{HM_s}{2K}\Big)\Big]. \tag{2.23}$$

The minima are the roots of the sine θ=0° and θ=180° and the maxima are at the position, where $\cos\theta = \frac{-\mu H}{2KV}$. A transition between different minima can be realized by a jump over the barrier $\Delta E_{1,2} = E_{max} - E_{min,1,2}$. Neél and Brown deduced a stochastic model for the switching behavior of monodomain particles that appears like an Arrhenius-law

$$\nu = \nu_0 \exp\Big(-\frac{\Delta E}{k_B T}\Big), \tag{2.24}$$

as it is known for transition rates in certain chemical reactions. The frequency ν_0 is in the simplest approximation an attempt frequency which would be exactly the switching frequency for a vanishing energy barrier $\frac{\Delta E}{k_B T} \to 0$. This frequency depends on the Lamor precessional frequency, known from quantum mechanics of spin angular momentum in external magnetic fields. The exponential factor is directly related to a Boltzmann factor from statistical mechanics.

A coercive field of magnitude $H_K = \frac{2K}{M_s}$ yields switching frequencies

$$\nu_{12} = \nu_{12}^0 e^{-(E_{max}-E_{min,1})/k_B T} = \nu_{12}^0 e^{-KV(1+H/H_K)/k_B T} \tag{2.25}$$

$$\nu_{21} = \nu_{21}^0 e^{-(E_{max}-E_{min,1})/k_B T} = \nu_{21}^0 e^{-KV(1-H/H_K)/k_B T}. \tag{2.26}$$

They are symmetric in the limit $H \to 0$, implying $\nu_{12} \equiv \nu_{21}$ and $H \geq H_K$ maximal.

Which switching mechanism dominates depends on the form and extension of the particle [16]. The switching frequency will be determined through the anisotropy barrier ΔE= $E_{\text{max}} - E_{\text{min}}$, expressing the difference between the most and least favorable energetic states $\theta = 0$ and $\theta = \pi$: ΔE= $E_{\text{max}} - E_{\text{min}}$. This energy can still be increased or decreased by Zeeman energy and dipolar energy, respectively.

$$\hat{H} = -J \sum_{\langle i,j \rangle} \vec{S}_i \vec{S}_j - K \sum_i \vec{S}_{i,z}^2 - E_{dd} - \mu_0 \vec{\mu}_s g \vec{S}_i \vec{H}. \tag{2.27}$$

The time period that passes in between two switching events is the averaged life time $\tau = 1/\nu$ of a favorable magnetic state. It depends exponentially on the temperature and the energy barrier. The time span τ of a particle in a particular state determines the time dependent magnetization $\langle \vec{M} \rangle (\vec{B})$=$M_0 \cdot \exp(-t/\tau)$ which is determined in an experiment of measurement duration $t = t_{exp}$. One can think of this in formal analogy to a radioactive decay at time t_0=0 in a sample with N nuclei and a decay rate $\lambda \neq 0$. After the time $t_1 = t$, one still has

$$N(t) = N_0 \exp(-\lambda \cdot t) \tag{2.28}$$

radioactive nuclei. Switching of $\vec{M}$ and a decay event are both be considered as an irreversible process.

2.2 Spin spirals and winding numbers

2.2.1 Non-collinear magnetic states

The emergence of non-collinear spin states is a topic of low-dimensional magnetism and results from competing magnetic interactions. In monolayers the nearest neighbor distance, the symmetry and the hybridization with the substrate can play an important role for the determination of magnetic properties. This can lead to a variety of magnetic structures, from ferromagnetic and antiferromagnetic states, as discussed in the previous section, towards complex, non-collinear spin textures. The formation of a ferromagnetic or antiferromagnetic state can be the result of a domi-

nating nearest neighbor exchange interaction; complex magnetic structures, however, often provide a hint to a situation of competing magnetic interactions. Magnetic interactions in a monolayer on a substrate are conveniently described by fitting the results of an ab-initio electronic structure model, such as spin-density functional theory [121], to a two-dimensional Heisenberg model. When such information is provided, it becomes possible to search for the origin of a specific magnetic ground state and the relevant magnetic interactions that compete for influence.

Special emphasize is put on non-collinear states in one spatial dimension (a.k.a. spin spirals) and can be explained in different ways in this picture of the two dimensional Heisenberg model. The first possibility consists in having two different couplings $J_1 > 0$ and $J_2 < 0$ for nearest and next-nearest neighbor coupling between spins where a competition for parallel and anti-parallel alignment leads to helical or cycloidal spirals. The so called Dzyaloshinskii-Moriya (DM) interaction relates the spins via a vector product and can play an important role when the inversion symmetry of the system is broken at the surfaces. Its Hamiltonian reads

$$E_{DM} = \sum_{i,j} \vec{D}_{i,j} \cdot (\vec{S}_i \times \vec{S}_j) \tag{2.29}$$

It favors a 90°-spin spiral and the rotational sense is determined by the sign of D; high symmetry surfaces typically favor a formation of cycloidal spin spirals. Of course, competition between Heisenberg exchange and DM-interaction may lead to spin spirals with any angle between adjacent spins and also higher-order interactions can play a role for the magnetic ground state.

The first experimental realization of a spin spiral ground state at a surface was observed in the system of one monolayer of Mn on a W(110) surface [122].

2.2.2 Topological properties in continuous magnetic systems

The spin spiral, considered in the continuum limit of a magnetization field, when modulated only in one spherical angle θ or ϕ, has interesting topological properties, as its magnetization field $\vec{M}(\vec{r})$ can be mapped exactly to a circle which reflects the description by the first homotopy group $\pi_1(X)$. This is defined by a mapping

$$M : S^1 \to X \tag{2.30}$$

from the unit circle to the space of interest and in the case of the spin spiral the space X amounts to the set of orientations of spins of the chain. This means that there exists no continuous transformation between a spin state in which a spiral exists and one where either no spiral or several (two or more) spirals exist. This can also be formalized by the concept of the winding number obtained from the Stokes theorem:

$$n_1 = \frac{1}{2\pi} \int_0^{2\pi} 1 d\phi \tag{2.31}$$

The winding number is normalized to unity for a complete integral over the S^1-sphere and plays a role in chapter 4 for determining the nontrivial topological state of the continuum limit in the non-collinear ground states and excited states.

2.3 Dynamics in closed and open quantum systems

Familiarity with the axioms of quantum mechanics will be assumed in the following (see also [123]).

We describe the dynamics of a closed system in non-relativistic quantum mechanics by the time-dependent Schrödinger Equation

$$i\hbar \frac{\partial}{\partial t} |\psi\rangle = H|\psi\rangle. \tag{2.32}$$

with the Hamiltonian H and a pure state $|\psi\rangle$ (a projective ray, equipped with an equivalence relation $|\psi\rangle \cong |\phi\rangle = \alpha|\psi\rangle$ and $\alpha \in \mathcal{C}$).

It has an equivalent formulation by an equation for a density operator and is called von-Neumann-Equation:

$$i\hbar \frac{\partial}{\partial t} \rho = [H, \rho]. \tag{2.33}$$

In terms of quantum statistical mechanics such a density operator is a convex combination of pure

quantum states

$$\rho = \sum_i p_i |\psi_i\rangle\langle\psi_i| \tag{2.34}$$

and can be represented by a direct sum of irreducible representations of projective Hilbert space rays.

If one likes to determine the dynamics of an open quantum system, one has to consider a tensor product space of a relevant system of interest $\rho_{sys.}$ and a second system, conveniently called "environment", $\rho_{env.}$. $\rho_{tot.} = \rho_{env.} \otimes \rho_{sys.}$, which must then be traced out by an operation

$$\langle\psi_{env.}|\rho_{env.} \otimes \rho_{sys.}|\psi_{env.}\rangle, \tag{2.35}$$

called the partial trace. This partial trace ignores the information of the environment and effectively reduces the dimension of the total system to that of the system of relevance. As the partial trace maps from a higher dimensional representation of a density operator to a lower dimensional representation of a density operator it is ensured to be a linear map. Whether system and environment are energetically coupled and thus entangled, also depends on the physical situation of interest.

A famous dynamical equation for an open quantum system that makes a lot of idealizations [79] but is a good first approximation in many applicational scenarios is the Lindblad Equation which reads

$$\frac{\partial}{\partial t}\rho_{sys.} = -\frac{i}{\hbar}[\rho_{sys.}, H] + \sum_{i,j}^{N^2-1} H_{i,j}([a_i \rho a_j^+] - \frac{1}{2}[a_j^+ a_j, \rho_{sys.}]). \tag{2.36}$$

The first term of the r.h.s. is an ordinary and potentially renormalized Hamiltonian contribution of the "original small system". The second term is called a dissipator $\mathcal{D}(a_i, a_j^+)$ and has an anti-Hermitian structure, if one conveniently chooses the Hamiltonian part as the Hermitian part. The coefficient matrix $H_{i,j}$ is a completely-positive map. However, it doesn't conserve the trace of the density operator ρ which is very important for the probability interpretation and this is why there is another summand in the dissipator where $a_j^+ a_j := a_j^+ \mathbf{1} a_j$ is the renormalization of the unit element for every time step [143, 144]. This term will be important to look at later in chapter 6 of this thesis.

The Eq. (2.36) describes a memory-less semi-group evolution behavior of the density operator

and thus models exponential-type relaxation.

In chapter 6, an equation for pure states is written down which corresponds to this equation in the decoherence regime of a classical density function $\rho_{sys.} := \rho_{sys.}^{class.}$. Introduction of appropriate weighting factors $w_i = w_i(a_i)$ and $w_i^* = w_i^*(a_i^+)$ for the i-th state in the coefficient matrix $H_{i,j}$ even grants the possibility to phenomenologically model a thermal (quantum) distribution $\rho \propto \frac{1}{\exp(E_i/k_B T(\pm 1))}$ for the reduced density matrix at hand.

2.4 Simulation methods

2.4.1 Spin dynamics

In order to describe the dynamics of classical magnetic systems, one uses mainly three different types of equations of motion: The Landau-Lifshitz-Equation [27], the Gilbert-Equation [87] and the Landau-Lifshitz-Gilbert-Equation [88] which have been derived in this temporal order. The derivation of these differential equations will be presented in the following subsections:

Landau-Lifshitz-Equation (LL)

The Landau-Lifshitz-Equation, introduced by Landau and Lifshitz in 1935, is an ordinary, nonlinear differential equation of first order and consists of two summands. The first summand is called the precession term and has a quantum mechanical origin when derived in the Heisenberg picture for an interaction of a spin and an external field. The second term is called the damping term and is of phenomenological nature:

The precession term

The origin of the derivation is provided by the Heisenberg equation of motion:

$$i\hbar \frac{\partial \langle \hat{S}_i(t) \rangle}{\partial t} = \langle [\hat{S}_i(t), \hat{\mathcal{H}}] \rangle \tag{2.37}$$

with the time dependent spin operator $\hat{S}_i(t)$ and the Hamiltonian $\hat{\mathcal{H}} = -\frac{\partial \hat{\mathcal{H}}}{\partial \hat{S}_i}$.
By using the ordinary angular momentum commutation relations for spins

$$[\hat{S}_i^x, \hat{S}_j^y] = i\hbar\epsilon_{ijk}\hat{S}_k^z \tag{2.38}$$

and an expansion of the commutator from 2.37 in powers of Planck's constant $\hbar$

$$[\hat{S}_i(t), \hat{\mathcal{H}}] = i\hbar\hat{S}_i \times \frac{\partial\hat{\mathcal{H}}}{\partial\hat{S}_i} + O(\hbar^2) \tag{2.39}$$

the Heisenberg equation of motion can be written in the form of a cross product:

$$i\hbar\frac{\partial\langle\hat{S}_i(t)\rangle}{\partial t} = i\hbar\langle\hat{S}_i \times \frac{\partial\hat{\mathcal{H}}}{\partial\hat{S}_i}\rangle + O(\hbar^2). \tag{2.40}$$

Note that the classical limit reads $\hbar \to 0$ and that not all nonlinear terms in 2.40 vanish. Based on the Ehrenfest theorem [135] concerning the identification of quantum expectation values with classical vectors under certain assumptions, it follows

$$\frac{\partial\langle\vec{s}_i\rangle}{\partial t} = \vec{s}_i \times \frac{\partial\hat{\mathcal{H}}}{\partial\vec{s}_i}. \tag{2.41}$$

The proportionality of the magnetic moment $\vec{\mu}$ and the spin $\vec{s}$ via $\vec{\mu} = -\gamma\vec{s}$ immediately yields the expression

$$\vec{s}_i = -\frac{\mu_s}{\gamma}\vec{S}_i \tag{2.42}$$

with a normalized spin vector $\vec{S}_i = \frac{\vec{\mu}_i}{\mu_s}$.

Inserting this into (2.40) leads to the precession term of the Landau-Lifshitz-Equation

$$\frac{\partial\vec{S}_i}{\partial t} = -\frac{\gamma}{\mu_s}\vec{S}_i \times \frac{\partial\hat{\mathcal{H}}}{\partial\vec{s}_i}. \tag{2.43}$$

Physically, this term describes a precessional motion of the spin vector around an effective, magnetic field $\vec{H}_{\text{i,eff}}$.

The damping term

An undamped dynamics, as presented in (2.4.1) is not physically realistic such that one requires another term which can emulate dissipative effects on the spin vectors. This term is oriented perpendicular to the precession term and the effective magnetic field and causes a steady motion toward

the effective magnetic field while the exact speed of this process is parameterized by the dimensionless damping parameter λ.

Conveniently, this idea can be converted into a double cross product structure

$$-\frac{\lambda}{\mu_s}\vec{S}_i \times (\vec{S}_i \times \vec{H}_{\text{i,eff}}), \tag{2.44}$$

which was introduced without further background information by Landau and Lifshitz.

First analytic calculations for a system of uniaxial anisotropy in the 1950's produced a critical damping parameter value α_{krit} of $\mathcal{O}(10^{-9}\,\text{s})$ for fastest possible dynamical magnetization reversal through superposition of the precessional and damped motion under the influence of an external magnetic field [152].

2.4.2 Gilbert-Equation

Experimental results as well as foundational considerations imply an unphysical magnetization reversal process for large damping parameter values $\lambda >> 1$, as the reversal speed would become infinite and therefore exceed the speed of light and violate relativity theory [124]. Thomas L. Gilbert accounted for this issue by introducing a Rayleigh dissipation function into the damping term. By doing this, damped magnetization dynamics becomes structurally equivalent to the Rayleigh dissipation of a rigid body in classical mechanics, obtained from an extended Euler-Lagrange equation for a mechanically rotating body. The Gilbert equation, named in his honor, then reads

$$\frac{\partial \vec{S}_i}{\partial t} = -\frac{\gamma}{\mu_s}\vec{S}_i \times \vec{H}_{\text{i,eff}} + \alpha\Big(\vec{S}_i \times \frac{\partial \vec{S}_i}{\partial t}\Big), \tag{2.45}$$

and describes physically realistic results for the limit $\alpha \to \infty$. The microscopic origin of this term remains unexplained, though. This equation is difficult to handle for numerical integration and an improved version will be described in the following.

Landau-Lifshitz-Gilbert-Equation (LLG)

The Landau-Lifshitz-Equation, as mentioned above, only contains a time derivative expression for the spin vector on the left hand side of the equation and this more desirable form can be achieved for the Gilbert equation as well and naturally leads to the Landau-Lifshitz-Gilbert-Equation.

In order to achieve this, one multiplies "$\vec{S}_i\times$" from the right side and uses the Leibniz rule $\vec{a}\times(\vec{b}\times\vec{c})=\vec{b}(\vec{a}\cdot\vec{c})-\vec{c}(\vec{a}\cdot\vec{c})$ to get the expression

$$\vec{S}_i\times\frac{\partial\vec{S}_i}{\partial t}=-\frac{\gamma}{\mu_s}\vec{S}_i\times(\vec{S}_i\times\vec{H}_{\text{i,eff}})+\alpha\vec{S}_i\Big(\vec{S}_i\cdot\frac{\partial\vec{S}_i}{\partial t}\Big)-\alpha\frac{\partial\vec{S}_i}{\partial t}. \tag{2.46}$$

Due to spin normalization $\vec{S}_i^2=1$ and the product rule's use, one notices a vanishing of the second term of the right hand side

$$\vec{S}_i\times\frac{\partial\vec{S}_i}{\partial t}=-\frac{\gamma}{\mu_s}\vec{S}_i\times(\vec{S}_i\times\vec{H}_{\text{i,eff}})-\alpha\frac{\partial\vec{S}_i}{\partial t}. \tag{2.47}$$

This can be inserted directly into the damping term of the Gilbert Equation, thereby delivering a nonlinear differential equation of first order

$$\frac{\partial\vec{S}_i}{\partial t}=-\frac{\gamma}{(1+\alpha^2)\mu_s}\Big[\vec{S}_i\times\vec{H}_{\text{i,eff}}+\alpha\vec{S}_i\times(\vec{S}_i\times\vec{H}_{\text{i,eff}})\Big] \tag{2.48}$$

which is known as the Landau-Lifshitz-Gilbert-Equation [87]. A dynamical transition in an external magnetic field is represented in figure 2.1.

The energy minimization is equivalent to a vanishing torque of magnetization vector exerted by the effective magnetic field. This becomes apparent by expressing the cross product and scalar product via the intermediate angle θ_i. Equation 2.48 is instructively written as

$$\frac{\partial\vec{S}_i}{\partial t}=-\frac{\gamma}{(1+\alpha^2)\mu_s}\Big[\underbrace{\vec{S}_i\cdot\vec{H}_{\text{i,eff}}\sin\theta_i}_{\to 0\text{ for }\theta_i\to 0^0/180^0}+\underbrace{\vec{S}_i\cdot(\vec{S}_i\cdot\vec{H}_{\text{i,eff}}\cos\theta_i)}_{\to\vec{H}_{\text{i,eff}}\text{ for }\to 0^0/180^0}-\vec{H}_{\text{i,eff}}\Big]. \tag{2.49}$$

Finally, it should be emphasized that all three presented equations of motion could be derived from the Heisenberg equation of motion, but still assuming a classical vector space structure instead of that of a quantum mechanical Hilbert space for an observable algebra of spins [123]..

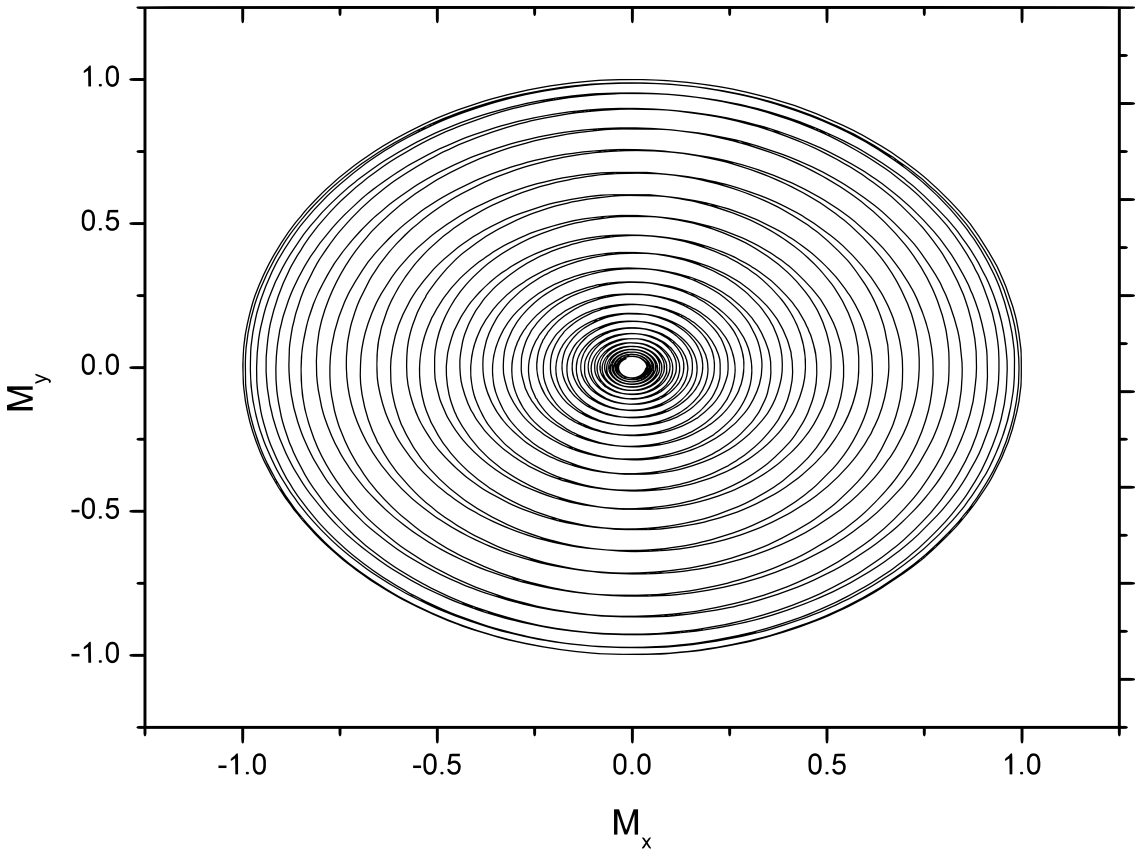

Figure 2.1: Damped precession of an isolated macrospin in an external field $B_z = -|\vec{B}|\vec{e}_z$ from $\mu_z = +0.98(\mu_s)\vec{e}_{\mu_z}$ towards $\mu_z = -1.00(\mu_s)\vec{e}_{\mu_z}$ in the μ_x-μ_y-plane.

Langevin-dynamics

The Néel-Brown law [62] implies a direct relation between temperature fluctuations in the environment and its effect on the magnetization reversal frequency of a magnetic domain. This effect is quantitatively described by an additional thermal field contributing to the effective field $-\frac{\partial \hat{\mathcal{H}}}{\partial \vec{S}_i}$ of the LLG-Equation which only describes Hamiltonian contributions in its original formulation. The additive thermal field has the signature of white Gaussian noise

$$\vec{H}_i = -\frac{\partial \hat{H}}{\partial \vec{S}_i} + \vec{\xi}_i(t) \tag{2.50}$$

satisfying the conditions

$$\langle \xi_i(t) \rangle = 0 \tag{2.51}$$

$$\langle \xi_i^{\nu}(t) \xi_j^{\theta}(t') \rangle = \underbrace{2\alpha\mu_s k_B T}_{q} \delta_{ij}\delta_{\nu\theta}\delta(t-t') \tag{2.52}$$

for the first and second statistical moment [40].

The strength of the noise q is obtained by inserting the solution to the Langevin Equation into the equipartition theorem [25]. In this representation, the influence of temperature is time-dependent and independent of the spin coordinates and thus stochastic rather than deterministic. This implies that the exact dynamics can not be derived from the initial conditions of the spin configuration. The advantage of this scheme is the breaking of time reversal symmetry and the ergodic occupation of the phase space in the long time limit $t \to \infty$. The indices i and j represent the lattice positions and ν, θ represent cartesian coordinates.

An equivalent formulation of Langevin-dynamics can be given in the framework of Hamiltonian dynamics. Here one starts with the classical Hamiltonian $H = \frac{p_i^2}{2m} + V(q)$ for generalized canonical coordinates q_i and momenta p_i and obtains equations of motion

$$dq = pdt \tag{2.53}$$

$$dp = -\nabla V(q)dt + -\gamma p dt + \kappa dW(t) \tag{2.54}$$

including a Wiener-random process W, satisfying the conditions from (2.51) [142].
Using the effective field expression, one can isolate a Langevin equation that decomposes into a part for the ordinary LLG-Equation and a stochastic noise part:

$$\frac{d\vec{S}_i}{dt} = f_i + g_i\xi_i \tag{2.55}$$

$$f_i = \frac{\gamma}{(1+\alpha^2)\mu_s}\Big[\vec{S}_i \times \vec{H}_{\text{i,eff}} + \alpha\vec{S}_i \times (\vec{S}_i \times \vec{H}_{\text{i,eff}})\Big] \tag{2.56}$$

$$g_i\xi_i = -\frac{\gamma}{(1+\alpha^2)\mu_s}\Big[\vec{S}_i \times \xi_i + \alpha\vec{S}_i \times (\vec{S}_i \times \xi_i)\Big]. \tag{2.57}$$

This is the stochastic LLG-Equation, being used in chapter 4 and 5 for numerical evaluation of the classical spin dynamics.

A very general description of the time evolution of physical systems is captured by a Markovian master equation [26]. This is a differential equation of first order in time and monitors the occupation probability w_μ of a physical state. It reads

$$\frac{d\,w_\mu}{dt} = \sum_\nu \Big[w_\mu(t) P(\nu \to \mu) - w_\mu(t) P(\mu \to \nu) \Big]. \tag{2.58}$$

The equation describes transition rates $P(\nu \to \mu)$ and $P(\mu \to \nu)$. The first term encodes the transition from an arbitrary state $\nu \neq \mu$ into the state μ and the second term converts the state μ into the state ν.

The transition rate $P(\nu \to \mu)$ in rescaled coordinates can also be interpreted as a function of the initial state ν and the jump $r = \mu - \nu$, and as such, one gets the master equation for a continuous Markovian process in integral form

$$\frac{d\,w(\mu,t)}{dt} = \int w(\mu - r; t) P(\mu - r, r) dr - w(\mu, t) \int P(\mu; -r) dr, \tag{2.59}$$

whereas from now on μ and ν are considered as continuous variables.
By expanding the first integral of (2.59) after the difference $(\mu - r)$ and assuming that the transition rate $P(\nu;\, r)$ is only non-zero for small jumps r, a special master equation, truncated to second order, emerges:

$$\frac{d\,w(\mu,t)}{dt} = \int w(y,t) P(y;r) dr - \int r \frac{\partial}{\partial \mu} w(y,t) P(y;r) dr + \tag{2.60}$$

$$\frac{1}{2} \int r \frac{\partial^2}{\partial \mu^2} w(y,t) P(y;r) dr - w(\mu,t) \int P(\mu; -r) dr. \tag{2.61}$$

The performed expansion is known as the Kramers-Moyal-expansion in the literature [114, 113].

If the expectation value and the variance of the jump is represented by $a_i(\mu) = \int r^i P(\mu; r)dr$, a one-dimensional Fokker-Planck-Equation (FKP) [112] is obtained

$$\frac{\partial w(\mu, t)}{\partial t} = -\frac{\partial}{\partial \mu}(a_1(y)w) + \frac{1}{2}\frac{\partial^2}{\partial \mu^2}(a_2(\mu)P) \tag{2.62}$$

with the drift coefficient a_1 and the diffusion term a_2.

If the coefficient a_1 is identified with the function f and a_2 with the function g from (2.55), an equivalence of the FKP and the mentioned Langevin Equation is achieved. In this way, it becomes visible, how the microscopic, spin dynamical calculations can realize a time-dependent expression that becomes equivalent to a canonical ensemble expectation value.

The general master equation expression also forms the basis for the Lindblad equation, mentioned in (2.36) and mentioned in chapter 6.

2.4.3 Numerical integration method

In this thesis, spin dynamics is either implemented by the stochastic LLG-Equation (2.48) or as a variant of the time-dependent Schrödinger Equation (2.32). Mathematically speaking, one treats an initial value problem $y'(x) = f(x)$ with supplied initial conditions $y(x_0) = y_0$. Unavoidable analytical complication, such as the nonlinear term in the stochastic LLG-Equation or the non-local nature of the dipole-dipole interaction term requires a numerical treatment and leads to an integro-differential equation in the most general case.

Euler-, Heun- and Runge-Kutta-methods

Systems of ordinary differential equations (ODE's) of k-th order read

$$y^k = f(t, y(t), y'(t), \ldots, y^(k-1)(t)) \tag{2.63}$$

$$y^1 = y_i, i = 0, \ldots, k-1 \tag{2.64}$$

and can always be reduced by successive variable transformation to a first order differential equation, treatable by initial value problem frameworks. The numerical integration of the r.h.s. of the

first order differential equation can be achieved by a single-step or multistep method.

Both methods deliver an approximative function $y(t)$ at a finite number of positions. The single-step method only uses information from the initial time t_i in order to approximate the function at the time t_{i+1} while the multistep method has multiple evaluation points t_j with $j \leq i$ to realize a proper approximation scheme. This work only treats single-step methods.

The easiest single-step method happens to be the Euler method. It linearly approximates the solution function y(t) in the interval h between y_n and y_{n+1} as

$$y_{n+1} = y_t + hf(t_n, y_n) \tag{2.65}$$

and produces a truncation error of the order $O(h^2)$, as can be easily verified by a Taylor expansion.

The second order Runge-Kutta-method provides a more precise approximation, as it uses two evaluation points at the beginning and at the center of the interval h, denoted k_1 and k_2.

The algorithm reads

$$k_1 = hf(t_n, y_n) \tag{2.66}$$

$$k_2 = hf(t_n + 0.5 * h, y_n + 0.5 * k_1) \tag{2.67}$$

$$y_{n+1} = y_n + k_2 + \mathcal{O}(h^3), \tag{2.68}$$

introducing a truncation error of order $\mathcal{O}(h^3)$. The same qualitative result can be achieved by the second order Heun-method.

The implemented single-step method, used in this thesis for implementation, is the classical fourth order Runge-Kutta method. This method uses four evaluation points with individualized numerical weights:

$$k_1 = hf(t_n, y_n) \tag{2.69}$$

$$k_2 = hf(t_n + \frac{h}{2}, y_n + \frac{k_1}{2}) \tag{2.70}$$

$$k_3 = hf(t_n + \frac{h}{2}, y_n + \frac{k_2}{2}) \tag{2.71}$$

$$k_4 = hf(t_n + h, y_n + k_3) \tag{2.72}$$

$$y_{n+1} = y_n + \frac{k_1}{6} + \frac{k_2}{3} + \frac{k_2}{3} + \frac{k_4}{6} + \mathcal{O}(h^5). \tag{2.73}$$

This algorithm, at $h' := 2h$, is numerically superior to an algorithm of a second order method at h. It is important to note that this method is also used to compensate for intrinsic numerical instabilities even in the case of a linear differential equation. This fact will be exploited in chapter 6 by a numerically efficient linear dissipative wave equation.

All represented algorithms can be found in [147].

Stochastic integration calculus

Generally, one has to consider two different definitions of stochastic integrals for the above mentioned non-deterministic equations of motion. The definition, used by the Ito-calculus, requires an evaluation of the stochastic process at the beginning of the interval of integration while the definition of the Stratonovich-calculus demands to take an average over initial and final values of the interval h. The implemented Runge-Kutta-method evaluates both the initial and final time of the interval and formally corresponds to the Stratonovich integral.

Chapter 3

Interaction assisted switching of ferromagnetic nanoparticles

3.1 Introduction

Until today, a considerable amount of research efforts in nano-scale magnetism and magnetic data storage is centered around questions of field- or temperature-induced reversal dynamics of ferromagnetic nanodots, arranged in small magnetic assemblies [2]-[12]. Studies on superparamagnetism and switching field distributions for ferromagnetic dots usually employ somewhat random densities of magnetic grains and thus the influence of dipolar energy on switching field distributions cannot be systematically extrapolated. In the quest for the highest possible density of storage units in modern age computer technology, a much more systematic study of the positive impact of interactions on coordinated switching behavior is both expected and demanded. Consequently, the 'rule of thumb', stating that inter-dot-coupling is almost negligible for arrays of average distance greater than the particles' diameters in a zero-field remanence state, must be put into question. For high density arrays, driven to instability by multiple means (temperature, fields, frustrated configurations, low perpendicular anisotropy, etc.), additional inter-particle energy contributions might further lower effective energy barriers and facilitate magnetization dynamical paths of decreased action upon traversing saddle points in the energy landscape.

In this chapter, I am going to describe theoretical studies on the interaction behavior of ferromagnetic nanoparticles in the light of long-range magnetostatic fields. The investigations are motivated

by an experimental setup of dipolarly coupled Co/Pt nanodots, pushed close to a state of instability due to the choice of temperature, magnetic field and easy axis anisotropy. The observed superparamagnetic behavior unraveled a correlated switching behavior of multiple magnetic dots due to the long-range nature of the interactions. This was confirmed in particular by simulations of stochastic, atomistic spin dynamics, modelling the nanodots as uniformly rotating single domain magnetic objects in macrospin approximation. These surprising findings significantly contribute to the understanding of the magnetostatically induced modified switching mechanisms of dilute, unstable magnetic ensembles and even more so for high density bit pattern configurations.

In the following sections of this chapter, I will elaborate on how multi-particle interactions affect the magnetization dynamics of nanoparticles and how far reaching those interactions are, measured against the diameter of a typical dot. I will briefly explain the experimental set-up of Co/Pt nanodots, placed on a Hall-cross and measured by the anomalous Hall-effect, and then quickly move on to theoretical considerations. Atomistic-Landau-Lifshitz-Gilbert simulations, including a stochastic field term, have been performed to analyze the magnetic ensemble for various sets of energetic parameters, time scales and distances. Analogous to the experimental situation, I simulated static magnetization curves and afterwards dynamical telegraph-noise plots to study the impact of interactions on different time scales and energetic influences. In all simulations, a rigid, single domain magnetic entity was assumed for all four involved dots, as domain wall propagation was believed to be negligible due to the exchange stiffness of Co/Pt composite particles.

As a second part of this chapter, I will model the dynamics of the nanodots in a more idealized, theoretical fashion to highlight the conceptual analogy of interacting nanodots and interactions between magnetic systems and dynamical fields via spin dynamics. The interaction of nanoparticles will be looked at as a generalized form of a dynamical phase transition [125] between two magnetic subsystems, influencing each other instead of being just influenced by a time-dependent periodic external field.

3.2 Collective switching of interacting nanodots

3.2.1 Experimental setup

The details of the fabrication process of nano-sized Co/Pt nanodots has been extensively described in [13, 14] to which I am referring in the following. It involves the extraction of the ferromagnetic dots from a planar Pt/Co/Pt multilayer ($Pt_{5\,nm}(Co_{0.8\,nm}Pt_{2\,nm})_3Pt_{1nm}$) by ion milling, using an SiO_2-based shadow mask. The platinum underlayer beneath the ferromagnetic dots is then exposed to electron beam litography with negative resist in order to further utilize it as a Hall-cross onto which the elements of study (approximately 35 nm in diameter) are attached to.

The intrinsic magnetic properties of the dots (of which low perpendicular magnetic anisotropy is of particular relevance for the studies of interest) were achieved by a combination of Co- and Pt-layer thickness optimization and the choice of films with canted magnetization. This guaranteed control of both magnitude and spatial orientation of the anisotropy axis is achieved due to cancellation effects of anisotropy and uncompensated magnetostatic fields at the interface. The fabricated dots admitted a low effective anisotropy energy $E_{k,1}^{eff}$ of the order of roughly 1 electron volt perpendicular to the film plane.

They have been positioned on a Hall cross of nanoscopic dimensions and all magnetization measurements have been performed based on the anomalous Hall effect which admits a proportionality to the perpendicular component of the magnetization vector. Much like in the historic setting, a current is applied and a transverse voltage is measured, but unlike for the classical Hall effect, the Co/Pt nanodots do not lead to a significant signal other than an anomalous contribution due to the magnetization. This interesting phenomenon is thoroughly explained in [17]-[20] and accounts for the averaged magnetization signal of all the four dots on the Hall cross.

In order to access the thermally activated magnetization dynamics of these Co/Pt nanodots, an in-plane field is applied to modify and reduce the barrier height separating oppositely magnetized perpendicular states [20]. The field strength is tuned appropriately such that the instability due to thermal agitation of the dot magnetization is observable. As the dots reveal different coercive fields the temporal behavior of an individual dot can be separately studied via an appropriately tuned in-plane field.

3.2.2 Results of the experiment and simulations

Figures 3.1 (a) and (b) shows the mean magnetization curves and time-dependent signals measured in the described set-up. Because of a slow ramping of external magnetic field, each step in figure 3.1(a) could be unambiguously assigned to an individual dot. From the dot-resolved measurement of the anomalous Hall voltage, one is able to identify the first reversal at about 5 mT, which corresponds to the switching of dot C, the second reversal at about 20 mT is produced by dot A, and the last switching at about 50 mT, corresponds to the reversal of dot D. More details of the procedure can be found in [13, 14].

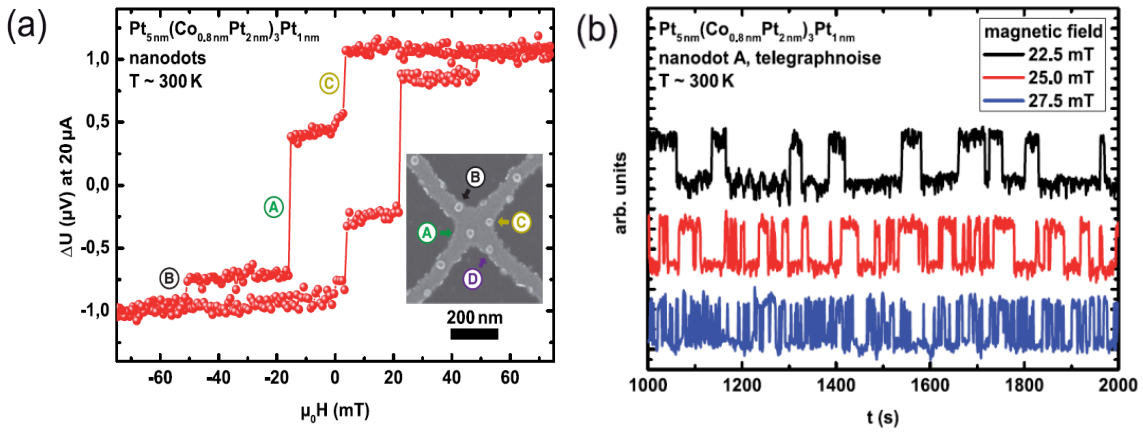

Figure 3.1: The response via the AHE of a system of four nanodots in fields with different orientation at T=300 K. (a) The switching fields of the individual dots are determined by application and slow ramping of a perpendicular field which is parallel to the anisotropy field of the dots. The scanning electron microscope image of the inset shows the four dots with a color code representation (A=green, B=black, C=yellow, D=violet). The dots C, A and B can be clearly assigned to magnetization reversal in the hysteresis loop at magnetic field values of 5 mT, 20 mT and 50 mT. A signal from dot D cannot be observed at room temperature. The dot size is 36 nm for A, C and D and 40 nm for dot B. (b) The telegraph noise for dot A is shown for different magnetic field strengths and one can clearly see that the in-plane field $B := B_x$ can effectively lower the barrier for dot magnetization reversal. An increase in switching frequency is evidently accompanied by this.

To probe the magnetization state and behavior of individual dots, the anomalous Hall-effect is used, which is directly proportional to the out-of-plane component of magnetization. As in a conventional Hall-type measurements, a current is applied and a cross voltage is measured. The normal Hall effect is negligibly small for the Co/Pt material system and only the magnetization-dependent anomalous contribution is seen in measurements [20,22], thus giving access to the magnetization state of individual nanoparticles. Figure 3.1(a) displays the magnetization behavior of the system

obtained in a single out-of-plane field sweep at room temperature for a system that consists of four dots on the Hall-cross (see inset of figure 3.1(a)). One can relate hysteresis loop features to each individual ferromagnetic dot by applying the current across adjacent leads and measuring the anomalous Hall voltage across the opposite leads as shown in [15] or via the signal height by bringing together the measured relative strengths with the calculated sensitivities for the conventional geometry [17, 18, 19].

In figure 3.1(b), the telegraph noise, obtained from dot A for three different field values, is presented. It is apparent that the field lowers the barrier, leading simultaneously to an increased frequency of switching with an increasing field strength.

For a lower temperature of T = 150 K, all four dot signals become visible in the hysteresis curves that are displayed in figure 3.2(a), particularly also for dot B. The most pronounced jumps can still be associated to the dots A and C, as seen previously for room temperature measurements in 3.1. The coercive fields of them are slightly increased in comparison to the room temperature measurement, as expected from the reduction of thermal agitation. The signal of dot D appears at a small field of approximately 5 mT. The absence of this signal for dot D in 3.1(a) can be explained by the fact, that it becomes superparamagnetic for the time scale of the measurement (at a given external field strength) at room temperature and its small signal is partially hidden behind the larger signal of dot C. Although the hysteresis loops at both temperatures are very similar, the analysis of the telegraph noise signal in magnetic in-plane fields unravels important differences (figure 3.2(b)). The sub-figures show the temporal signal for a domain of field strengths, for which switching behavior sets in for dot A. The fields are higher than for the room temperature measurements since the magnetization states are more robust against thermal activation, which can also be seen from the fact that the coercivities are increased. At the lowest in-plane field strength (35 mT), no switching event is observed. By increasing the field strength to 38 mT, the switching that corresponds to the one shown in figure 3.1(b) kicks in (same scales of the x-axis). However, a second switching is superimposed in the experiment (figure 3.2(b)) that is faster and has a smaller signal height. At 40 mT the frequency of the switching event with smaller amplitude is decreasing again. This observation gives rise to the hypothesis that a correlated switching event among dots at the verge of instability can be observed. However, the experiment doesn't allow for the verification of this hypothesis. Therefore, I further elaborated on this by simulation results in the next section.

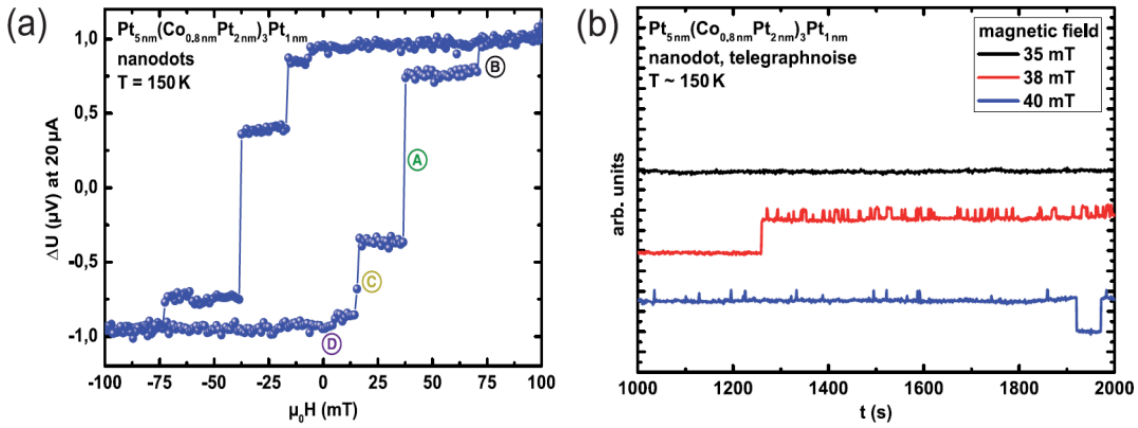

Figure 3.2: The AHE response of a system containing the four nanodots for different field orientation at a temperature T=150 K. (a) The magnetic hysteresis is now more pronounced due to the reduced thermal noise. For this set of parameters, one can unambiguously identify the jumps of all four nanodots, including dot B. The new switching fields are 5 mT, 20 mT, 38 mT and 70 mT. (b) The telegraph noise for dot A, as expected, exhibits much less jumps of magnetization. The in-plane magnetic field reveals an interesting fluctuating sub-signal on top of a larger seemingly more stable signal of magnetization at about 38 mT which becomes less pronounced at 40 mT and was even completely absent at 35 mT.

Switching at a critical field

In order to shed light on the question of correlated switching, I first simulated the expected equilibrium magnetization curves, using the parameters of the experiments in order to verify a computationally valid basis for the numerical dynamical analysis of the nanodot interaction. Fig. (3.3) reveals a very good match of the nanodot switching fields, described in figure (3.2) and is both plotted as a superimposed $\sum_{i=1}^{4} S_{z,i}$ and dot-resolved magnetization signal $S_{z,i}$.

After that, I analysed additional, dynamical experimental data at the critical field B=38mT, at which the interesting phenomenon, described in the last section, has been observed. In contrast to the behavior at room temperature, the signal heights at 150 K do not coincide with the signals obtained in the hysteresis loops. The hysteresis loop (figure 3.3(a)) shows jump heights of (1.13 ± 0.03) μV, (0.22 ± 0.03) μV, (0.46 ± 0.03) μV, and (0.08 ± 0.03) μV for dots A, B, C, and D, respectively. The signal heights in the telegraph noise are (0.83 ± 0.05) μV for the big jump and (0.25 ± 0.05) μV for the smaller jump. While the smaller jump height is somewhat close to the value found for dot B the large jump signal cannot be explained by any of the individual dot switching transitions obtained in the hysteresis loops. Even though the identification of the smaller signal seems to be natural at first glance, there are serious arguments against a dynamical switching of dot B. Based

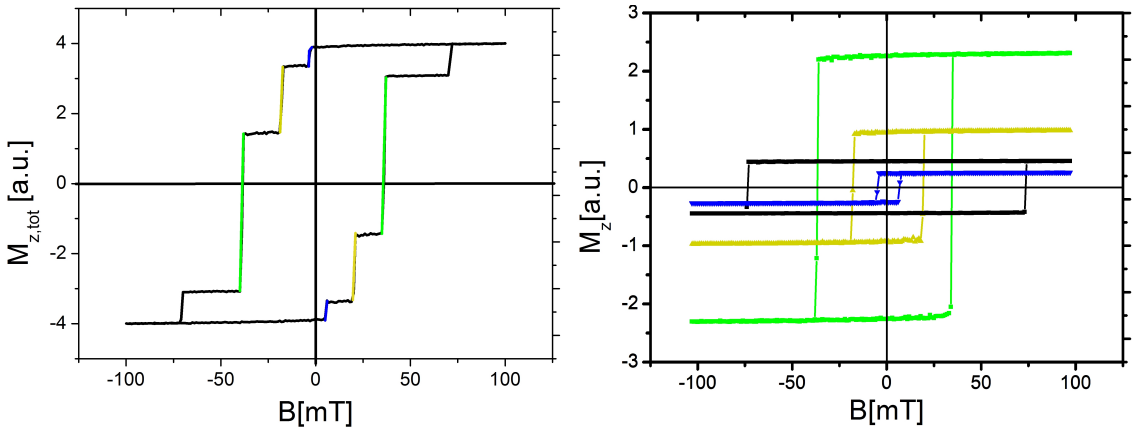

Figure 3.3: Simulated time-averaged magnetization curves of the four nanodots with (a) total magnetization and (b) dot-resolved magnetization of the z-component, parallel to the external field. The color code is adjusted to the experimental labelling. The numerical values of the anisotropy energies have been assumed as 1.3 eV, 1.6 eV, 0.9 eV, 0.8 eV for the dots A, B, C and D, respectively.

on the hysteresis curves, it is evident that dot B has the highest coercivity and anisotropy of all four dots. This means that by simple assuming single particle switching as a zeroth approximation the frequency should be the lowest among all particles. The switching between the central and upper level, however, appears with a high rate which obviously cannot be attributed to the switching of dot B in a single switching scenario.

A telegraph noise measurement for the four dots on an extended time interval is shown in figure 3.5(a) for an applied field of 38 mT. The temporal evolution reveals the already mentioned three voltage levels that are involved in the switching (inset). This was explained in terms of the evaluation of multiple spin dynamical simulations which favored such a particular ”3-spin switching scenario”. This is described in fig. (3.4).

Obviously, the system exhibits fast fluctuations, corresponding to an alteration between the two higher voltage levels of the AHE measurement. The total separation of the lower and upper voltage levels is (1.08 $\pm$ 0.05) μV. The value is apparently close to the signal of dot A in the hysteresis. When the value obtained in the hysteresis loop is corrected for the tilting of magnetization in the in-plane field, one could expect a signal height of 1.05 μV for the reversal of dot A. The good agreement between the predicted, effective signal height for dot A and telegraph signal of the measurement indicates that the net change between the lower and upper voltage level is caused exclusively by the reversal of dot A. Hence, we may conclude that the analysis of the experimentally measured voltage levels indicates that dot A is a key player in the observed thermal switching while

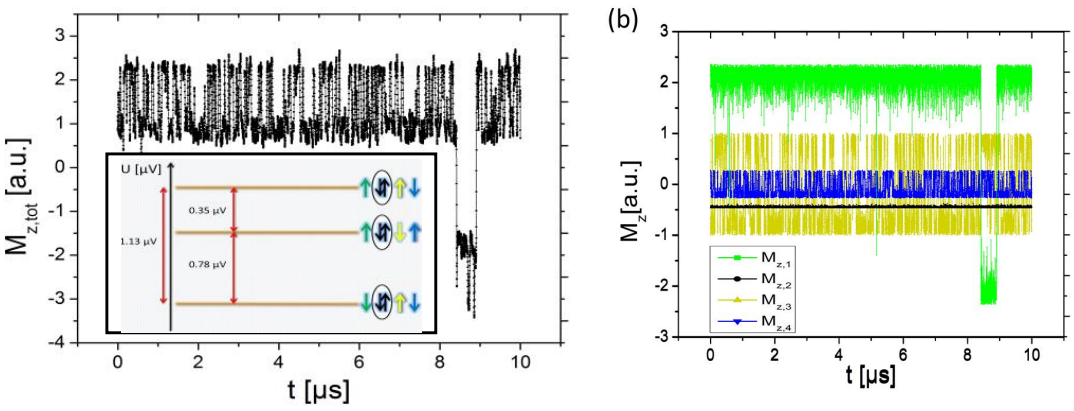

Figure 3.4: Favored 3-spin scenario for the switching behavior of the dots, according to spin dynamical simulations under appreciation of signal heights from the experiment and realistic energetic parameters for the nanodots. A sporadic switching of dot 'A' and a frequent switching of dots C and D have been rationalized and is shown via spin-averaged (a) and spin-resolved telegraph noise (b). The inset schematically shows the hypothetical signal heights of the anomalous Hall voltage, associated with such a switching, being within a tolerable error of approximately 6 percentages and 8 percentages of the experimental values with respect to the large signal and the small signal switching event.

other signals cannot be attributed to single dot switching.

As a next step, it is instructive to focus on the time scales of the switching events in figure (3.5). Utilizing the anisotropy that has been assumed, the effective barrier heights for single particle switching in the in-plane field can be estimated for dot A: $\Delta E_{\mathrm{A}}\,(38\ \mathrm{mT}) \approx 37\ k_{\mathrm{B}}T$. The result is that dot A should not switch on the time scale of the experiment (at 150 K) while dots C ($\Delta E_{\mathrm{C}}\,(38\ \mathrm{mT}) \approx k_{\mathrm{B}}T$) and D ($\Delta E_{\mathrm{D}}\,(38\ \mathrm{mT}) \ll k_{\mathrm{B}}T$) should switch with a frequency that is too fast to be resolved within the experiment (assuming an attempt frequency in the range of 1011 Hz). This means that the experimental result and the expected behavior (based on single particle potentials) are in disagreement, as values for dots C and D are too large and those for dot A are too small. Reasonable adjustment can thus not be made by a simple adjustment of the attempt frequencies. More importantly, the inset in figure 3(a) demonstrates that the transition from the bottom level always ends in the central level, which is definitely caused by a simultaneous switching of more than one dot. Hence, the switching of single dots cannot explain the finding and correlated switching has to be assumed.

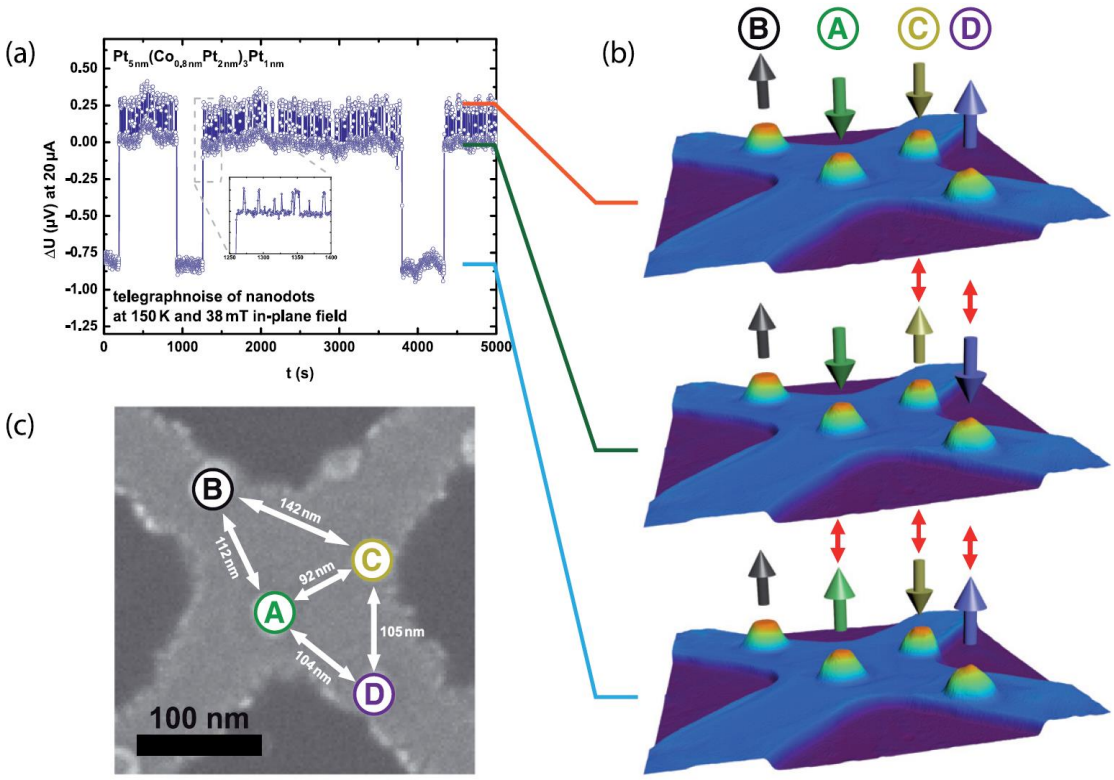

Figure 3.5: Graphic display of the telegraph noise and the associated magnetic states of the system of four nanodots. (a) Dynamical evolution of the nanodot magnetization for the relevant, critical magnetic in-plane field of 38 mT over a large period of time (80 minutes). It is obvious that the overall signal switches between three levels of signal height. A detailed combinatorial analysis of the jump heights and the expected dynamical behavior from single dot measurements is described in panel (b). (c) Local SEM micrograph of the Hall cross. The inter-dot separation is indicated in white. The B-D inter-dot distance is 209 nm.

3.2.3 Energy landscape and dynamical correlation function

In order to get better insight into the highly complex energy landscape of the ensemble of nanodots, I performed simulations in the framework of Landau - Lifshitz - Gilbert spin dynamics, including a stochastic Gaussian distributed field [24], modelling temperature effects via an additive Langevin noise term. For this purpose, the dots have been treated as macroscopic dipoles. This approximation is motivated by the strong exchange interaction between the constituting atoms of the dots and the high J/K ratio, that prevents the formation of domain walls. The exact same spatial arrangement of four dots has been modeled and the dynamics of the switching behavior analyzed. In agreement with the experimental results, I have found that the dynamical behavior of the four dots is quite different from calculations based on the energy barriers as determined from the temperature dependent coercive fields of individual magnetic particles. The predominantly occupied magnetic state is the one which minimizes the dipolar energy and can be seen in the middle panel of figure 3.5(b). The dynamical calculations, however, clearly indicated that this state is twofold degenerated with respect to the orientation of the dots D and C. This means, that on the timescale at which the dots A and B remain locked in the respective orientations, the dots D and C realize many switching events between configurations of upper and middle panels of figure 3.5 (b). This result raises the decisive question of whether this instability may explain the deviation of the energy barriers from those of individual, decoupled magnetic dots.

In full generality, one can only answer this question by investigating the complete energy landscape of the ensemble. This proves to be a tremendous task, since the energy landscape is nine-dimensional (the magnetization of each macroscopic dipole i can be described by two spherical coordinates $(\theta_i,\ \varphi_i)$ plus time). A way to solve this problem is to analyze the dynamical correlation function $C_{\mathrm{dyn}} = 1/T \int_{-\infty}^{\infty} dt\ S_{z,i}(t) S_{z,j}(t+s)$ between pairs of magnetic moments i and j, where $S_{z,i(j)}$ is the z-component of magnetization of moment i and j at times t and $t+s$, respectively. This function provides the information whether a given state is still correlated after a delay time s. Hence, $|C_{\mathrm{dyn}}| \rightarrow 1$ corresponds to the correlated, in-phase switching, while $C_{\mathrm{dyn}} \rightarrow 0$ to stochastic noise. In the simulations, this function was calculated for vanishing delay $s = 0$ and variable center-to-center distances r_{ij} to check for the degree of correlation for simultaneous switching. The dependence of the function $C_{\mathrm{dyn}}\left(r_{ij}^3\right)$ on dot separation is given in figure 3.6. The distance scale in the simulation is comparable to the length scale of the experiment and chosen

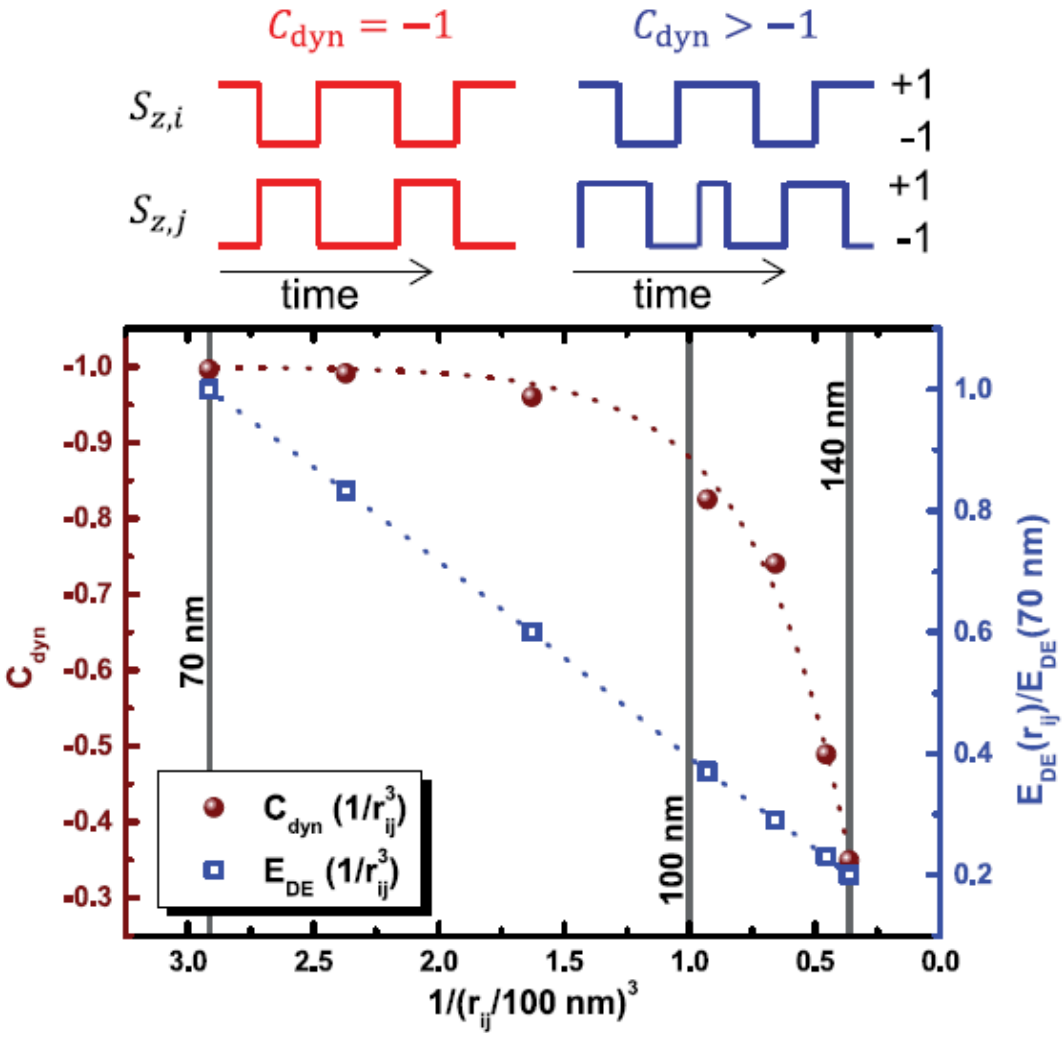

Figure 3.6: Simulations of the dynamical correlation function C_{dyn} and the decrease of dipolar energy E_{DE} plotted as a function of the inter-particle distance. The decrease of the dynamical correlations (red spheres) and the decrease of the dipolar coupling energy is normalized to the range of 70 nm to 140 nm which corresponds to typical inter-dot distances on the Hall cross. The dipolar energy decreases linearly due to the x-axis, being scaled as $1/r_{ij}^3$, normalized to 100 nm. The dynamical correlations decrease more slowly and amount to persistent antiferromagnetic coupling of the dots. This functional form is not dependent on the value of the damping parameter (here $\alpha :=0.2$ is chosen which is close to the value of Co/Pt dots for which the magnetization dynamics can be reasonably approximated by the LLG-Equation). All dotted curves are guides to the eye.

to be 100 nm (see also figure 3.5(c)). In figure 3.6 the spheres give the time-averaged dynamical correlation, while the open squares show the decrease of the strength of dipolar interaction with $1/r_{ij}^3$ (dotted curves as guide to the eye) for comparison. The plot clearly shows that the dynamical correlation C_{dyn} decreases much slower than the static dipolar coupling. For the separation of dots C and D (105 nm) the correlation function is still more than 0.8 and thus correlated switching is found. Hence, these two dots are switching in-phase and the stability of the anti-parallel configuration is increased. Even the farther separated dots $(r_{ij} \approx 140\ \mathrm{nm})$ show strong correlations (see figure 4) which is responsible for the occasional switching of dot A although its anisotropy energy is much larger than the dipolar energy. The physical reason for the long range phenomenon is the minimization of the time-averaged or -integrated total potential energy of all dots. This manifests in the many-body dynamical correlations and prevents the magnetic moments from dephasing. In other words, the many-body dynamical effects, described here experimentally and theoretically, correspond to a minimization of a dynamical quantity, the spin dynamical version of the action, rather than to a mere minimization of single particle energies in a static viewpoint for individual dots.

I illustrated that fact further by fig. (3.7) which uses the same distance scaling, as fig. (3.6) for the x-axis. The figure illustrates the large amount of action S, accumulated by single reversal in the presence of a static magnetic dipole source at some distance $r_{i,j}$. It is remarkable that despite the presence of noise and dissipation such a conceptually simple action-based *ansatz* which only strictly applies for exact Hamiltonian systems grants such a good explanation for the collective behavior of the dots in the simulations.

With the result of the theoretical analysis it becomes clear that the fast switching between the middle and upper voltage level is a correlated switching of dots C and D. From the hysteresis measurement in figure 2(a) a signal height of $(0.32 \pm 0.06)\ \mu$V has to be expected, taking the field induced canting into consideration. A complete analysis of all transitions between all possible states reveals that the scenario proposed in figure 3.4 is the one that comes closest to the experimentally observed value concerning level separation. Both the theoretical and experimental results prove unambiguously that it is crucial to know very accurately the magnetic behavior of the dots in the surrounding on a scale that is far beyond the separation of nearest neighbors, to properly describe thermal switching or switching field distributions.

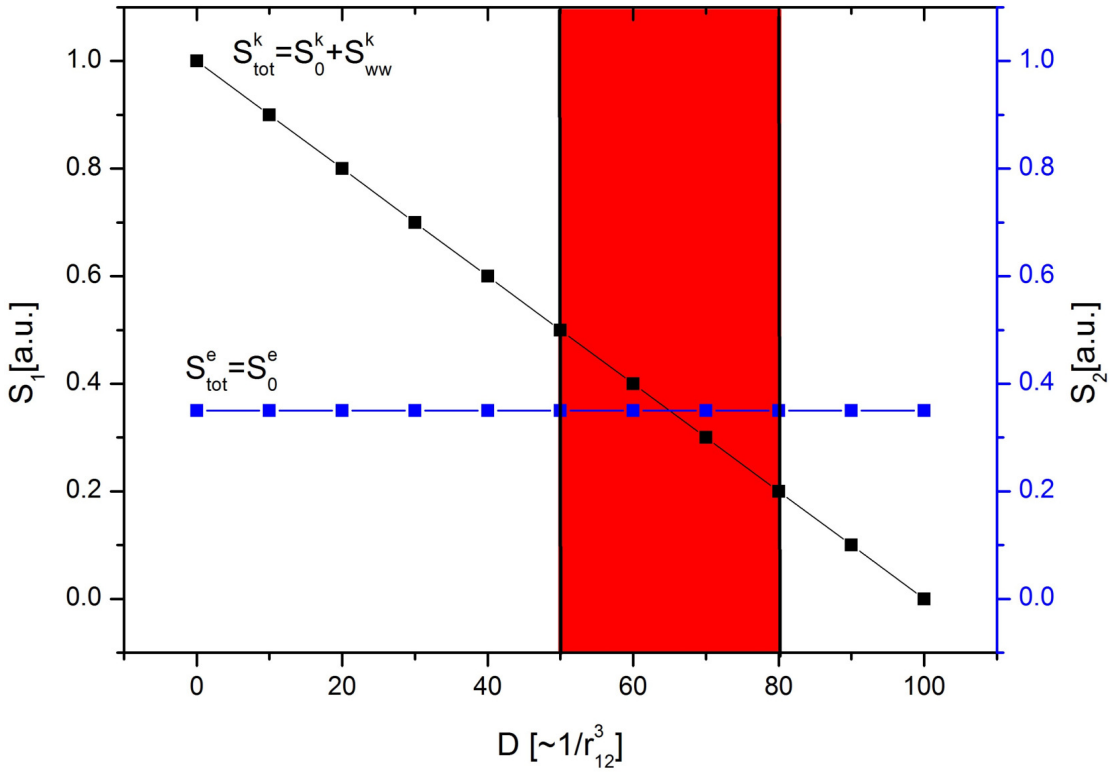

Figure 3.7: Comparison of the expected accumulated action for a reversal path of a single nanodot (blue) and for the reversal in the presence of a second nanodot at a distance, as prescribed by the x-axis (normalized to cubic inverse inter-dot distance). The numerical value of the action is not affected by isolated reversal, but rises linearly with decreasing inter-dot distance. This makes isolated switching increasingly unfavorable for nearby magnetic environments of a nanodot.

Finally, I would like to comment on the frequency decrease of switching when changing the field from 38 mT to 40 mT in figure 3.2 (b). The latter is an indication for some asymmetry in our experimental set-up, in particular a small misalignment of the external field, which favors one over the other state. The effect of the misaligned field is also seen in the room temperature measurements (figure 3.1(b)) where the switching between the two states with same energy is slightly asymmetric in time.

3.2.4 Systematic tuning of switching properties

In this subsection, we demonstrate how the two-spin correlation function can be tuned by varying different parameters in a small system of interacting dipolar particles. Additionally, we discuss our results in the context of interacting magnetic oscillators to understand the dynamic behavior in the limiting cases of small and large interaction energy E_{dd}.

3.2.5 Numerical results for a 4-particle-array

Particularly important for future applications of storage devices is external control or even mastery over switching properties of selected nanoparticles inside an array. We investigated the impact of the magnetostatic interaction of four particles on a length scale that is several times larger than the particle size and we were able to show that even on such a scale there is mutual influence on the switching rate. In order to quantify the influence of the interaction, we calculated the average switching rate $\nu_{\text{free,i}}$ of the i-th particle in the absence of interaction fields and compared this number with switching rate $\nu_{\text{j,i}}$ of the i-th particle in the presence of an interaction field of particle j. We encoded this ratio into a square matrix

$$M_{int,ij} = \begin{pmatrix} M_{11} & M_{12} & \dots & M_{1N} \\ M_{21} & M_{22} & \dots & M_{2N} \\ \vdots & \vdots & \dots & \vdots \\ M_{N1} & M_{N2} & \dots & M_{nn} \end{pmatrix} \tag{3.1}$$

with matrix elements $M_{ij} = \frac{\nu_{\text{free,i}}}{\nu_{\text{j,i}}}$. This matrix characterizes the mutual influence on the switching rate of the N interacting particles and has therefore dimension N. In order to account for

many-body interactions (e.g. the influence of particle i by particles j and k in terms of a resulting frequency shift), $M_{int,ij}$ can be generalized to a tensor $M_{int,i,j,k,...}$ with N indices. The influence of particle i, quantified by $\frac{M_{int,i,j,k,...}-M_{i,i}}{M_{int,i,j,k,...}}$, is then determined by summation over all indices $j, k, \ldots$ and results in

$$\sum_{j,k,...} M_{i,j,k,...} = \sum_{k=1}^{N-1} \binom{N-1}{k} \tag{3.2}$$

distinguishable matrix elements for each value of i.

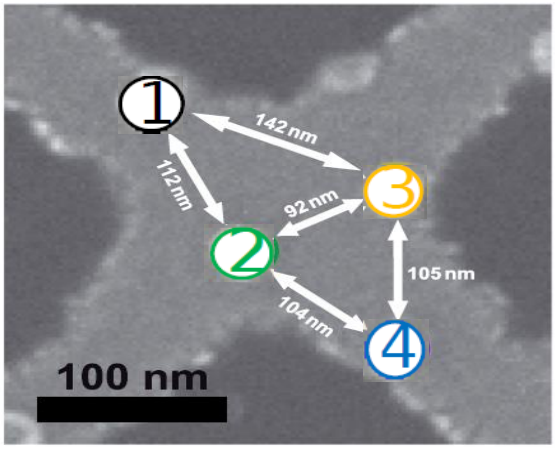

Figure 3.8: System of four Co/Pt magnetic nanodots on a Hall-cross [1]. The geometry of the system inspired the theoretical study on the correlation of the dots.

Motivated by an experimental study [1], we exemplify this scheme by evaluating all matrix elements for four magnetostatically coupled particles with different anisotropies K_1=21.73 $k_\mathrm{B}T$, K_2=11.07 $k_\mathrm{B}T$, K_3=5.47 $k_\mathrm{B}T$ and K_4=2.67 $k_\mathrm{B}T$ and different distances, ranging from approximately 3 to 5 times the particles' diameter (figure 3.8). The effective magnetic moments of all particles have been assumed to be $\mu_\mathrm{s} = 3.7 \cdot 10^5 \mu_\mathrm{B}$. The asymmetric choice of parameters helps to discuss the full complexity of the problem. It also accounts for the different size of artificially produced nanoparticles as well as their individual shape anisotropy [14, 15].

For the given example, the matrix (3.1) reads as

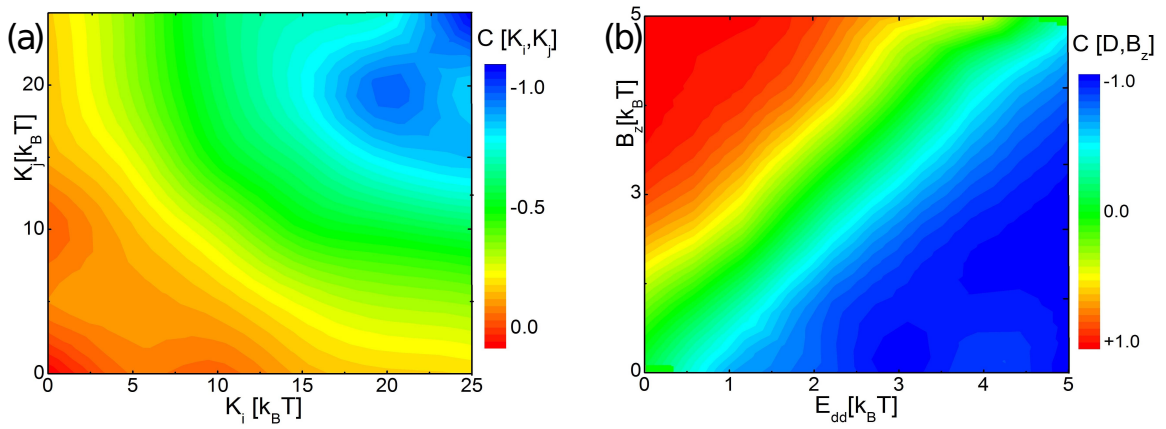

Figure 3.9: (a) Anisotropy of particle i vs anisotropy of particle j for a reference dipolar energy $E_{dd} = k_B T$. The external field is set to $\vec{B} = \vec{0}$ for all simulation points in this diagram. (b) Dipolar energy E_{dd} plotted against an external field aligned parallel to the z-axis. The competition of dipolar interaction field which favors anti-parallel alignment and external field which favors parallel alignment of the magnetization vectors is illustrated by the contour lines.

$$M_{int,ij} = \begin{pmatrix} 1 & 3.053 & 7.064 & 5.667 \\ 1.005 & 1 & 1.207 & 1.008 \\ 1.043 & 1.002 & 1 & 1.094 \\ 1.040 & 1.000 & 1.120 & 1 \end{pmatrix} \tag{3.3}$$

with vanishing self-interaction; i.e., diagonal elements M_{ii} are exactly 1.

It can be immediately extracted from (3.3) that the particle with the highest anisotropy K_1 dramatically enlarges the switching frequency of all the other particles, while it retains its own free switching frequency $\nu_{\text{free},1}$ to a very high degree. This effect is to some extent inherited by the rest of the particles: The particle with second-largest anisotropy K_2 still causes relative deviations of the switching frequency of particle with K_3 but not vice versa. The deviations from diagonal elements of (3.3) almost vanish when we are looking towards the subspace of particles 3 and 4 which are almost on equal footage with respect to the matrix elements $M_{3,4}$ and $M_{4,3}$. In this manner, switching can be observed with a certain hierarchy: Particle 1 manipulates the dynamics of particle 2. Particle 2 manipulates the dynamics of particle 3 and so forth (although this manipulation breaks down at some critical anisotropy/distance value).

Additionally, we calculated the two-spin correlation-function in dependence of different ratios for selected parameters, arising from the considered Hamiltonian.

Figure 3.9 (a) reveals the mutual influence of two spins with different anisotropies. Anti-parallel alignment is clearly favored for spins with strong anisotropy, while it almost vanishes for spins with small anisotropy-values. This diagram reflects the matrix elements of (3.3), because the relative deviations in switching frequencies of the different particles can be used to estimate the two-spin correlation function between them.

In figure 3.9 (b), the two-spin correlation function for a static magnetic z-field and dipolar interaction is shown. On the considered time scale, spin i is chosen to have stable orientation parallel to the z-direction, while the spin j tries to align in the opposite direction. Because of the vanishing two-spin correlation function along the diagonal of the diagram, it is very simple to negate the influence of a dipolar field by applying a suitable counter field B_z=-$H_{int,i}$ where $H_{int,i}$ is the dipolar interaction field of particle i acting on particle j.

3.2.6 Interacting magnetic oscillators

In this subsection, we want to discuss the results from the matrix (3.3) in terms of coupled magnetic oscillators which are well known from the literature (e.g. [136, 137, 138]) and have a formal basis in the context of Holstein-Primakoff-transformations [134, 135]. This can be motivated in the anisotropic ($\frac{K}{k_B T}$ >>1) single-particle-picture, where the energy landscape takes the quadratic form

$$E = E_i = -KS_{z,i}^2 \tag{3.4}$$

and leads to an average switching frequency ν (due to thermal activation) in the limit of $t \to \infty$, allowing for a Fourier (half-) expansion after an infinite number of oscillators

$$Z(\beta) = \sum_{n=0}^{\infty} \exp[-i\beta(n + 1/2)\nu] \tag{3.5}$$

that models a corresponding canonical ensemble (h:=1).

The analogy to the oscillator representation becomes also visible in the partition function of equality (3.20), if we add four regularization factors $0 < K_\nu << 1$ for the spin-components $S_{x,1}, S_{x,2}, S_{y,1}$

and $S_{y,2}$ to get a quadratic form in all cartesian components. The energy then reads as

$$\mathcal{H} = -\vec{K}_1\vec{S}_1^2 + J\vec{S}_1\vec{S}_2 - \vec{K}_2\vec{S}_2^2 \tag{3.6}$$

with vectors $\vec{K}_i$:=$(K_{x,i}, K_{y,i}, K_{z,i})$ and $\vec{S^2}$:=(S_x^2, S_y^2, S_z^2).
The equation (3.6) can be diagonalized straightforwardly and results in an expression

$$\mathcal{H}_{diag} = -\vec{K'}_1\vec{S'}_1^2 - \vec{K'}_2\vec{S'}_2^2 \tag{3.7}$$

for two decoupled 3D magnetic oscillators in the sense of (3.5) with normal coordinates. Here, $\vec{K'}_1$ and $\vec{K'}_2$ contain the information about the coupling.

A typical case, discussed in the literature, is a linear coupling of two mechanical oscillators which leads to two normal mode solutions: a) in phase-oscillation; b) anti-phase-oscillation or a superposition, resulting in a time-dependent energy transfer, also known as "beat". This beat is maintained by the mechanical spring that transfers kinetic energy from oscillator 1 to oscillator 2 and vice versa. It is interesting to see whether the magnetic coupling shows a similar behavior or not.

In the case of a small magnet with uniaxial anisotropy, the oscillatory magnetization dynamics of S_z is a result of constant thermal activation and a diffusive motion over a quadratic energy barrier instead of a continuous energy transfer between potential and kinetic energy (there is in fact no intrinsic "directional" kinetic energy present, but only Gaussian distributed thermal energy). For a coupled pair, there is no apparent reason why a magnet i should be prefered over another magnet j in terms of the influence on the switching frequency ν_{ij} or ν_{ji} respectively. A first look at the two particle subspace in the matrix (3.3) with $K_i \geq K_j$ suggests that coupled magnetic oscillators behave qualitatively different from linearly coupled harmonic oscillators, as the matrix elements are asymmetric. For example, the element $M_{3,2}$ of matrix (3.3) is 7 times larger than the diagonal elements $M_{i,i} = 1$. Formally, this difference can be regarded as an energy loss or a "dissipative channel". The described asymmetry calls for a dynamical explanation which can be given by the difference in thermal stability of the magnets with different anisotropy. First, we concentrate on the weak coupling regime, in terms of interaction energy E_{dd}. The averaged time-dependent dipolar interaction field of particle i, acting on particle j is

$$\langle \vec{H}_{int,i} \rangle_t = \frac{1}{T} \int_{t_1}^{t_2} dt \vec{H}_{int,i}. \tag{3.8}$$

For sufficiently long periods of time $T = t_2 - t_1 >> \tau_r$, the magnitude of $\langle \vec{H}_{int,i} \rangle_t$ is larger for a magnet with $K_i > K_j$. Therefore, short time correlations are ruled out and a time-averaged influence on a time scale $T >> \tau_r$ becomes important. In this manner, a magnet i forces a magnet j with $K_j < K_i$ to align in its time-dependent interaction field and not vice versa.
However, if the coupling is sufficiently large ($\frac{E_{dd}}{k_B T} >> 1$) the two particles switch collectively which is qualitatively similar to anti-phase oscillations in the more simple mechanical analogon, mentioned above. In this case, short time correlations increase significantly and the long-time dynamical asymmetry of the alignment vanishes. The increased switching rate of both magnets can be understood very well in the picture of a reduced energy barrier

$$E^{\text{Barrier}} = E^{\text{Anisotropy}} - 2\frac{D}{r_{ij}^3} \tag{3.9}$$

emerging from an alignment of the spin-vectors parallel to the x-axis of the system when passing the hard plane of the system, as discussed further above in chapter 3.

3.2.7 Conclusion

In summary, I have shown that magnetostatic interactions can play a significant and important role in the dynamic reversal process of magnetic nanoparticles even when the system's energy is dominated by anisotropy barriers. The observed switching behavior leads to the conclusion that correlations determine the switching. Dynamical processes have been observed that are clearly in contradiction to a single particle switching scenario. Wrong interpretations can be obtained, if only single particles are in the focus of study, neglecting the temporal behavior of the surrounding magnetization degrees of freedom and corresponding correlations. The spin-dynamical-simulations of hysteresis loops, telegraph noise and the supplementary calculations of the dynamical correlation function prove that dynamic correlations facilitate new reversal paths through the multidimensional energy landscape. This phenomenon finds a quite natural explanation in terms of action minimization and saddle point transition in the energy landscape. The farest reaching theoretical outcome is

that dynamical correlations are decreasing slower than the static interactions, responsible for this behavior (long range dipolar fields). This was considered as a behavior analogous to that of a dynamical phase transition. It follows that correlations become imminent when a magnetic system is close to the state of thermal instability and the dipolar energies of inter-dot coupling are of the same order of magnitude as the thermal fields. The simulations demonstrate that the interactions cannot be disregarded when thermally assisted switching with low effective barrier heights is the focus of interest, which has wide ranging implications for the research of superparamagnetism as well as technical applications, such as heat or thermally assisted magnetic recording.

3.3 Dynamical phases of interacting nanoparticles

After investigating the experimental situation of interacting nanodots in (3.2) this chapter will be continued with a section on a possible dynamical manifestation of a phase transition between classically interacting magnetic particles. This is motivated by the dynamical correlation function (3.2.3) and its functional behavior as a function of interaction strength and inter-particle distance.

A brief introduction to general dynamical phase transitions is given in (3.3.1) and then the idealized modelling of a system of exchange interacting magnetic moments is presented in (3.3.2 and 3.3.3). This simplification is justified by antiferromagnetic ground state properties of a pair of dipoles with large out-of-plane uniaxial anisotropy energy $E_{\mathrm{K}_\perp} >> E_{dd}$ (compare (2.10) and (2.4) for the notation).

A short conclusion (3.3.4) is presented at the end of the section.

3.3.1 Dynamic phase transition in linear response and Landau theory

Dynamical phase transitions are well known in the framework of the Landau-theory, which is closely related to the mean-field-theory [151, 139]. The theory predominantly deals with non-equilibrium stochastic systems subject to an oscillating magnetic field $h(t)$ with period T. A prominent system, undergoing such a phase transition, is the kinetic Ising-model which shows two characteristic phases, originally analyzed numerically by Tania and Oliveria [125] in the context of Glauber-dynamics [128]: (a) A symmetry restoring oscillation or *paramagnetic phase* and

(b) a symmetry breaking oscillation or *ferromagnetic phase*. The transition between these phases is intimately linked to both, the exact magnitude and the frequency $\omega = 2\pi/T$ of the oscillating external field. Typically, the time-dependent magnetization $m(t)$, averaged over one period of the external magnetic field serves as the dynamical order parameter Q of the system, hence

$$Q = \frac{1}{T} \oint dt\, m(t). \tag{3.10}$$

This is in contrast to the volume averaged order parameter

$$M = \frac{1}{V} \int dV m(V), \tag{3.11}$$

used for the description of a static phase transition. This order parameter can be obtained as an ensemble-average, calculated by ordinary Monte-Carlo simulations. In figure 1 (b), we qualitatively reproduced the two phases found in [125] within the framework of our dynamic model, introduced in section (4.2), using an exchange interaction, as well as a static external field to symmetrize the ferromagnetic phase.

Very recently, the more general case of $h(t)$ being superimposed by a static external bias field h_b, was studied and it was shown that h_b serves as a conjugate field with respect to the order parameter Q [120].

The dynamical correlation function C_{lit}, proposed in the literature [148], which describes the time-averaged overlap of the magnetization $m(t)$ with the oscillating field $h(t)$ is

$$C_{lit} \propto \oint m(t)h(t)dt = h_0 \oint m(t)\sin(\omega t)dt \tag{3.12}$$

from which the order parameter Q can be obtained with little difficulty. In our case, we want to describe the correlation between two dipolarly coupled magnetic moments. The main difference is the dynamical, *a priori* non-periodic, character of the time-dependent dipolar fields which is due to the interaction of the magnetic moments and due to the fact that both moments are evaluated in the superparamagnetic regime. Therefore, we can expect qualitatively different results when evaluating our correlation function $\mathcal{C}$.

3.3.2 Dynamical phase transition for two interacting magnetic moments

The dynamical phase transition, described in this section, arises from the coupling of different magnetic moments and is not maintained by an external field. The evolution of the presented system can thus not be described within the linear response theory as the previously studied systems [125, 129, 130, 131, 132]. We start the discussion of this phenomenon by introducing a proper correlation function which is similar to (3.12), but replaces the magnetization $m(t)$ by the z-component of a time-dependent spin vector $S_{z,1}(t)$ and the external field $h(t)$ by another spin-vector $S_{z,2}(t)$. This gives rise to the self-organized behavior of the system. Furthermore, we will regard the correlation function as the order parameter of the system, because we are interested in the mutual response of the two spin components as a function of time. In the following, numerical representation of the time dependence of the two vectors is described by an additional index k, running from 1 to $M >> 1$, hence by the expressions $S^k_{z,1}, S^k_{z,2}$.

Figure 3.10 shows the correlation function $\mathcal{C}$, calculated numerically for M time steps via the expression

$$\mathcal{C} = \sum_{k=1}^{M} \frac{S^k_{z,i} S^k_{z,j}}{[S^k_{z,l}]^2} \quad l = i, \text{if } S^k_{z,i} > S^k_{z,j}, \text{else} : l = j \tag{3.13}$$

$$= \int ds \; S_{z,i}(s) \cdot S_{z,i}(t+s) \tag{3.14}$$

of the z-components of two dipolarly coupled nanoparticles i and j as a function of the cubic inverse inter-particle distance r_{ij}^{-3} evaluated at vanishing time difference s=0. Almost the same functional dependence holds for antiferromagnetically coupled nanoparticles, if one assumes a hypothetical cubic inverse distance dependence for the coupling. This clearly underlines the similarity of dipolar and antiferromagnetic energy terms under the given boundary conditions of large anisotropy and we will pick this up in section 3.3.3. As it can be seen from figure 3.10, $\mathcal{C}$ goes to zero with some potency of the coupling strength. The strength of the coupling in contrast reveals a linear dependence on $\frac{1}{r_{ij}^3}$ in this kind of plot. It means that the dynamical correlation function decreases much slower than the interaction strength. In other words, the switching magnetic moments are strongly correlated at distances, where the interaction strength almost vanishes.

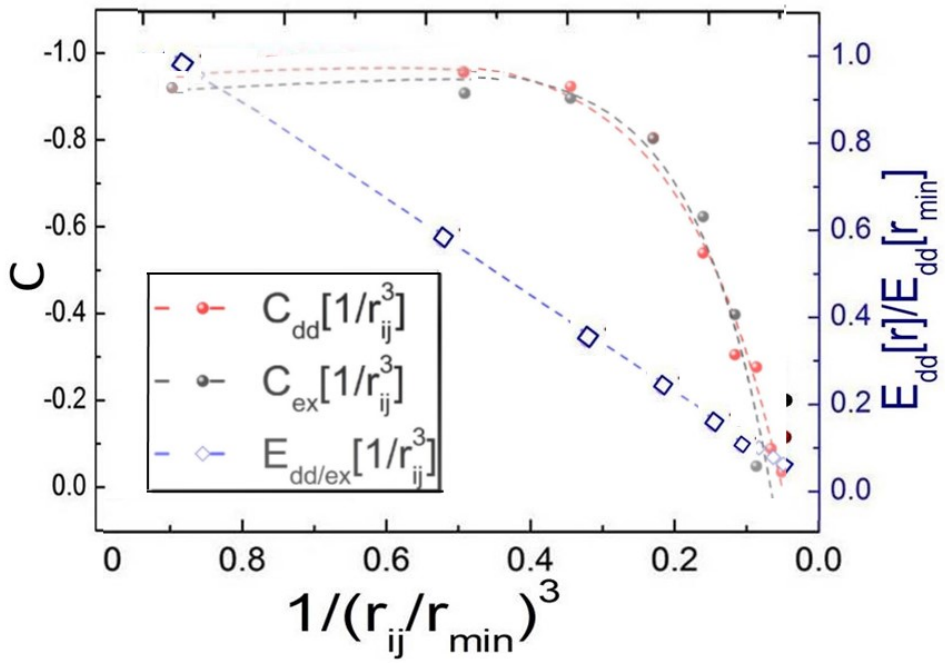

Figure 3.10: Two-spin correlation function $\mathcal{C}$ for dipolarly interacting nanoparticles with $K_1 = K_2 = 20\,k_BT$ as a function of the cubic inverse distance (red), starting from a critical distance r_{min} where $\mathcal{C}$ starts to deviate from -1 . The order parameter $\mathcal{C}$ goes to zero for larger distances. A very similar functional dependence $\mathcal{C}(r_{1,2})$ holds for antiferromagnetic exchange coupling (black), for which the same distance dependence was assumed. The linear dependence of the dipolar and exchange energy on $1/r_{ij}^3$ is also plotted for comparison (blue).

In the limit of strong coupling, the relative difference in all cartesian components $\alpha = x, y, z$ of the spins

$$|S_i^\alpha - S_j^\alpha| = 2S_i^\alpha = 2S_j^\alpha \tag{3.15}$$

is a strictly additive property ($\forall t$), while in the limit of vanishing coupling the difference is uniformly distributed, i.e.

$$0 \leq |S_i^\alpha - S_j^\alpha| \leq 2. \tag{3.16}$$

Hence, the power-law of $\mathcal{C}(\frac{1}{r_{ij}^3})$ has to be hidden in the dynamics of the system under investigation. The shape of the function $\mathcal{C}(\frac{1}{r_{ij}^3})$ resembles the decrease of magnetization of a ferromagnet as a function of increasing temperature, describing a continuous phase transition. In the next section, we analyze whether it is possible to define a dynamical phase transition for a very small system of

two coupled superparamagnetic particles.

3.3.3 Statistical description of a dynamic phase transition

The proper definition of any phase transition relies on an ensemble description. In order to characterize a phase transition in a system with a small number of particles, a corresponding ensemble description has to be found. For that purpose, we develop a general scheme, containing two steps. At first, we demonstrate how to simplify the Hamiltonian of the dynamical system and then we demonstrate how to map the model onto a lattice problem with many degrees of freedom.

Simplification of the Hamiltonian

To ensure the equivalence of an initial and simplified model, reliable boundary conditions have to be formulated and satisfied. We elaborate these boundary conditions by introducing a probability function

$$P(\theta_{op}) = [P(\theta_0), \ldots, P(\theta_\pi)] \tag{3.17}$$

which measures the canonical weight, obtained from the corresponding partition function, of all spin configurations with a given angle θ_{op}; i.e., an opening angle. Different states of this function are characterized by different angles $\theta_{op} \in [0, \pi]$. The correlation function $\mathcal{C}$, derived from (3.17) is positive for all $\theta_o < \frac{\pi}{2} - \frac{\epsilon}{2}$ $\left(C^{>0} = \int_0^{\pi/2-\epsilon/2} d\theta_{op} P(\theta_{op})\right)$ and negative for all $\theta_{op} > \frac{\pi}{2} + \frac{\epsilon}{2}$ $\left(C^{<0} = \int_{\pi/2+\epsilon/2}^{\pi} d\theta_{op} P(\theta_{op})\right)$ with ϵ as an arbitrarily small number.

From these definitions, we can construct the correlation function

$$C := C^{0>} + C^{0<} = const, \tag{3.18}$$

which has to be identical for any two models to be compared within our analysis. In the following, we will demonstrate how the conservation of C can be recast into a continuity equation.

Since our simulations are stochastic in origin, we can assume ergodic behavior of our spin system for $t \to \infty$. Therefore, it is possible to express the two-spin correlation function for particles, aligned along the x-axis in real space, canonically via

$$\langle C\rangle_{can} = \sum_{config} (\vec{S}_i\vec{S}_j)_{config}\frac{\exp(-\beta\mathcal{H}_{config})}{Z(\beta)} \tag{3.19}$$

in terms of a canonical partition function

$$Z(\beta) = \sum_{a,b,c,d,e,f} \exp(-\beta\mathcal{H}_{a,b,c,d,e,f}) = \sum_{a,b,c,d,e,f} \exp\Big(-\beta\Big[-K\sum_{i=1}^{2}(S^e_{z,i})^2 + D[-2S^a_{x,1}S^b_{x,2} + S^c_{y,1}S^d_{y,2} + S^e_{z,1}S^f_{z,2}]\Big]\Big) \tag{3.20}$$

taking into account all possible configurations (=*config*) of the two spins, characterized by the indices $a, \ldots, f$.

The main reason for this mapping is that we try to understand our findings within the framework of a well-defined theory of phase transitions in statistical systems with many degrees of freedom [139, 140]. Another notable observation from figure (3.10), worth mentioning in this section, is that the two-spin correlation function for dipolarly coupled spins with strong uniaxial anisotropy K and exchange coupled spins are very similar when it is assumed that both model Hamiltonians share the same distance dependence. Moreover, we found that the two-spin correlation function of exchange coupled spins without anisotropy term, matches the two-spin correlation function of exchange coupled spins with uniaxial anisotropy when the exchange coupled spins have another distance dependence ($\neq 1/r_{12}^3$). Thus, the model with $K \neq 0$ (labeled "1") can be transformed into the model with $K = 0$ (labeled "2") by destroying negative correlation $C^{<0}$ for $\theta_0 \geq \frac{\pi}{2} + \frac{\epsilon}{2}$ via $f(\theta_0)$ and simultaneously create it for $\theta_0 \leq \frac{\pi}{2} - \frac{\epsilon}{2}$ via $g(\theta_0)$ in the form

$$\begin{aligned}
&\int_0^{\frac{\pi}{2}-\frac{\epsilon}{2}} d\theta_{op}\Big(P(\theta_{op})_1 + f(\theta_{op})\Big) \; - \int_{\frac{\pi}{2}+\frac{\epsilon}{2}}^{\pi} d\theta_{op}\Big(P(\theta_{op})_1 + g(\theta_{op})\Big) \\
&= \int_0^{\frac{\pi}{2}-\frac{\epsilon}{2}} d\theta_{op}\Big(P(\theta_{op})_2\Big) \; - \int_{\frac{\pi}{2}+\frac{\epsilon}{2}}^{\pi} d\theta_{op}\Big(P(\theta_{op})_2\Big)
\end{aligned} \tag{3.21}$$

with the boundary condition

$$\int_0^{\frac{\pi}{2}-\frac{\epsilon}{2}} d\theta_{op} f(\theta_{op}) - \int_{\frac{\pi}{2}+\frac{\epsilon}{2}}^{\pi} d\theta_{op} g(\theta_{op}) = 0 \tag{3.22}$$

to be fulfilled. Equation (3.22) thus reflects a vanishing net flow of total correlation

$$\nabla(C_f^{>0} + C_g^{<0}) = 0, \tag{3.23}$$

introduced by the functions f and g.Summarizing, we have a mapping

$$K > D > k_B T \leftrightarrow K > J > k_B T \leftrightarrow J' > k_B T$$

from effectively antiferromagnetic dynamics of dipolarly coupled spins with strong uniaxial anisotropy to antiferromagnetically coupled spins with vanishing anisotropy.

The partition function of the isotropic exchange Hamiltonian can be decomposed into the partition function for N paramagnets, subject to an external field $\vec{B}_i = J\vec{S}_i$ for the i-th paramagnet. Incorporating the effect of anisotropy from the original model results in an internal field, giving rise to a shifted Langevin-function $L \rightarrow L^{'}$ for the paramagnets. Because of the limiting case of $C \equiv 0$ for $r_{ij} \rightarrow 0$ the correlation function remains zero for field values $\frac{1}{N}\sum_{i=1}^{N} \vec{B}_i = \vec{B}$. The simplified partition function reads

$$\begin{aligned} Z(\beta)' &= \sum_{\alpha,\beta,\gamma,\delta,\epsilon,\phi} \exp(-\beta \mathcal{H}_{\alpha,\beta,\gamma,\delta,\epsilon,\phi}) \\ &= \sum_{\alpha,\beta,\gamma,\delta,\epsilon,\phi} \exp\Big(-\beta\Big[J'[S_{x,1}^{\alpha} S_{x,2}^{\beta} + S_{y,1}^{\gamma} S_{y,2}^{\delta} \\ &\quad + S_{z,1}^{\epsilon} S_{z,2}^{\phi}]\Big]\Big). \end{aligned} \tag{3.24}$$

with antiferromagnetic exchange constant J'. It is important to note, that the simplified model with $K = 0$ has spherical symmetry - something we will use later on. At very high values of J' the opening angle θ_{op} in the probability function $P(\theta_{op})$approaches zero. It means that the spin components of the moments 1 and 2 are related to each other by

$$S_{x,2} = S_{x,1} \pm \Delta S_x, S_{y,2} = S_{y,1} \pm \Delta S_y, S_{z,2} = S_{z,1} \pm \Delta S_z \tag{3.25}$$

with a small displacement $\Delta S_{\mu,\nu}$ ($\mu \in (x, y, z)$ and $\nu \in (1, 2)$) paying tribute to the observation (3.15) within the dynamics.

By decreasing J', the number of orientations of spin 2, contributing non-negligibly to the interaction with spin 1, increases steadily until the equation (3.16) is satisfied for the limiting case $J' = J_c$.

Mapping the small system onto a statistical system

Now, we map our small system of two interacting spins, expressed in a canonical partition function onto a statistical system with many degrees of freedom. To do so, we define a hypothetical Ising model with spins homogeneously distributed on a sphere with surface area $A_{sphere} = 4\pi r^2_{sphere}$ and *all* spins oriented perpendicularly to the surface. The spins are coupled via an effective ferromagnetic exchange interaction

$$J'' = \frac{J'}{r^{\kappa}} \; \forall \; \mathrm{r} \geq r_{sphere} \, , \text{ otherwise } J'' = 0 \tag{3.26}$$

with parameter κ, which determines the range of the interaction (see figure 3.11 d-f). We resort to a ferromagnetic model by virtue of simplicity and use the invariance of the underlying physics under a piecewise transformation of all source points of the exchange fields, generated by each spin site, to its respective antipode $(\theta_i, \phi_i) \rightarrow (-\theta_i, -\phi_i)$ which then corresponds to the antiferromagnetic case.

For the description of the evolution of the order parameter of section 3.3.2, only one configuration with *all* spins pointing either outwards or towards the surface is used to account for the spherical symmetry of the problem, achieved in the previous section (see figure 3.11 d-f). The distance dependence of the correlation function of equation (3.13) will be reflected in the statistical model by increasing the range of J'' via the decrease of the parameter $\kappa_{k=1,\ldots,k=n}$ in n discrete steps. The comparison of the two models is given in figure 3.11 (a-c) and (d-f) respectively.

For $J' >> J_c$, our dynamical 2-spin system (figure 3.11 a) with very sharp $P(\theta_{op})$ distribution envelops the ground state of the Ising model with a very short interaction range $\kappa = \kappa_1$, corresponding to a small surface area A_1 (figure 3.11 d). Within A_1 the normalized order parameter $\langle S_z \rangle_{A_1}$ approaches unity. This was also confirmed in extended Monte-Carlo simulations .

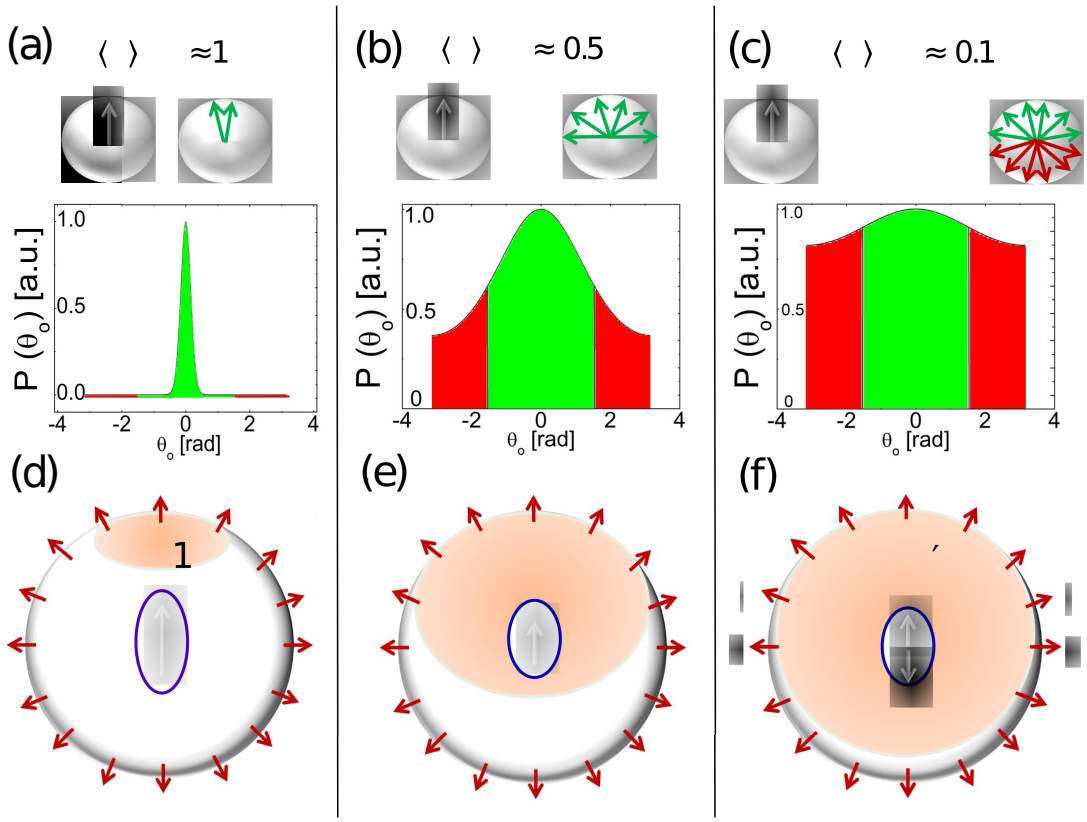

Figure 3.11: Modeling of the system of two interacting particles by means of the probability function (3.17) (top panels) and the corresponding spherical Ising model (bottom panels): **Top:** Effective coupling, experienced by a spin with arbitrary, but fixed orientation i on the sphere with another spin j of arbitrary orientation. Green color expresses positive correlations $C^{>0}$ while red color expresses negative correlations $C^{<0}$, resulting from different angles in the propability function $P(\theta_{op})$. (a) For strong interaction, there is only non-negligible weight of $P(\theta_{op})$ for configurations with small angles between possible spin orientations; i.e., the cone around the encircled spin. The number of contributing configurations rises with decreasing interaction, as seen in (b) and (c). **Bottom:** Corresponding model of parallel aligned Ising-spins, oriented along the surface normal at each position on the sphere. (d) A spin at position i experiences a large effective field (highlighted by the blue ellipsoid) from its environment. For $J >> J_c$ the area A_1 underlined in orange gives the interaction range. As the range of the interaction rises and curvature plays a role, the effective field at lattice site i is reduced, as seen in (e). Its value subsequently approaches zero in (f) towards the long-range limit ($\frac{|n-n'|}{n} \to 0$) of the interaction where the correlation length ζ diverges.

The decrease of J' in the 2-spin model results in a broadening of $P(\theta_{op})$ (fig. 3.11 b). This situation corresponds to an increase of the interaction range and the surface area A_k in the spherical model (figure 3.11 e) and, hence, to the decrease of the order parameter $\langle S_z \rangle_{A_k} < 1$ due to the curvature. Eventually, the system reaches a limit on the sphere and $\langle S_z \rangle_{A_n} \to 0$ as well as $A_n \to A_{sphere}$.

The introduced model allows us to map our $N = 2$ particle system with isotropic exchange interaction and N^2 possible states onto an N particle spherical Ising system. Hence, a proper statistical description of the dynamical phase transition can be achieved. From a more fundamental point of view, the decrease of the parameter κ (in combination with the curvature of the sphere) leads to a connection of initially disconnected regions of the phase space and thus naturally establishes a correlation length ζ which diverges in the above mentioned long-range limit for $\alpha \to \alpha_n$ when the order parameter $\langle S_z \rangle_{A_n} = 0$ vanishes. Thus, it is important to note that our approach is different from the mean field approximation. This is due to the fact that our dynamic correlation function $\mathcal{C}$ takes full account of the partition function of the system, which is not the case in the mean field theory, featuring only the most important state of a partition function in a self-consistent set of equations [141].

The above analysis demonstrates that despite the smallness of the numerical system the canonical correlation function $\langle C \rangle_{can}$ is suitable for the description of the dynamical phase transition, as it can be mapped onto the statistical system with order parameter $\langle S_z \rangle_{A_k}$ (for the k-th parameter κ_k) or equivalently the effective field generated at a particular lattice site i. Note, that the violation of ergodicity, usually discussed for the two ferromagnetic branches of the Ising-model below $T = T_c$ doesn't contradict with our assumption of ergodicity concerning the dynamic behavior, because the numerically found correlation function $\mathcal{C}$ includes information from the entire phase space volume; i.e., there is no spontaneous symmetry breaking within the dynamic description. Hence, the experimental or theoretical analysis of the telegraph noise of two coupled magnets as a function of distance gives a possibility to define a critical distance below which the particles become dynamically correlated. Moreover, the piecewise increase of the range of interaction, acting on the described Ising-state on a sphere, gives a more intuitive explanation for the increase of the correlation length ζ towards the critical point than in the 2-dimensional Ising-model, discussed extensively in the literature [33, 34, 35, 140] as a prototype for phase transitions in the field of magnetism. The described procedure from above can be applied to larger systems as well.

3.3.4 Conclusion

In this section, the effect of long-range interactions on the correlation behavior of two exchange-coupled particles has been investigated. We systematically calculated the correlation function $\mathcal{C}$ between the signals of two spin vectors over a wide variety of distances and found a continuous decrease of this time-averaged observable as well as a characteristic symmetry reduction. We propose a method that allows us to map the dynamics of a small number of particles onto a statistical ensemble of many static particles and, hence, to describe a dynamical phase transition. The established procedure for identifying the dynamical phase transition may serve as a prototype how to model the continuous decrease of any two-spin correlation function for a particular Hamiltonian. The first step of such a procedure exploits the possibility of an equivalent formulation of an original Hamiltonian via an isotropic exchange Hamiltonian by choosing well-suited auxiliary functions. The second step is then a model dependent transformation of the modified Hamiltonian on the spherical Ising model with varying range of interactions. The analysis of the correlation function allows for the conclusion that in the limit of strong interactions the particles behave "paramagnetic" with respect to the notions of the field induced DPT in Landau theory while they behave "ferromagnetic" in the limit of low interaction strength.

Chapter 4

Concept of non-trivial topological magnetic helices

4.1 Introduction

An increasingly active field of study in solid state and condensed matter physics on the nanoscale is devoted to the conceptualization, theoretical modelling and fabrication of applicational devices for purposes of energy efficient storage and processing of information. Utilization of the spin degree of freedom has been a particulary promising route in this direction and has benefited from substantial progress in measurement technology, such as spin-polarized scanning tunneling microscopy.

A limitation of several proposed research directions, such as spintronics, spin caloritronics or magnonics has been the neccessity of an interaction of the spin degrees with external agents (charges, heat currents, external fields) and a spin-charge conversion. More recent strategies aim towards an all-spin based use for storing and releasing magnetic information in nanoscopic objects. In this context, artificially produced micro- and nanoscopic dipolar systems allow for a variety of magnetic anisotropies in different spatial directions. Furthermore, attention is focused on atomic spin ensembles [29, 30], magnetic nanoarrays [31, 32, 36, 37], structured multilayers [44] and superlattices [39, 40], colloids [42], and molecular systems [43].
In particular, Ruderman-Kasuya-Kittel-Yoshida (RKKY) induced antiferromagnetic coupling has already been utilized to transmit the information of the state of an ”input” ferromagnetic dot to the ”gate” dot [28, 39] and a dependence of the magnetic ground state on the chain length has been

confirmed elsewhere [45].

The proposed concept of the energy storage and release is based on the use of metastable energy states. This idea has been employed since ancient times and is predominantly used in water mills to harness the energy of water in elevated states of potential energy and goes under the name of "hydropower" [60]. In anticipation of an age of depleted fossile energy ressources and ongoing climatic changes, such renewable and sustainable forms of energy supply gain importance in both public and scientific recognition [61]. This concept has also been pursuited for magnetic systems in [59] . In the following, this concept is transfered to magnetic chains and the manipulation of their phase space and energy landscape, respectively.

In this chapter, I present results on the size-dependent magnetic order in one-dimensional spin chains, stabilized through competition of exchange, RKKY or dipolar interactions and in-plane anisotropies, published in [53]. As the basic result, local energy minimum states manifest as integer twists of the magnetic configuration while local maxima are found in between those minima at half-integer twists. When modulated in one degree of freedom, topological protection manifests as an additional property and contributes to the magnitude of the involved energy barriers. Modulation of the spirals and helices by rotation of one terminal spin results in a periodic storage and release of magnetic energy, giving an opportunity for potential application in future storage devices.

4.1.1 Structure under consideration

All calculations are based on a x-directional linear chain of N dipoles with uniaxial or easy plane anisotropy which are coupled by ferromagnetic (FM) or antiferromagnetic (AFM) exchange, RKKY or dipolar interaction. This configuration corresponds to a chain of nanomagnetic islands, a stack of nanopillars or an atomic chain on a substrate. The anisotropy may arise from either magnetocrystalline anisotropy, particle shape or higher order multipolar contributions. The Hamiltonian of the system reads as

$$H = D\sum_{i,j}\frac{\vec{S}_i\vec{S}_j}{r_{ij}} - 3\frac{(\vec{S}_i\vec{r}_{ij})(\vec{S}_j\vec{r}_{ij})}{r_{ij}^5} - K\sum_i (S_i^x)^2, \tag{4.1}$$

where $\vec{S}_i$ is a three-dimensional unit spin vector, D is the dipolar coupling constant, K is the anisotropy constant, and $\vec{r}_{ij}$ is the distance between spin vectors i and j of the chain.

4.2 Energy minimization of magnetic spin chains

Before describing the procedure of how the magnetic helix states were modeled and manipulated, some theoretical background on the energy landscape of dipolar spin chains will be described.

In the following, we show how the (non-) collinear stable spiral states for the spin-chain can be constructed by an expansion after collinear solutions. We start with the simplest possible situation of two dipoles, a dimer. In this case only collinear solutions for stationary points (minima, maxima and saddle-points) arise. Then, we consider the more general case of N dipoles and deduce the amount of collinear solutions in this extended phase space from the solutions of the dimer. The collinear solutions of the chain with N dipoles are subsequently used to construct the (non-)collinear solutions.

Therefore, we consider (without loss of generality) a chain with N spins along the x-axis with normalized distance $r_{i,j} = x_{i,j} = 1,\ \forall\ |i-j| = 1$, and pure dipolar interaction between each spin-sites i and j.

$$\begin{aligned} E_{int} = & E_{i,j} = [\sin(\theta_i)\sin(\theta_j)\cdot[-2\cos(\phi_i)\cos(\phi_j) \\ & + \sin(\phi_i)\sin(\phi_j)] + \cos(\theta_i)\cos(\theta_j)]/(x_{ij})^3. \end{aligned} \tag{4.2}$$

We calculate the stationary points of the chain with generalized phase space coordinates q_k, expressed in terms of normalized spherical coordinates (θ_i, ϕ_i). This task requires the computation of the multidimensional gradient of the energy which must satisify

$$\vec{\nabla} \sum_{i,j}^{N} E_{i,j} = \vec{0} \tag{4.3}$$

The set of equations in (4.3) can be solved exactly for N=2 and results in 2^2 solutions along the x-axis ($\theta_1 = \theta_2 = \frac{\pi}{2}$ with angles $\phi_1 = \pm\phi_2 = 0, \frac{\pi}{2}, \pi$ or $\frac{3}{2}\pi$), 2^2 solutions along the z-axis ($\theta_1 = \theta_2 = 0$ or π), continuously degenerated in the ϕ_1- and ϕ_2-coordinates, as well as 2^2 solutions along the y-axis. An additional "ring" of degenerated solutions $\phi_1 = \pm\phi_2 = \frac{\pi}{2}$ or $\frac{3}{2}\,\pi\ \forall\ \theta_1 = \pm\theta_2$ can be constructed by a linear superposition of basis-solutions along the y- and z-axis and are thus not treated as basis-solutions.

We want to prove now that the many-body problem for collinear stationary points reduces to the dimer-problem by showing that each of the $(N-1)!$ pairs of coupled spins i and j satisfy the orthogonal sets of solutions of the dimer. Since we have a discrete lattice problem, bounded by a natural number N, we prove our statement by mathematical induction:
Our *basis* is realized by the N=3 problem which must satisfy

$$\begin{aligned}
\partial\theta_1(E_{1,2}+E_{1,3}) &= 0\\
\partial\phi_1(E_{1,2}+E_{1,3}) &= 0\\
\partial\theta_2(E_{2,1}+E_{2,3}) &= 0\\
\partial\phi_2(E_{2,1}+E_{2,3}) &= 0\\
\partial\theta_3(E_{3,2}+E_{3,1}) &= 0\\
\partial\phi_3(E_{3,2}+E_{3,1}) &= 0,
\end{aligned} \tag{4.4}$$

for all possible stationary points.
At this point, we utilize L'Hopital's rule [41] from one-dimensional mathematical analysis to approach the stationary points from different directions in the 6-dimensional phase space, inflicting several boundary conditions on the set of solutions for stationary points. In total, we have $5!$ different equations for different quotients $\frac{\partial q_k E}{\partial q_l E}$ which are (a priori) undefined, but can be expressed by second derivatives $\frac{\partial q_m \partial q_k E_{tot}}{\partial q_m \partial q_l E_{tot}}$, except for points in phase space, for which the second derivative of the denominator equals to zero without the trivial cases $k=l$. These additional derivatives ∂q_m just introduces a $\frac{\pi}{2}$-phase shift with respect to the periodic function in q_m in spherical coordinates. The advantage of calculating quotients is to cancel out distance dependences, as will be shown below. For example, the quotient $\frac{\partial\theta_1(E_{1,2}+E_{1,3})}{\partial\phi_1(E_{1,2}+E_{1,3})}$ can be calculated in 6 different ways:

$$\lim_{\theta_1\to\theta_1^s}\frac{\partial\theta_1(E_{13}+E_{12})}{\partial\phi_1(E_{13}+E_{12})} = \lim_{\theta_1\to\theta_1^s}\frac{\partial\theta_1\partial\theta_1(E_{13}+E_{12})}{\partial\theta_1\partial\phi_1(E_{13}+E_{12})} = \alpha \tag{4.5}$$

$$\lim_{\phi_1\to\phi_1^s}\frac{\partial\theta_1(E_{13}+E_{12})}{\partial\phi_1(E_{13}+E_{12})} = \lim_{\phi_1\to\phi_1^s}\frac{\partial\phi_1\partial\theta_1(E_{13}+E_{12})}{\partial\phi_1\partial\phi_1(E_{13}+E_{12})} = \beta \tag{4.6}$$

$$\lim_{\theta_2\to\theta_2^s}\frac{\partial\theta_1(E_{13}+E_{12})}{\partial\phi_1(E_{13}+E_{12})} = \lim_{\theta_2\to\theta_2^s}\frac{\partial\theta_2\partial\theta_1(E_{13}+E_{12})}{\partial\theta_2\partial\phi_1(E_{13}+E_{12})} = \gamma \tag{4.7}$$

$$\lim_{\phi_2 \to \phi_2^s} \frac{\partial \theta_1 (E_{13} + E_{12})}{\partial \phi_1 (E_{13} + E_{12})} = \lim_{\phi_2 \to \phi_2^s} \frac{\partial \phi_2 \partial \theta_1 (E_{13} + E_{12})}{\partial \phi_2 \partial \phi_1 (E_{13} + E_{12})} = \delta \tag{4.8}$$

$$\lim_{\theta_3 \to \theta_3^s} \frac{\partial \theta_1 (E_{13} + E_{12})}{\partial \phi_1 (E_{13} + E_{12})} = \lim_{\theta_3 \to \theta_3^s} \frac{\partial \theta_3 \partial \theta_1 (E_{13} + E_{12})}{\partial \theta_3 \partial \phi_1 (E_{13} + E_{12})} = \epsilon \tag{4.9}$$

$$\lim_{\phi_3 \to \phi_3^s} \frac{\partial \theta_1 (E_{13} + E_{12})}{\partial \phi_1 (E_{13} + E_{12})} = \lim_{\phi_3 \to \phi_3^s} \frac{\partial \phi_3 \partial \theta_1 (E_{13} + E_{12})}{\partial \phi_3 \partial \phi_1 (E_{13} + E_{12})} = \varphi \tag{4.10}$$

with $\alpha = \beta = \gamma = \delta = \epsilon = \varphi$. We arbitrarily compare the values for γ and ϵ. The quotient reduces to

$$\frac{\partial \theta_2 \partial \theta_1 (E_{1,2})}{\partial \theta_2 \partial \phi_1 (E_{1,2})} = \frac{\partial \theta_3 \partial \theta_1 (E_{1,3})}{\partial \theta_3 \partial \phi_1 (E_{1,3})} \tag{4.11}$$

and yields the constraint $\theta_2 = \theta_3$ or $\theta_2 = \theta_3 \pm \pi$, because the quotients only differ in coordinates θ_2 and θ_3. The same principle applies to the quotient of the values of δ and φ

$$\frac{\partial \phi_2 \partial \theta_1 (E_{1,2})}{\partial \phi_2 \partial \phi_1 (E_{1,2})} = \frac{\partial \phi_3 \partial \theta_1 (E_{1,3})}{\partial \phi_3 \partial \phi_1 (E_{1,3})} \tag{4.12}$$

and yields the constraint $\phi_2 = \phi_3$ or $\phi_2 = \phi_3 \pm \pi$. On the other hand, we can easily compute the identity

$$\begin{aligned} &\frac{\partial \theta_1 (E_{1,2} + E_{1,3})}{\partial \phi_1 (E_{1,2} + E_{1,3})} = \\ &= \frac{\partial \theta_2 \partial \theta_1 (E_{1,2} + E_{1,3})}{\partial \theta_2 \partial \phi_1 (E_{1,2} + E_{1,3})} = \frac{\partial \theta_2 \partial \theta_1 E_{1,2}}{\partial \theta_2 \partial \phi_1 E_{1,2}} = \frac{\partial \theta_1 E_{1,2}}{\partial \phi_1 E_{1,2}} \end{aligned} \tag{4.13}$$

which relates γ directly to the dimer-problem. This equation has two distinct sets of solutions for the constraints $|\theta_2 - \theta_3| = 0$ or $\pm\pi$, $|\phi_2 - \phi_3| = 0$ or $\pm\pi$ mentioned above. The π-shifted solution yields

$$\frac{\partial \theta_1 E_{1,2} + \partial \theta_1 E_{1,3}}{\partial \phi_1 E_{1,2} + \partial \phi_1 E_{1,3}} = \frac{0}{0} = \frac{\partial \theta_1 E_{1,2}}{\partial \phi_1 E_{1,2}} \tag{4.14}$$

and can be identified with the set of solutions for the dimer-problem. The other set of solutions results in the trivial identity

$$\frac{2\partial \theta_1 E_{1,3}}{2\partial \phi_1 E_{1,3}} = \frac{2\partial \theta_1 E_{1,2}}{2\partial \phi_1 E_{1,2}} = \frac{\partial \theta_1 E_{1,2}}{\partial \phi_1 E_{1,2}} \tag{4.15}$$

Hence, comparison with equation (4.14) and the fact that $0 = \partial \theta_1 E_{1,2}|_{\theta_1 = -\theta_2} = -\partial \theta_1 E_{1,2}|_{\theta_1 = \theta_2}$

yields that the second set of solutions also matches that of the dimer-problem. Permutating the different coordinates in phase space, e.g. making additional use of the values for α and β, and applying the same procedure as in equations (4.11) and (4.12) gives the analogue constraints for the variables of spin 1 ($\theta_1 = \pm\theta_2$ or $\pm\,\theta_3$). This results in 2^3 stationary points along the x-axis and 2^3 highly degenerated stationary points along the z-direction and 2^3 solutions along the y-axis $\phi_i = \pm\phi_j = \frac{\pi}{2}$ or $\frac{3\pi}{2}$ for $\theta_i = \theta_j = \frac{\pi}{2}$.

This scheme is also applicable to all cases $N > 3$ because a mixed second derivative $\partial q_m \partial q_n$ always reduces the quotients to one single interaction between spins at sites m and n.

We now assume the validity of the statement, proven for N=3, for arbitrarily large, but finite values of N. The induction step $N \to N+1$ is simply performed by using the additivity of the dipolar interaction

$$\begin{aligned}
\underbrace{\partial\theta_1(E_{1,1} + E_{1,2} + \cdots + E_{1,N})}_{=0} + \partial\theta_1 E_{1,N+1} &= 0 \\
\underbrace{\partial\phi_1(E_{1,1} + E_{1,2} + \cdots + E_{1,N})}_{=0} + \partial\phi_1 E_{1,N+1} &= 0 \\
\ldots &= 0 \\
\ldots &= 0 \\
\underbrace{\partial\theta_N(E_{N,1} + E_{N,2} + \cdots + E_{N,N})}_{=0} + \partial\theta_N E_{N,N+1} &= 0 \\
\underbrace{\partial\phi_N(E_{N,1} + E_{N,2} + \cdots + E_{N,N})}_{=0} + \partial\phi_N E_{N,N+1} &= 0 \\
\partial\theta_{N+1}(E_{N+1,1} + E_{N+1,2} + \cdots + E_{N+1,N}) &= 0 \\
\partial\phi_{N+1}(E_{N+1,1} + E_{N+1,2} + \cdots + E_{N+1,N}) &= 0
\end{aligned} \tag{4.16}$$

which evidently forces the derivative of the two-particle-interaction of the spin $N+1$ with all other spins to be zero by comparison of the coefficients. A substitution of variables with indices $i \leftrightarrow N+1$ shows that the remaining two derivatives do also vanish by virtue of symmetry. Summarized, there is a total number of 2^N collinear stationary points along each of the three cartesian axes, labeled by $\psi_{x,i}, \psi_{y,j}$ and $\psi_{z,k}$. This remains valid, even if we alter the magnetic moment of each spin-site individually, which is explored in the following.

At this point, we change to cartesian coordinates, since the basis-solutions coincide with the x,y and z-axes. We are able to express any point in the $3N$-dimensional phase space by a suitable superposition of the $2^N + 2^N + 2^N = 3 \cdot 2^N$ basis-solutions $\Psi_{x,i}$, $\Psi_{y,j}$ and $\Psi_{z,k}$ calculated above, e.g.

$$\begin{aligned}(S_{x,1}, S_{y,1}, S_{z,1}, \ldots, S_{x,N}, S_{y,N}, S_{z,N}) = \\ = \sum_{i=1}^{2^N} \alpha_{x,i}\Psi_{x,i} + \sum_{j=1}^{2^N} \alpha_{y,j}\Psi_{y,j} + \sum_{k=1}^{2^N} \alpha_{z,k}\Psi_{z,k}\end{aligned} \tag{4.17}$$

certainly including all possible non-collinear stationary points.

If we exploit the fact that the energy of any chain-configuration can be decomposed into interactions of the S_x-, S_y- and S_z-components, the task of finding non-collinear spiral states reduces to the determination of the coefficients $\alpha_{i,x}, \alpha_{j,y}$ and $\alpha_{k,z}$ to express the non-collinear basis-solutions by the collinear basis (resembling the task of calculating Clebsch-Gordan-coefficients to express coupled quantum spins in the basis of single quantum spins (for example [55]).

To make things even more transparent we use the decomposition into S_x, S_y and S_z-components with coefficients

$$\begin{aligned}(S_{x,1}, S_{x,2}, S_{x,3}, \ldots, S_{x,N}) &= \sum_{l=1}^{N} \beta_{x,l}\psi_{x,l} \\ (S_{y,1}, S_{y,2}, S_{y,3}, \ldots, S_{y,N}) &= \sum_{m=1}^{N} \beta_{y,m}\psi_{y,m} \\ (S_{z,1}, S_{z,2}, S_{z,3}, \ldots, S_{z,N}) &= \sum_{n=1}^{N} \beta_{z,n}\psi_{z,n}\end{aligned} \tag{4.18}$$

with $\Psi_{x,i}$=$[\psi_1, \psi_2, \ldots \psi_N]_{x,i}$, $\Psi_{y,j}$=$[\psi_1, \psi_2, \ldots \psi_N]_{y,j}$, $\Psi_{z,k}$=$[\psi_1, \psi_2, \ldots \psi_N]_{z,k}$ and coefficients $\beta_{x,i}, \beta_{y,j}, \beta_{z,k}$ which have an unambiguous relation to the coefficients $\alpha_{i,x}$, $\alpha_{j,y}$ and $\alpha_{k,z}$. If there is only one basis-set with non-zero coefficients, it corresponds to collinear solutions. A superposition of the different basis-sets with symmetric distribution of the coefficients with respect to the center of the chain for each set results in minima-states.

One example for N=5 is given by the component-resolved expansion

$$
\begin{aligned}
S_x &: 0 \rightarrow + \frac{1}{2} \leftarrow + 0 \rightarrow + \frac{1}{2} \rightarrow + 0 \rightarrow \\
S_y &: 0 \nearrow + \frac{1}{2} \swarrow + 1 \nearrow + \frac{1}{2} \swarrow + 0 \nearrow \\
S_z &: 1 \uparrow + \frac{1}{\sqrt{2}} \downarrow + 0 \uparrow + \frac{1}{\sqrt{2}} \uparrow + 1 \downarrow
\end{aligned}
\tag{4.19}
$$

and corresponds to a stable non-collinear spiral state.

In conclusion the number of stationary points for collinear states is $3 \cdot 2^N$. Since the calculation of the symmetric coefficients is in general not a straightforward task, we calculated them systematically by the modulation of the spirals, as explained in the subsection 4.3. The number of minima corresponds to all possible numbers of symmetric coefficients between 0 and N in the different basis-sets. A graphical model for a magnetic helix is shown in figure 4.1.

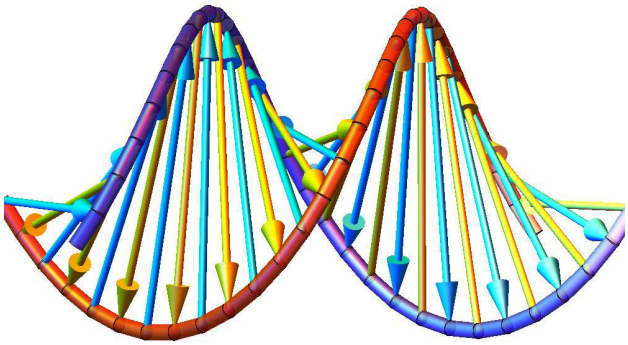

Figure 4.1: 2-dimensional projection of a 3-dimensional model of a magnetic helix. It is clearly visible how spin vectors simultaneously wind around two spatial directions, as parametrized by the two spherical angles ϕ and θ . The variation of the azimuthal angle is color-coded by blue and yellow spin vectors (”base-pairs”) while the variation of the polar angle is color-coded by a blue-red alteration of the ”back-bone” of the helix.

4.3 Theoretical model of spin spirals and helices

4.3.1 Search for stationary energy states of the spin chain

The following results are discussed for dipolar interaction (see 4.2) as the most generic form of interaction, but the formalism can be straightforwardly applied to the RKKY or (direct) exchange interaction, if needed.

All information about the saturation magnetization M_S of a particle is hidden in the dipolar interaction constant $D = \mu_0 M_s^2/2$, as defined in (4.1). At first, we look for the exact total number of critical points of Hamiltonian (1) solving the set of equations $\nabla \sum_{i,j}^{N} H = \vec{0}$ as was explained in the previous section (4.2). We reveal 3×2^N stationary points (minima, maxima, or saddle points) related to (non-)collinear solutions, and the question is what the magnetic configurations corresponding to these metastable states look like. To answer this question analytically, we utilize the method used for the construction of spin-spiral states. The magnetic structure is regarded as a superposition of spirals in the 2D Brillouin zone under the requirement of a constant magnetic moment at all sites. The energy of the constructed structure is then analyzed. The spin spirals can be described via vectors δ and q in the form (i) $\vec{S}(r) = \vec{S}[\sin(\delta r)\cos(qr), \sin(\delta r)\sin(qr), \cos(\delta r)]$ or (ii) $\vec{S}(r) = \vec{S}[\sin(\delta r), \sin(\delta r)\cos(qr)\cos(\delta r)]$. For q = 0 and $r \| \vec{O}\vec{x}$, for example, (i) gives a spin spiral $\vec{S}(x) = \sin(\delta x), 0, \cos(\delta x)]$ in the xz plane. The energy of this spin configuration as a function of δ is plotted as a dashed line in figure 4.2(a).

It is seen that the energy is minimal ($E_{min,1}$) at $\delta = \pi$, i.e., corresponds to the AFM alignment of neighboring spins and is known as the ground state of a chain with easy x-z plane [see figure 4.2(c)]. There is only one minimum in this case, and the envelope of the AFM structure Fig. 1(c) forms a straight line. If, however, (δ, q) differ from these special values, the energy spectrum changes dramatically: it adopts many local energy minima and maxima, in good agreement with the analytical calculations.

The contour plot of the energy $E(\delta, q)$ for a chain of N=10 dipoles can be seen in figure 4.2(b). Several cross sections of this two-dimensional energy surface for different K are shown in Fig. 1(a). Amazingly, the minima occur for all $q, \delta = \pm(n\pi/N), \pi \pm (m\pi/N)$ for $K < -2.3D$ and with integer $q, \delta = \pm(n\pi/N), \pi \pm (\pi/2N) + \pm(m\pi/N)$ for $K > 2.3D$ with integer $m \in [0, N]$ and $n \in [0, N]$. That is to say, the energy spectrum becomes discrete and the energy gaps become

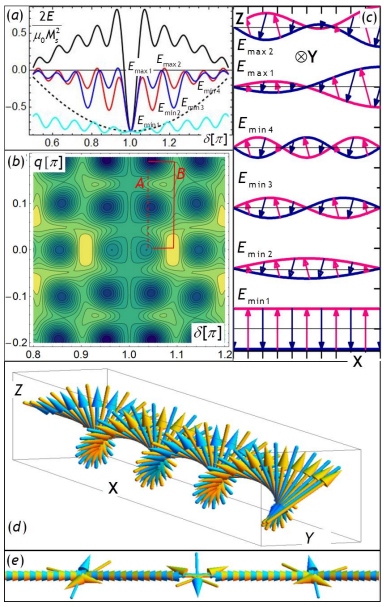

Figure 4.2: (a),(b) One- and two-dimensional representation of the energy of modulated helices in a dipolar chain consisting of 10 moments as a function of δ and q. (c) S_z for several energy levels. The thick lines in (c) show the envelope lines of double helices corresponding to the magnetic moments (arrows) in two sublattices. The dashed parabola in (a) corresponds to the energy E of the harmonic spiral $S(x)$ =(sin(δx),0, cos(δx)); the black, red, and blue curves correspond to $E(\delta)$ of modulated helices with K = 0 and q = 0, q = π/N, and q = $2\pi/N$, respectively, while the cyan line shows $E(\delta)$ for q = π/N and $K = 2.5D$. The energy scale in (b) goes linearly from $-0.8D$ (blue) to +$0.8D$ (yellow). (d) Three-dimensional representation of an intermediate helix state found in the SD simulations for N = 81 (video SI2 of [53]) for $K = -1.23\mu_0 M_z^2$ at $T < 1K$. (e) End configuration of SD simulations for K = 0 and starting configuration identical to (d).

size dependent; i.e., we observe all components of quantum confinement. The deepest lying energy minima, i.e., stablest energetic states, correspond to magnetic helices (MH) with integer number of turns along the chain, as demonstrated in Fig. 4.2(c), (d) and (e), and can be uniquely described using quantum numbers m and n defining wave vectors δ and q, which are commensurate to the chain length. The number of helix turns is codified by the smaller wave vector. For example, if $\vec{\delta} \leq \pi$, then $q = \pi/N$ amounts to to one helix turn of the total chain.

4.4 Spin dynamics and Monte Carlo simulations

In order to access the complete configurational space beyond the restrained two-wave-vector approximation, Monte Carlo (MC) and spin dynamical simulations (SD) have been performed. Furthermore, a magnetomechanical model presented in fig. 4.3 and described in the supplementary

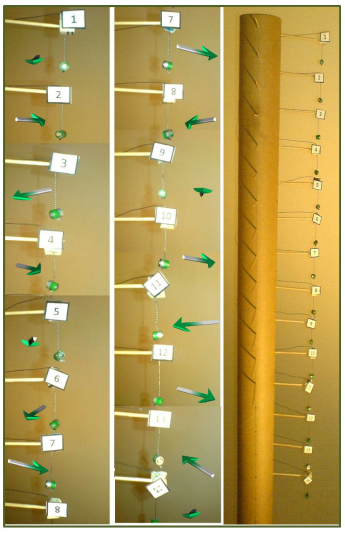

Figure 4.3: Magnetomechanical model of [53]. The magnets are not connected by a wire. They are hanging each on their own soft, nonmagnetic filament and they are coupled via magnetostatics only. The hole is larger than the diameter of the filament and magnets may rotate without screwing it. Left: Stable spin helix with modulation vector $q = (3/2)\pi/14$. Right: General view of the model. Silver and green colors represent the north and the south poles, respectively.

material of [53] has been tinkered. While the MC procedure has been developed to adequately model the equilibrium properties of many-body systems, the SD calculate an exact dynamical path from an initial configuration into a final configuration. The details of the numerical procedures are elaborated on in [50, 51, 53]. According to the MC analysis, the stable equilibrium configuration of a dipolar chain of length N for $k_BT > 0.1D$ and $-1.2D < K < 2D$ indeed corresponds to $E_{min,2}$ in Fig. 4.2(c), i.e., to $(q, \delta) = (\pi/N, \pi \pm (\pi/N))$. Only at lower temperatures or higher anisotropy the ground AFM state can be achieved. Our SD simulations demonstrate that the exact dynamical path towards the global energy minimum strongly depends on the starting configuration and passes through several energy MH states as predicted above. Starting with the $S\sin[(\pi + (\pi/N))x], \cos[(\pi + (\pi/N))x], 0$ state, e.g., one ends up with a half-turn helix for an anisotropy comparable with the dipolar energy. Another example of dynamical relaxation is recorded in video SI2 in the supplemental material of [53], while one of the intermediate configurations is shown in fig. 1(d). Even for a vanishing anisotropy constant K the system often freezes in a modulated structure, as depicted in fig. 4.2(e). In accordance with the simulations, the most probable stable states of the chain established after mechanical agitation are spin spirals with π or $\pi = 2$ twist. Both an easy-plane rotation of magnetization and a systematic modulation of the easy-axis component were clearly observable. The less likely (but still stable) spiral case with $q = 3\pi/2N$

configuration is visible in fig. 4.3.

The stability of the magnetic helices can be explained as such: (i) the internal fields, created in these structures, coincide with the orientation of dipoles, and (ii) those states cannot be transformed into the magnetic ground state by a continuous transformation of the configuration; i.e., they possess topological stability. Consequently, if the ends of a chain are fixed, the helical structure will remain at the local energy minimum. Next, this property will be exploited to achieve different (δ, q) states artificially. To manage this, the magnetization vector of one of the terminal dipoles is rotated in order to introduce additional magnetic energy into the chain. The results of this procedure are carried out in MC simulations (Fig. 3), SD simulations (see suppl. of [53]), as well as in the magnetomechanical models (see suppl. of [53]).

The Monte Carlo simulations have been prepared for chains of length $N = 70a$. The equilibrium winding-up process is given in fig. 4.4(a). At the beginning, the slow annealing procedure from the aforementioned literature has been applied. At the end of this process, at a thermal energy of $k_BT = 0.05D$, the chain has relaxed into the magnetic helix state with $q = \pi/N$; that is, the entire chain acquired half of a modulation period. This relaxed configuration was taken as the starting point for the winding-up process. Then, the first spin has been rotated at an angular rate of $(\pi/2)/(2 \times 10^5$ Monte Carlo Steps (MCS)), as our analysis revealed that a critical period of about 2×10^5 MCS was long enough to achieve a new equilibrium state. After nine completed rotations, as illustrated in fig. 4.4(a), the chain was found at the stable $q = 5\pi/2N$ helix configuration. The other terminal spin of the chain remained unconstrained.

In Fig. 3(b) the calculated time dependence of magnetization of the z component for the first and the last spins is visualized. It is visible that the rotation angle of the last spin is retarded compared to the rotation angle of the first spin. This can be explained by the tendency of the magnetic spiral to remain in its initial energy minimum.

A further interesting aspect concerns the propagation velocity of a knot in the magnetic helix: The propagation of this knot decreases with increasing q, as shown by the dashed red line, and can be modeled by a function of the form $v = at^2$ with some negative acceleration a. The backward process is shown in figs. 4.4(c) and 4.4(d). Here, the first spin is rigid and the relaxation of the chain is observed. The back rotation was decelerated once again, as evidenced in fig. 4.4(d). The whole process, however, was slowed down significantly. This can be explained by the fact that

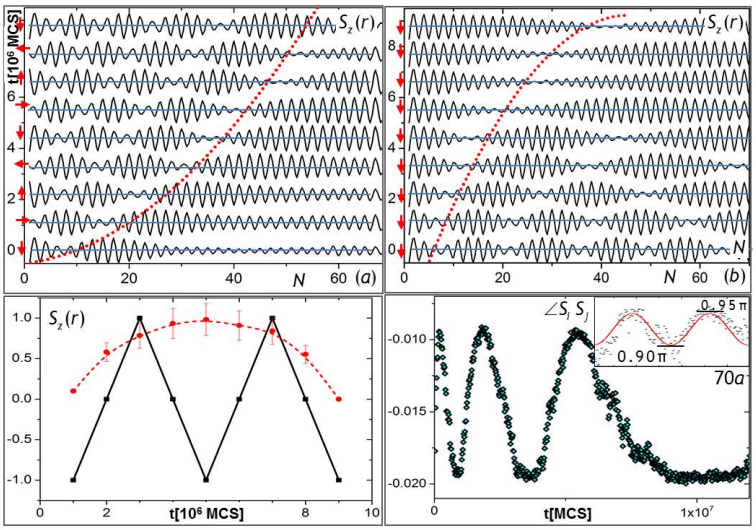

Figure 4.4: MC simulations of a linear chain of 70 dipoles with $K = -1.23\mu_0 M_S^2$ at $k_B T < 1K$. (a) Winding up of the spiral. Each snapshot of $S_z(r)$ corresponds to a relaxed state. The far-left moment (red) has been rotated with velocity of $(\pi/2) \times 105$ MCS. (b) Time dependence of the far-left (blackline) and the far-right (red line) moments. (c) Release of the stored energy: the left moment is fixed downwards. (d) Nonlinear time dependence of the chain-averaged $\langle S_z \rangle$. A typical angle distribution in a relaxed helix is shown in the inset.

spiral had been released at a local energy minimum state.

The obtained MC results match up very well to the SD simulations shown in supplementary videos of [53] for dipolar coupling and for ferromagnetic exchange interaction, respectively. The relevant time scale for dynamical processes depends on the chosen magnitude of the magnetic interactions and damping parameters of the atomistic LLG Equations. For a chain made out of $35 \times 35 \times 2$ nm sized nanoparticles, interparticle distance 20 nm, and a dimensionless Gilbert damping parameter of 0.01, the completed winding up process (see supplementary video sequence of [53]) amounts to milliseconds. In addition, SD provides new interesting features of the winding process. The first important conclusion is that the speed of the entire process depends on the angular rotation speed, enforced externally onto the first spin of the chain. The second, more staggering finding is that the emergence of each new turn of the magnetic helix is accompanied by a sudden change in the magnetization of many dipoles in the case of dipolar interaction. At the beginning, the neighbors of the first dipole rotate coherently with certain phase shift between adjacent spins of the chain. The internal energy of the chain grows as a result towards a local energy maximum (e.g., $E_{max,1}$ in fig. 4.2). Once the rotation angle approaches a critical value, the local maximum is realized, and a very fast change in the orientation of magnetization of the dipoles happens and

the system relaxes down into the nearest stable state corresponding to two turns of the helix (see suppl. of [53]). During this time, a subset of the dipoles continue to rotate in the direction of forced winding up, while another subset rotate in the opposite direction. In the proposed magneto-mechanical experiment, the states with larger q's are also found immediately after the magnetization jumps described above, as demonstrated in [53]. Accordingly, the magnetic helix can find stable energy states automatically, once they are critically rotated. This happens to be different from Dzyaloshinskii-Moriya spin spirals [30].

The "click into place" behavior during the winding-up process exists also for $q = 0$, i.e., for S_x = 0. If the same procedure is repeated for a spin chain coupled via nearest-neighbor ferromagnetic exchange interaction with identical interaction strength and damping parameters, the behavior is analogous but no jumps occur (see suppl. of [53]), as the relaxation time of the chain and the angular rotation velocity are of the same order of magnitude. When a wound-up chain (in a high-energy state) is released (supplementary to [53]), the stored energy is sufficiently large to overcome several barriers.

The intriguing features of magnetic helices open up several interesting perspectives for technological applications. Arguably the most important opportunity lies in the new way of energy storage. Among the oldest methods, which is still actively employed in a large number of applications, is the spring wind-up technique.

A simple but powerful everyday example, would be a clockwork device mechanically powered by a mainspring. In this scheme, one end of a mechanical spring is fixed, while the other one gets continuously rotated until the spring is wound up. Then this latter spring terminal is released and the stored potential energy transforms into the kinetic energy of a clock arrow, a motor, a pump, or another viable mechanical device. An analogous procedure can be applied to the magnetic helices. By rotation of one chain's end via local magnetic fields or spin-polarized currents, one can force the helix towards higher integer windings and, thus, magnetic higher energy. The system can then stay in this new stable configuration to store the energy introduced through the rotational process of the first spin. The stored energy can then be transformed into its mechanical or magnetic counterparts to produce work as visualized in the supplementary parts of [53] and fig. 4.3.

As an additional feature of stability of the above described magnetic helices, one can understand their stability from the viewpoint of continuum theory of micromagnetics [62] as a non-trivial topological magnetic configuration.

4.5 Search for topological invariants

In the previous chapter the metastability of magnetic helices has been explored on the basis of energy considerations. On the other hand, it has been mentioned that only certain numbers of windings are stable. The subset of integer windings of the helical structure can be characterized by a winding number.

As mentioned in the previous subsection, the investigated magnetic chains are based on the atomistic model of classical magnetic spin moments μ. This implies that the theory of topological order, which is a continuous theory for both, the considered degrees of freedom and its underlying spatial background, doesn't apply here. However, in the continuum limit of infinitesimal inter-particle distance $d \to 0$ and slowly varying magnetic order parameter $\delta M \to 0$ for $\delta d \to 0$, one can employ ideas from topology to explain the stability of the described magnetic helices, if the rotation of the spin vector takes place in one plane only.

The phenomenon of topological stability itself is simple and fundamental. Objects with so called "topological order" are resistant against any local perturbation. The notion of topological stability can be applied to various physical systems that can be modeled by continuous vector fields. Magnetic materials are among these systems. Particularly, magnetic solitons and skyrmions, introduced first in [56], belong to the class of topologically non-trivial objects, studied extensively in the last decade.

While magnetic skyrmions are characterized by the topological winding number

$$n_2 = \frac{1}{4\pi M_s} \int_A \vec{M}(\frac{\partial M}{\partial x} \times \frac{\partial M}{\partial y}) dxdy \tag{4.20}$$

the magnetic helices, modulated in a plane, can be seen as one -dimensional counterparts with the winding number

$$n_1 = \frac{1}{2\pi} \int_0^{2\pi} 1 d\phi \tag{4.21}$$

with angle ϕ as introduced in Eq. (4.2) of section (4.2).

In this interpretation, the metastable configurations of AFM or dipolar magnetic helices correspond to the topological numbers n_1 going from $[1/2, \ldots, N/2]$. Equations 4.20 and 4.21 can be

derived as special cases of a generalized Stokes theorem [133].

4.5.1 Summary

In conclusion, I showed in this chapter that finite length microscopic magnetic chains possess a quantized spectrum of local energy minima, sensitive to the geometry of the chain, the material of the elements and the shape of the involved particles. Furthermore, these quantized states can be described by topological winding numbers. The unique energy spectrum is realized by magnetic spirals or magnetic helices and in the case of spirals the configurations carry additional topological protection as one-dimensional counterparts to the celebrated two-dimensional magnetic skyrmions [28, 29, 30]. The results explain recent experimental findings and open broad perspectives for possible future investigations concerning the dynamics of this nontrivial system. Also, the results stimulate research in pursuit of realizing such topologically protected spin chains experimentally by exchange-coupled thin films [31, 40].

Chapter 5

Efficient propagation of a dissipative wavefunction equation (DWE)

Energy dissipation or damping is relevant for any real dynamical process of an open system, such as those described in the two previous chapters 3 and 4 on arrays of nanodots and spin chains. Therefore it is important to be able to develop a microscopic understanding of the underlying quantum dynamics of such systems which will be describable by quantum master equations. In the decoherent limit, a classical master equation such as that described in 2.4.2 can be available. This may also give a good correspondence with time-quantified Monte-Carlo systems, as demonstrated for spin-based Langevin equations [52] and even a conventional Monte-Carlo-simulation approach can yield good agreement with dynamically treated systems, as demonstrated in the previous chapter 4.

If the Hamiltonian, describing the system, its environment and their interaction is known microscopically, integration over environmental degrees of freedom yields a master equation for a reduced density matrix, influenced by a superoperator which is linear, completely positive and trace-preserving. If the dynamical description boils down to the simplicity of a rate equation, but knowledge about the microscopic details of transition rates is inaccessible, it is meaningful to use an absorbing potential, described by a special non-Hermitian operator in the energy eigenbasis acting on a wave function. Such an operator keeps the advantage of representing unitary and non-unitary processes and allows for an estimation of the corresponding dynamical time scales. On the other hand, this kind of generator enforces very small time steps in a numerical treatment for the large damping regime, as it usually contains an unrestricted parameter for the anti-Hermitian

absorption part. Furthermore, the used time-evolution includes a nonlinear term due to a necessary normalization condition for the wave function which is numerically expensive. Here, we propose an extended effective non-Hermitian Hamiltonian which can simulate the effects of a physically meaningful "viscous force" on the reduced system and avoids the need for a perpetual rescaling of time. Additionally, we have implemented a numerically advantageous linear version of the resulting evolution equation. This procedure can save significant computation time, particularly for interacting systems with an exponentially increasing Hilbert space. We show that the proposed equation can be easily implemented for a numerical description of different systems and exemplify this for different spin relaxation scenarios.

5.1 Introduction

When a system is driven out of equilibrium, it will return back to its statistical mechanical or mechanical equilibrium state after a finite time. The reason is that practically any system coupled to the environment exchanges energy with the latter [69, 70, 71, 72] and looses phase coherence [73, 74] to it (or more precisely to the total system). Various techniques have been employed to describe or model these processes [75, 76, 77, 78, 79, 80, 81]. A complete account of quantum mechanical interactions in the above sense can be given by a reduced density matrix description [123] or by a stochastic wave function description [83, 84]. A complete deterministic wave function evolution has to be linear to be in accordance with the theory of relativity [85]. If, however, only energy dissipation is at the center of concern and one has to deal with incomplete information about microscopic degrees of freedom, one can phenomenologically model this situation as a non-unitary process and the description typically includes a nonlinear damping term in addition to a linear equation of motion. Mathematically, such a nonlinearity reflects the absence of superposition among the one-dimensional Hilbert space vectors, associated with the diagonal elements of a (decohered) density matrix. A meaningful normalization condition in each time step helps to successfully estimate transfer rates from the reduced amount of obtainable information and approximates the irreversible relaxation behavior of many quantum systems, particularly decay phenomena for systems of different complexity. Two simple examples of classical nonlinear equations are given by the Newton equation with friction for mechanical systems or the Landau-Lifshitz-Gilbert equation of motion for magnetic systems [86, 87] which have many important applications in fields far apart from clas-

sical mechanics [89, 90]. One of the possible ways to treat the dissipative processes of quantum dynamics is the extension of the linear Schrödinger equation to its nonlinear counterpart [91] and using the classical limit $\hbar \to 0$ for the derivation of the Landau-Lifshitz-equation [92].

For the purpose of describing energy losses without exact knowledge of a master equation, a Hermitian total Hamiltonian H_{tot}, employed in the Schrödinger equation $H_{tot}|\psi\rangle_{tot} = E|\psi\rangle_{tot}$ of a closed system is often replaced by a non-Hermitian Hamiltonian, $H_{eff}|\psi\rangle_{eff} = E^{'}|\psi\rangle_{eff}$ which allows, besides its exploration in the foundations of quantum physics [93], for a phenomenological description of particle and quasiparticle decay [94, 27] as well as energy gain and loss of open systems with respect to an environment [96]. In a self-consistent approach towards measurements of a single open quantum system, the wave function evolution of environmentally-influenced quantum systems is stochastic and confined to a non-Hermitian evolution or quantum jumps, depending on particular random number outcomes [85, 97, 98, 99, 100]. This leads to Lindblad master equations [79] after sufficient averaging over independently generated stochastic Monte-Carlo wave function trajectories. However, we do not use non-Hermitian operators in this latter context to model "avoided jumps" in quantum jump trajectories.

The damping parameter λ describes the magnitude of energy dissipation from a subsystem. It is usually treated as a free, (a priori) unrestricted parameter or is taken from experimental measurements such as ferromagnetic resonance spectroscopy [101] or inelastic phonon scattering [102] measurements. Depending on the strength of λ, one distinguishes between the overdamped (return to equilibrium without oscillations), underdamped (return to equilibrium with oscillations) and critical regimes. An effective non-Hermitian Hamiltonian has the typical form $H^{*}_{eff} = H_0 - i\Gamma$ with H_0 being conveniently chosen as the Hamiltonian of the open system, $i\Gamma := i\lambda H_0$ the absorbing potential, being related to the imaginary part of the self-energy operator in standard perturbative calculations [103]. While the underdamped case is well described by an evolution equation, generated from the above mentioned Hamiltonian, specific assumptions have to be made, if one is interested in critical or overdamped regimes (see for example [104]). This is rooted in the straightforward linear parametrization of the anti-Hermitian operator part in λ which must have some limits, as discussed later in the manuscript.

In section 5.2, we briefly describe the meaning of non-Hermitian generators in the phenomenological dynamics of the non-unitary time evolution of open quantum systems. We advocate the

viewpoint that anti-Hermitian parts of the non-Hermitian operator should be bounded due to physical constraints and thus relaxation rates should be limited by an upper bound for all physical situations. Based on this, one can define a fixed scale for the time resolution of numerical integration schemes for the differential equations of motion.

We propose a simple non-Hermitian operator of the above kind and use it to generate a linear time evolution of the wave function with a numerically performed normalization. This saves computation time, as opposed to the proposals of the authors [85, 91, 92] who have used nonlinear evolution equations.

We present simulation results in section 5.3 which match predictions for single spin degrees of freedoms in external fields. Additionally, we show the nontrivial case of exchange interacting spins. Motivated by the simulations, we compare our finding to results obtainable by the classical Landau-Lifshitz-Gilbert equation [27], bearing a striking conceptual similarity to our effective equation of motion.

We finalize the chapter with a short discussion of the results in section 5.5.

5.2 Linear evolution equation for a non-Hermitian Hamiltonian

Open quantum systems that are perturbatively coupled to an environment yield a non-unitary time evolution in general which is conveniently worked out in the interaction picture. In many cases, after the integration over the known environmental degrees of freedom, one can identify a superoperator which serves as the generator for such a time evolution of the density operator. The Lindbladian [79] and Redfieldian [106] are typical superoperators at the Born-Markov level of perturbation theory with(out) secular approximation and usually capture both Hermitian and anti-Hermitian contributions. The anti-Hermitian contributions signal a non-vanishing result for the Fourier transform of the environmental Green's function and assist in explaining transitions within a stabilized basis of the reduced density matrix of the open system, but still permits a linear, trace-preserving and completely positive superoperator. A computationally less demanding description at the level of the Schrödinger equation without detailed knowledge about the transition rates cannot capture the process of coherence matrix elements of a density matrix, but can be justified for the purpose of

a qualitative description of energy renormalization and/or dissipation. It can thus qualitatively approximate the relaxation process, described by rate equations in a stabilized basis, and is given by the simple equation of the kind

$$i\hbar\frac{d}{dt}|\Psi\rangle = H_{eff}|\Psi\rangle. \tag{5.1}$$

The operator $\mathcal{H}_{eff} = \mathcal{H}_1 + i\mathcal{H}_2$ has a Hermitian and an anti-Hermitian part ($\mathcal{H}_1 = \mathcal{H}_1^+$ and $\mathcal{H}_2 = \mathcal{H}_2^+$) which separates a (renormalized) unitary part of the evolution and a non-unitary, dissipative part (sometimes associated with a decay rate or an absorbing potential). The presence of $\mathcal{H}_2$ destroys the unitary group property of the set of time evolution operators $\{U(t_i)\,,\, \forall i \geq i_0\}$ and the limited knowledge, obtainable from the thought of system-environment-interaction, necessitates a normalization procedure for the wave function. The latter is usually expanded into a set of orthonormal states $\{|\psi\rangle_n\}$ of an isolated quantum system (often the energy eigenbasis), subjected to irreversible repopulation of its eigenstates.

For our purposes of describing several damping regimes for a quantum system, it is convenient to group the anti-Hermitian parts of operators of equality (5.1) into two classes of *bounded* and *not bounded* anti-Hermitian generators. In our terminology, bounded anti-Hermitian generators $\mathcal{H}_2 : X \to Y$ fit the usual definition of bounded operators,

$$\frac{||\mathcal{H}_2|\Psi\rangle||_Y}{|||\Psi\rangle||_X} \leq M, \quad M < \infty \tag{5.2}$$

known from functional analysis [107], while for not bounded operators $M \to \infty$ in (5.2).

Since the strength of dissipation or decay rates is associated to the magnitude of the bound of the anti-Hermitian operator

$$\frac{||\mathcal{H}_2|\Psi\rangle||_Y}{|||\Psi\rangle||_X} \leq M, \tag{5.3}$$

and $[\mathcal{H}_1, \mathcal{H}_2]_- = 0$ (and often even $\mathcal{H}_1 = C\mathcal{H}_2$ with $C \in \mathcal{R}$), we require a bound which is of order $\mathcal{O}(M) \leq 1$ to achieve time scales for the non-unitary part of the evolution which are larger or equal to typical time scales of unitary processes.

In many applications [91, 92, 99], operators of the kind

$$\mathcal{H}^*_{eff} = H_0 - i\Gamma := H_0 - i\lambda H_0 \tag{5.4}$$

are used and λ is usually not a restricted damping parameter (in general λ could be chosen matrix-valued). Therefore, one has to deal with a not bounded anti-Hermitian generator for $\lambda \to \infty$, even though the spectrum of H_0 may be bounded from above.

Such operators lead to a nonlinear evolution equation of the kind

$$i\hbar\frac{d}{dt}|\psi\rangle = \Big(H_0 - i\lambda[H_0 - \langle H_0\rangle]\Big)|\psi\rangle, \tag{5.5}$$

if the renormalization of the probability amplitude is worked into an infinitesimal time evolution of the corresponding initial wave function [92]. We refer to (5.5) as *Gisin's Equation* due to a proposal of Gisin in [91].

Beyond the fact, that such an equation requires an adjustment of time steps in the large damping regime $\delta t \to \delta t = \delta t(\lambda)$, its nonlinear part, which entails the expectation value of the Hamiltonian H_0, slows down the speed of numerical integration, particularly for multistep methods, such as higher-order Runge-Kutta integration methods.

The simplest phenomenological way to avoid the adjustment of time steps is the introduction of the Gilbert-like prefactor $\frac{1}{1+\lambda^2}$ to the right hand side of equality (5.5) [105].

However, despite this modification, the approach still contains a nonlinearity due to the $\langle H_0\rangle$-expression. This is computationally ineffective due to the arising matrix-vector-products, repeatedly appearing in multistep numerical integration methods, used by many authors.

In order to overcome both the time scaling problem and the nonlinear representation for the evolution equation, we propose a new non-Hermitian generator

$$\mathcal{H}_{eff} = H_0 \sum_{n=0}^{\infty}(-i\lambda)^n = \frac{H_0 - i\lambda H_0}{1+\lambda^2}\,. \tag{5.6}$$

This ansatz pays tribute to the fact that limitations of the relaxation rates arise from changes to the microscopic transition rates in master equations, reflected by the superoperator or in our simplified case by an absorbing potential. Instead of converting the information, provided by this operator, into a nonlinear evolution equation, we numerically normalize our initial wave function

and thus succeed in implementing a formally linear evolution equation of the form

$$i\hbar\frac{\partial}{\partial t}|\psi\rangle = \Big(\frac{H_0 - i\lambda H_0}{1+\lambda^2}\Big)|\psi\rangle. \tag{5.7}$$

Since we constructed the effective Hamiltonian for a not yet specified H_0 Hamiltonian, we can simulate relaxation not just for single particle systems but also many-body systems by this method, as long as we can diagonalize the Hamiltonian H_0.

5.3 Simulations

In order to make the numerical scheme more efficient, as described in the last section, we describe the following results directly in terms of Eq. (5.1). The Eq. (5.5) in its rescaled form of [105] should therefore be replaced and propagated by a linear representation

$$i\hbar\frac{\partial}{\partial t}|\psi\rangle = \Big(\frac{H_0 - i\lambda H_0}{1+\lambda^2}\Big)|\psi\rangle \tag{5.8}$$

which captures the slow down of the relaxation rate at the level of the generator alongside L^2-normalization $|\psi(t+\delta t)\rangle \to \frac{|\psi(t+dt)\rangle}{|||\psi(t+\delta t)\rangle||}$ after each successful numerical time step $t \to t+\delta t$.

The Eq. (5.7) and the rescaled version of Eq. (5.5) differ by an infinitesimal time step δt only, but (5.7) can be solved much easier numerically, as one doesn't incorporate information about the eigenstate repopulation into the dynamical equation explicitly but only at the end of the time step and avoids the evaluation of the $\langle H_0\rangle$ term within the linear multistep method (Runge-Kutta 4.th order), implemented in our code.Numerical renormalization of (5.7) is also sligthly superior to (2.36) in the numerical integration efficiency, since latter requires to deal with the second summand of the dissipator $\mathcal{D}$ four times in the integration while it only appears once for the former. This saves memory time and becomes particularly relevant for a large Hilbert space dimension N of the relevant quantum system. Such a simplification is not possible for systems, based on a non-Hermitian Hamiltonian of the form (5.4), as there is no natural bound on the magnitude of the anti-Hermitian part of the generator and thus one would need smaller time steps in the numerical treatment to approximate both unitary and non-unitary timescales $\mathcal{O}(\tau)_1$ and $\mathcal{O}(\tau)_2$ of the dynamics simultaneously, as one expects $\mathcal{O}(\tau)_1 >> \mathcal{O}(\tau)_2$ in the large damping limit $\lambda >> 1$.

In order to verify the new results from the previous section, we performed numerical simulations of the Schrödinger equations (5.5) and (5.7) for the simple example of a spin 1 quantum system. We started our investigation with the simplest possible Hamiltonian

$$H_0 = -S_z B_z \tag{5.9}$$

and plotted the relaxation behavior of the x-component of the expectation value of the spin operator, respectively. Therefore our eigenbasis $|\psi\rangle_S = \sum_n c_n |\psi_n\rangle$ is just the ordinary Zeeman basis of a single quantum spin. Figure (5.1) shows the result in the three different damping regimes.

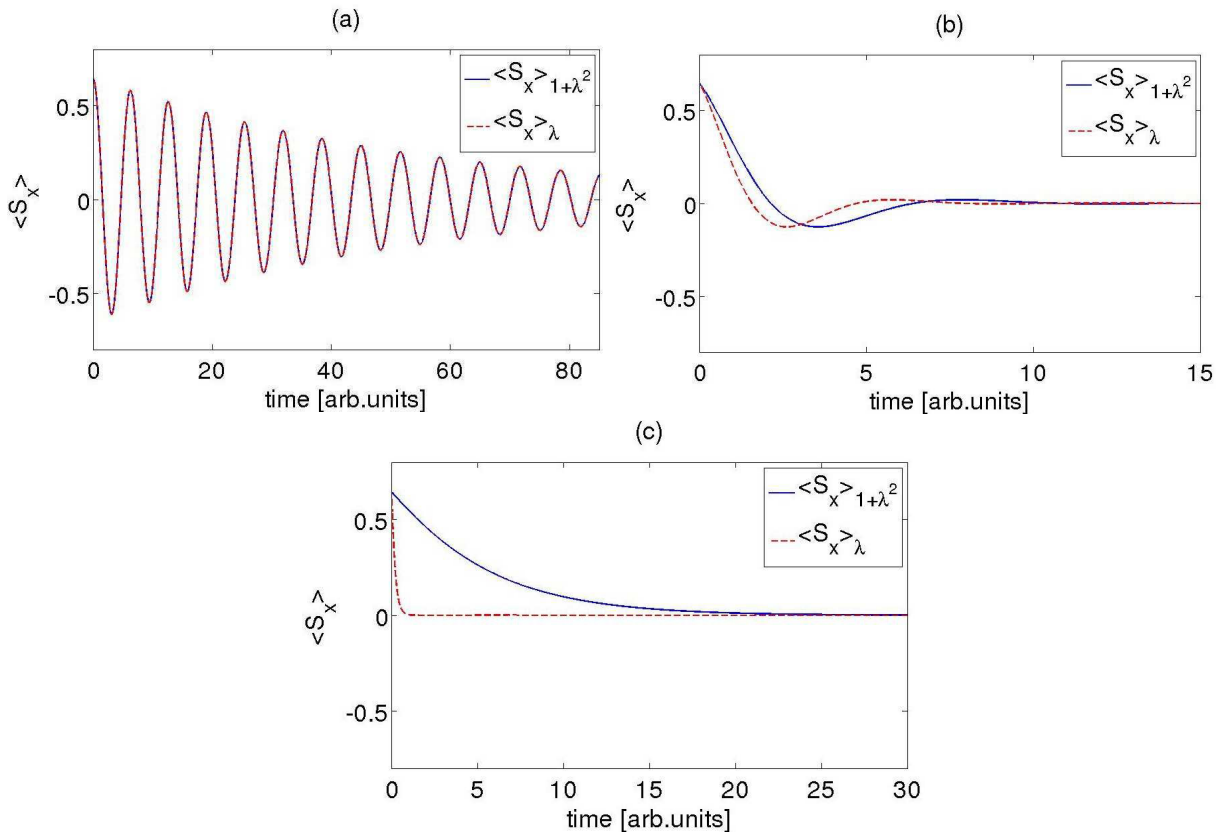

Figure 5.1: Relaxation behavior of the $\langle S_x \rangle$-component described by the two equations (5.7) (blue) and (5.5) (red) for a normalized initial expectation value $\langle \vec{S} \rangle$=(0.885,0.442,0.147): (a) Underdamped evolution ($\lambda = 0.02$), (b) near critically damped evolution (λ=0.6) and (c) overdamped evolution (λ=5.0). The magnetic field has been set to unity $B_z := 1$ in all cases. The differences in the relaxation behavior for the two equations are clearly visible for large damping values.

For small damping far below unity the results of (5.5) and (5.7) nearly coincide, as expected. One can understand this in a very simple way by performing a Taylor expansion of the denominator of (5.7) which yields

$$\lim_{\lambda \to 0} \frac{1}{1+\lambda^2} \approx 1 + \mathcal{O}(\lambda^3). \tag{5.10}$$

For intermediate damping the solutions clearly deviate from one another and one sees the increasing period of the oscillation of the expectation value for the improved, linear Eq. (5.7). The period T_1 described by the already known nonlinear evolution equation increases compared to the low damping value. The increase in period T_2 of Eq. (5.7) is larger, but from the comparison of the curves one can still not infer a qualitative but only a quantitative difference concerning the physical predictions, given by Eqs. (5.5) and (5.7). This general increase of the period of equality (5.7) is clearly due to the known frequency renormalization and, as expected, the ratio of periods $\frac{T_1}{T_2}$ is exactly 1/2 for $\lambda = 1$.

In the strong damping regime for $\lambda = 5$, one can finally distinguish the predictions of the equations also in a qualitative way: While the relaxation rate of the Eq. (5.7) has decreased several times compared to critical damping, the Eq. (5.5) has still increased ever since reaching that critical value. For our proposed equation, we clearly see a carry-over effect from the subcritical to supercritical damping like in the solution for the damped one-dimensional harmonic oscillator, known from the literature [86]. Damping of the real time oscillation period for subcritical damping is followed by damping of the imaginary time period for supercritical damping. Such a physically "well-behaved" solution space is imposed by the expansion of the Hamiltonian $\mathcal{H}_{eff}$ in imaginary damping values which has a limitless radius of convergence after Borel regularization [109].

However, our method is not restricted to a single spin relaxation but we can simulate ground state relaxation behavior of many-body systems and obtain the different damping regimes for them. We exemplify this for a realistic Hamiltonian

$$H_0 = -J\hat{\vec{S}}_1\hat{\vec{S}}_2 - K\sum_{i=1}^{2}\hat{S}_{z,i}^2 - \sum_{i=1}^{2}\vec{B}\hat{\vec{S}}_i \tag{5.11}$$

of two coupled magnetic atoms, prepared near the $|\uparrow,\uparrow\rangle$-product state and compare the relaxation results with thermal expectation values of the diagonalized Hamiltonian H_0 of Eq. (5.7) in figures (5.2) and (5.3). We found an excellent agreement in the low temperature regime $T \approx 0$ for the antiferromagnetic $J < 0$ case, discussed in figure (5.2).

We particularly demonstrated this convergence property in figure (2)(d) by lowering the tem-

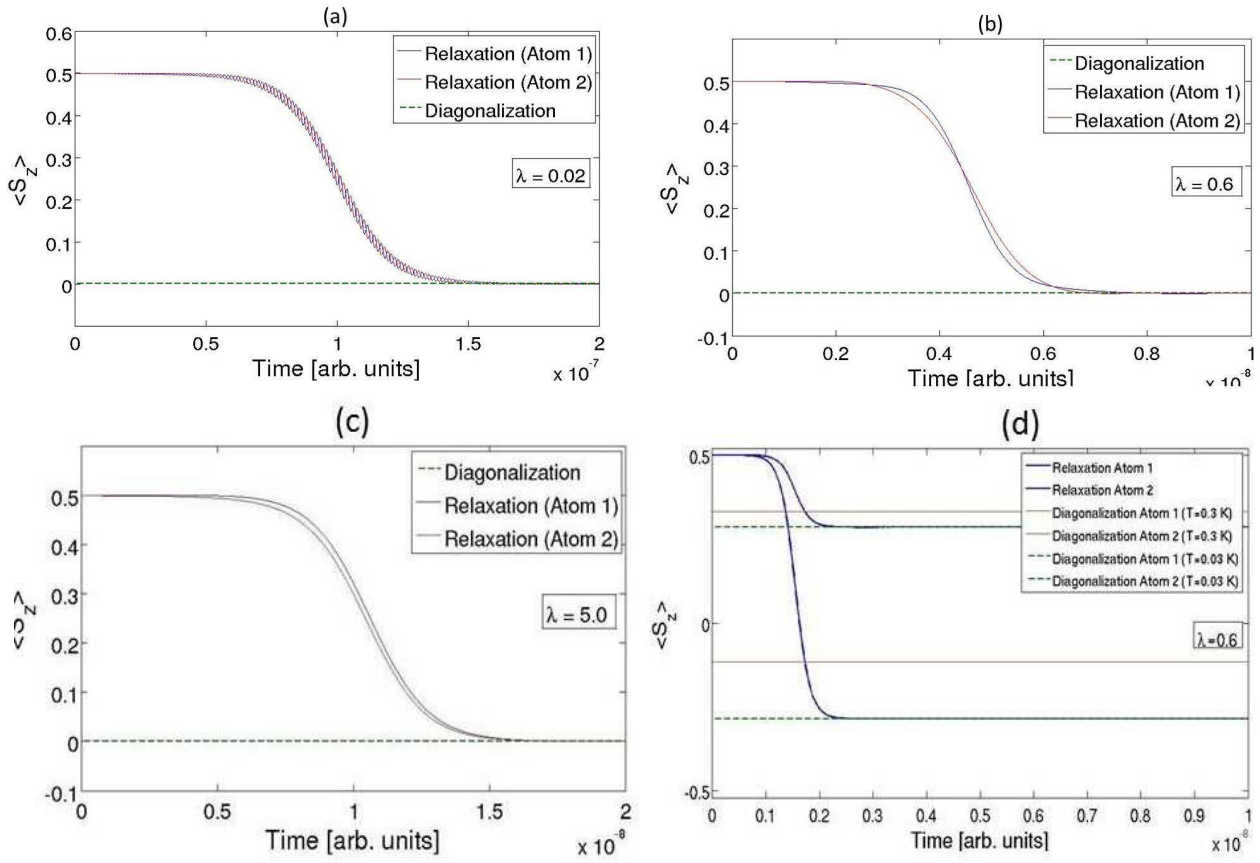

Figure 5.2: Relaxation behavior of two antiferromagnetically coupled spins of S=1/2 with $J = -0.01$ and uniaxial anisotropy $K = 1.0$, prepared near the ferromagnetic state $|\uparrow,\uparrow\rangle$ for damping parameters (a)$\lambda = 0.02$, (b)$\lambda = 0.6$ and (c) $\lambda = 5.0$. One observes relaxation towards the thermal expectation value of the traced out spin degrees of freedom of the total spin Hamiltonian at T=0.3 K. The speed of relaxation is in qualitative agreement compared to the relaxation of a single spin in a magnetic field. (d) Relaxation behavior of two antiferromagnetically coupled S=1/2 spins with $J = -1.0$, uniaxial anisotropy $K = 1.0$, and $B_z = 0.7$, prepared near the ferromagnetic state $|\uparrow,\uparrow\rangle$ for a damping parameter $\lambda = 0.6$. One observes a relative deviation of the dynamically computed expectation values for the traced out spins at T=0.3 K. If we reduce the temperature to T=0.03 K for the thermal expectation values, we find excellent agreement with the relaxation dynamics of our effective equation of motion (5.7).

perature for the thermal expectation value. That observation justifies the neglection of the noise operator in our effective equation of motion and demonstrates that our equation of motion is sensitive to the spectral energies of many-particle eigenstates. This even holds, if we prepare the state of the system in a subspace of the many-particle Hamiltonian, as discussed in the representative figures.

However, the ferromagnetic $J > 0$ case, described in figure (5.3)(a)-(c), deserved special mentioning, as its symmetry does not allow to find thermal expectation values from a single preparation of the initial state of the wave function alone, as we prepare the system in a subspace of the Hilbert space $\mathcal{H}$ of the Hermitian Hamiltonian of H_0 for the sake of generality.

However, an average over different initial conditions could easily account for the thermal expectation value and one may also achieve a thermal expectation value through the introduction of small additional tunneling contributions via transverse components to the Zeeman energy. Such quantum tunneling can thus serve a qualitatively similar purpose in our set up, as Gaussian noise fluctuations does in a (classical) Langevin treatment by making a larger part of the relevant mathematical space (Hilbert space or phase space) accessible to the system.

We want to conclude this paragraph by mentioning that Eq. (5.7) can be rewritten as

$$\begin{aligned} i\hbar(1+i\lambda)\frac{\partial}{\partial t}|\psi\rangle &= H_0|\psi\rangle \\ i\hbar\frac{\partial}{\partial t}|\psi\rangle &= (H_0 + \lambda\hbar\frac{\partial}{\partial t})|\psi\rangle. \end{aligned} \tag{5.12}$$

which is, however, structurally equivalent to

$$\frac{\partial}{\partial t}\vec{S} = -\frac{\gamma}{\mu_s}\vec{S}\times(\vec{H}_{eff} - \lambda\frac{\mu_s}{\gamma}\frac{\partial}{\partial t}\vec{S}) \tag{5.13}$$

if one replaces $|\psi\rangle$ by a classical, normalized, dimensionless spin variable $\vec{S}$, by using $\vec{H}_{eff} = -\frac{\partial H_0}{\partial \vec{S}}$ with effective magnetic moment μ_s and gyromagnetic ratio γ. One quickly realizes that the cross-product operation corresponds to real and imaginary phase rotations of a wave function in this analogy (see r.h.s. of (5.12)). Hence, our ansatz is valid for a variety of physical systems, bearing a close conceptual analogy to classical spin systems or more general geometric vectors, as Eq. (5.13)

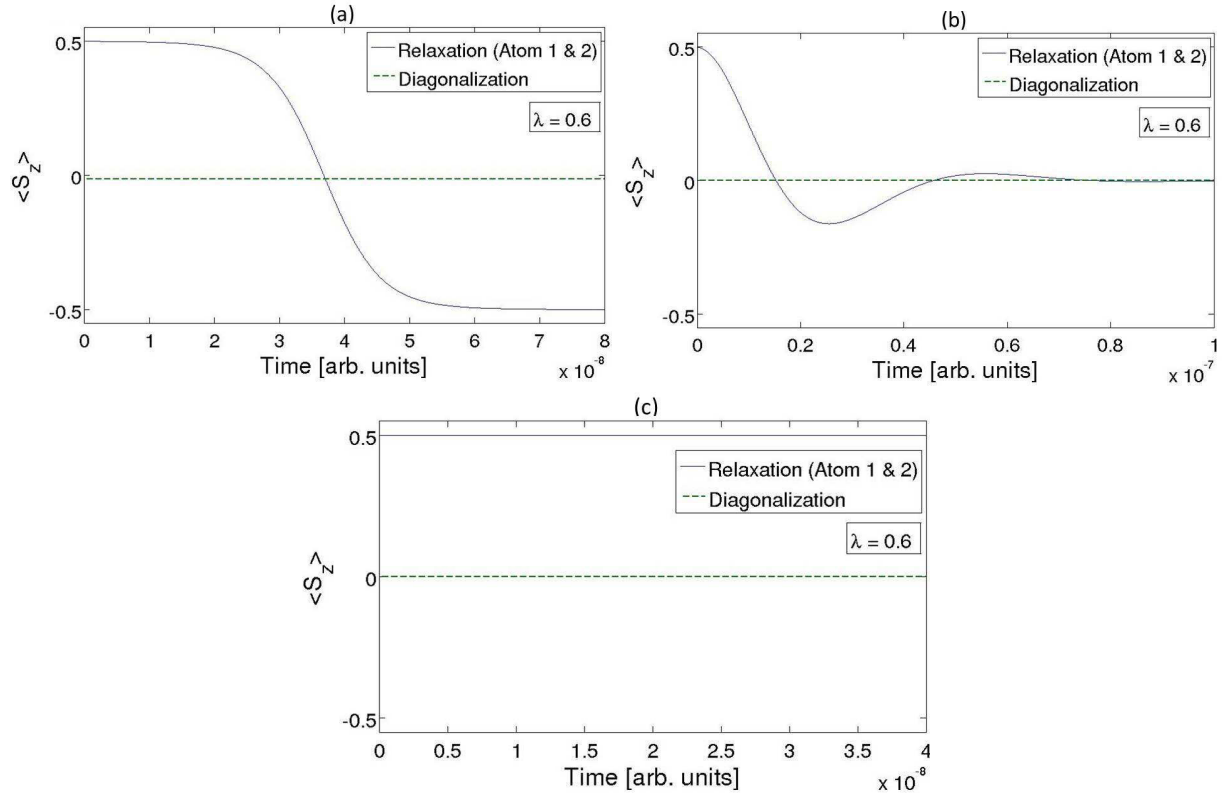

Figure 5.3: Relaxation behavior of two ferromagnetically coupled spins of S=1/2 with $J = 0.01$ and uniaxial anisotropy $K = 1.0$, prepared near the ferromagnetic state $|\uparrow,\uparrow\rangle$ for damping parameters $\lambda = 0.6$: (a) An additional B_z-field (small compared to exchange and anisotropy energies) gives rise to a reversal of the spin, as the $|\downarrow,\downarrow\rangle$ becomes the ground state of the spectrum. Large deviations from the thermal expectation value occur as significant thermal contributions from excited states are not accounted for by the relaxation. (b) An additional B_x-field leads to both relaxation and residual tunneling. For this case, thermal expectation values (at T=0.3 K) can be matched, as additional tunneling of the magnetization makes a large part of the Hilbert space of the system accessible for the damping part to act on. (c) In the absence of additional magnetic fields, thermal expectation values (at T=0.3 K) cannot be reproduced due to the symmetry of the Heisenberg model, but by considering a preparation in the opposite direction and averaging over the preparations of the wave function, one can restore the "thermal character" of the final state.

is nothing but the famous Landau-Lifshitz-Gilbert-Equation in its implicit representation.

5.4 Relation between DWE, Gisin's Equation and Lindblad-master equation

The r.h.s. of the Lindblad master Equation, introduced in 2.36, does have a Hermitian part through the (renormalized) Hamiltonian unitary part and an anti-Hermitian part through the dissipator $\mathcal{D}(a_i, a_j^+)$. Furthermore the second term of the dissipator was meant as a normalization term for the trace of the density on which the Lindbladian acts. This can be deduced from the application of the Choi-Kraus-theorem [144, 143] in the construction of a general generator for a quantum dynamical semi-group in [79].

We can now relate the Hamiltonian part of the Lindbladian to the first (Hermitian) summand of 5.4 and the first part of $\mathcal{D}$ to the second part (anti-Hermitian summand of 5.4), if we take a particular choice of U(1)-gauge for the wavefunction $|\Psi\rangle$ in the complex unit plane $\mathcal{C}$ and use the Born rule $|\Psi\rangle|^2 = \rho$ for the conversion of pure states into diagonal elements of a density matrix by scalar multiplication of bra- and ket-vectors. The second summand of $\mathcal{D}$ which ensures the trace class conservation during evolution can be related to either the nonlinear part 5.5 or the numerical normalization procedure at the end of the numerical integration step which we introduced in 5.6.

This comparison reveals that not only equations 2.36 and 5.7 act linearly on pure states and yield the same transformation independent of the chosen basis of states, but also the equation 5.5 does act linearly on the pure states, if the same interpretation of the action of the Hamiltonian is applied, as assumed for 2.36 and 5.4. This is in accordance with the axioms of quantum mechanics, referenced earlier in [82].

The nonlinear action results for the convex combination

$$|\Psi\rangle\langle\Psi| = \sum_i p_i |\psi_i\rangle\langle\psi| \tag{5.14}$$

of gauge-fixed pure states $|\psi\rangle$.

The fact that normalization is a position-dependent process in all three schemes L_i (i=1..3),

however, doesn't allow for a linear decomposition of a mixed state into two mixed states in the same basis $|\Psi\rangle\langle\Psi|$:

$$L_i \sum_{j=1}^{2} |\Psi_j\rangle\langle\Psi_j| \neq P_1 L_i |\Psi_1\rangle\langle\Psi_1| + P_2 L_i |\Psi_2\rangle\langle\Psi_2| \tag{5.15}$$

This is caused by the fact that a locally convex vector space is defined by a family of semi-norms $\mathcal{N}_{t\in\mathcal{R}}$ instead of just by one unique norm $\mathcal{N}$ [107].

In the following, we compare our proposed DWE (5.7), Gisin's Equation (5.5) and the Lindblad-Equation in the form (2.36) with respect to a conventional numerical implementation for numerical integration of the forth order Runge-Kutta scheme (a.k.a. "RK4"), as discussed in (2.4.3) of the chapter 2.4). The use of such a higher order method is useful to avoid the accumulation of numerical errors in the integration scheme due to numerical inaccuracy of *number*-variables of the programming language C++ (such as "float" or "double") [154].

In order to be able to compare the three Eqs. (5.7), (5.5) and (2.36), we have to assume a fixed basis for the density matrix representation of (2.36) which is equivalent to having pointer basis in the semi-classical decoherence limit of the quantum master equation. This enables to discuss the Lindblad equation as a semi-classical rate equation with evaluation of N eigenstates in a pointer basis of a Hilbert space $\mathcal{H}$ of dimension $dim(\mathcal{H}) = N$.

We remember the necessary four steps for numerical integration of the function f in the ordinary differential equation

$$y^k = f(t, y(t), y'(t), \ldots, y^(k-1)(t)) \tag{5.16}$$

$$y^1 = y_i, i = 0, \ldots, k-1. \tag{5.17}$$

They read

$$k_1 = hf(t_n, y_n) \tag{5.18}$$

$$k_2 = hf(t_n + \frac{h}{2}, y_n + \frac{k_1}{2}) \tag{5.19}$$

$$k_3 = hf(t_n + \frac{h}{2}, y_n + \frac{k_2}{2}) \tag{5.20}$$

$$k_4 = hf(t_n + h, y_n + k_3) \tag{5.21}$$

$$y_{n+1} = y_n + \frac{k_1}{6} + \frac{k_2}{3} + \frac{k_2}{3} + \frac{k_4}{6} + \mathcal{O}(h^5) \tag{5.22}$$

and one can easily see that with k being restricted to "1", f translates into the r.h.s. expressions of (5.7), (5.5) and (2.36).

The nonlinear Eq. (5.5) contains an expectation value

$$\langle H_0 \rangle \tag{5.23}$$

which implies an additional evaluation cost of a co-vector-matrix-vector product $\langle \psi | H_0 | \psi \rangle$ of dimension N for four evaluation points $k_1..k_4$ compared to the Eq. (2.36) and (5.7).

Despite the above described numerical gain of Eq. (2.36) over Eq. (5.5), the former equation still contains the second summand of the dissipator $\mathcal{D}$

$$\sum_{i,j}^{N^2-1} H_{i,j}([a_i \rho a_j^+] - \frac{1}{2}[a_j^+ \mathbf{1} a_j, \rho_{sys.}]) \tag{5.24}$$

from the section (2.3) of the theory chapter in its diagonal form.
This amounts to a matrix product of the coefficient matrix $H_{i,j}$ and the unit matrix ∞ and the diagonal density matrix which enters the four evaluation steps $k_1..k_4$ of the RK4 scheme. Since both the diagonal matrix and density matrix only contain N non-zero value, one is troubled with an additional matrix-vector-vector-product.

Finally, in our proposed DWE (5.7) we are neither troubled with additional co-vector-matrix-vector products nor with additional matrix-vector-vector-products for our generator of the time evolution of the form (5.6). The numerical normalization only enters *after* the completed numerical integration in order to arrive at normalized expectation values. Henceforth, f only contains

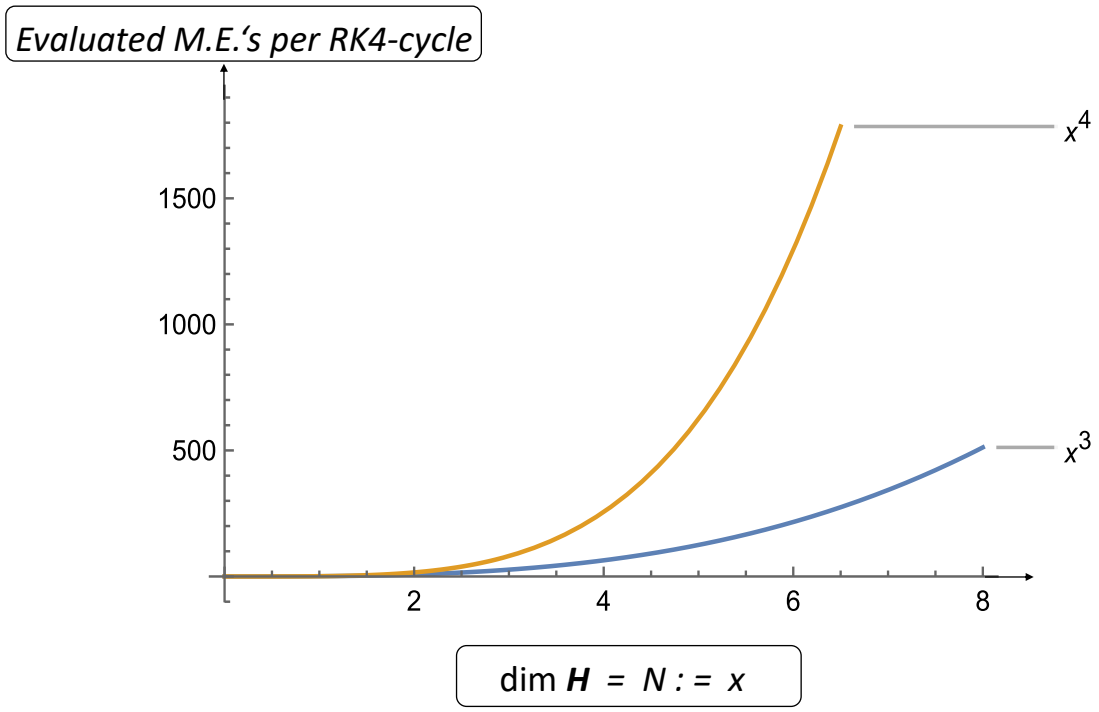

Figure 5.4: Estimated number of evaluated matrix elements (M.E.) for each RK4-cycle as a function of the Hilbert space dimensionality *dim* $\mathcal{H}$ of the quantum spin system for Gisin's Equation and the Lindblad-master equation (orange) and for the DWE (5.7) (blue), respectively.

matrix-vector-products for the four numerical evaluation steps. In the following section (5.3), these expectation values will be taken for spin operators.

The quantitative performance gain per "RK4-cycle" depends on the produced computational costs of the additional co-vector-matrix-vector-product of (5.5) and the matrix-vector-vector-product of (2.36) over the ordinary matrix-vector-products, present in all three equations. In general this leads to an evaluation cost of $\mathcal{N}^3$ for matrix-vector-products and $\mathcal{N}^4$ for matrix-vector-vector-product or co-vector-matrix-vector-product respectively, as shown schematically in figure 5.4. This results in an overall performance gain which scales linearly with the Hilbert space dimension $dim\mathcal{H} = N$.

5.5 Conclusion

To summarize, in this chapter a non-Hermitian Hamiltonian H_{eff} is proposed to describe dissipative behavior of quantum systems in all known damping regimes (underdamped, critically damped

and overdamped) with a bounded anti-Hermitian part. The H_{eff} generator has to be introduced into an effective time evolution scheme and the consequent action on the prepared wave function leads a superficially linear Schrödinger equation (5.7) which has to be numerically normalized at each time step. This approach saves significant computation time by avoiding numerical integration of an expectation value within the Schrödinger time evolution which costs co-vector-matrix-vector-products multiple times during the evaluation of a multistep method of choice (such as RK4). This is not the case in previous approaches [91, 105] and sets clear limits for numerical evaluation of larger system sizes in the respective cases, as the numerical performance gain through our implementation method scales linearly with the Hilbert space dimensionality of the open quantum system of interest. The chosen form of H_{eff} simultaneously permits to avoid any asymptotic divergences for limiting values of the damping parameter and reflects the microscopic origins of such restrictions to the relaxation process, covered by the restricted information provided by the anti-Hermitian absorbing potential. These findings question the idea to provisionally rescale the time in nonlinear evolution equations with unrestricted parameters and favor a linear evolution viewpoint with a modified Hamiltonian instead, though not ruling out dynamical explanations for restricted relaxation rates, either. The method was tested numerically for the case of isolated and exchange coupled atomic spins and can be extended to more complicated systems, as long as the Hermitian Hamiltonian H_0 of the method can be diagonalized. For the sake of completeness, it should be mentioned that the results obtained in this chapter can be straightforwardly generalized to a finite temperature bath by introducing canonical, numerical weight factors onto the pure states of the dissipative Schrödinger Equation, analogously to the procedure of the Lindblad equation (see [68] for example).

Chapter 6

Summary

In the following, I will summarize the main results that were obtained in the course of this Ph.D. thesis.

In chapter 3, the influence of interactions on the dynamics of classical magnetic bits was investigated, as well as the connection of this mutual influence of particles as a generalized manifestation of dynamical phases, known from responses of magnetic domains to external driving fields.

It was shown that dipolar interactions can play a profound role in the dynamic reversal process of magnetic dots even in the case when the anisotropy energy describes the leading energy contribution. From the observed switching behavior it could be inferred that correlations determine the switching events of the dots. Dynamical processes have been observed that are in contradiction to a single particle scenario and can lead to erroneous interpretations when only single particles are taken into account for measurements. The spin-dynamical simulations and the calculation of the dynamical correlation function proved that dynamic correlations open up new reversal paths through the multidimensional energy landscape. The most important outcome was the demonstration that dynamical correlations are reaching longer than expected by the static cubic inverse interaction law due to long range dipolar fields. It was revealed that correlations come into play when a magnetic system is brought close to the state of thermal instability. Furthermore, it was shown that the choice of anisotropy strength influences the switching frequency of other particle, too and that there are superficial similarities between the magnetic coupling of switching particles and that of harmonic oscillators, coupled by a spring. Furthermore, the mutual influence of simple exchange fields was investigated and different regimes for the inter-particle correlations were de-

fined, being reminiscent of a classical dynamical phase transition. The results demonstrate that the interactions cannot be disregarded when thermally assisted switching is the focus of interest, which has wide ranging implications for the fundamentals of superparamagnetism as well as technical applications, such as heat or thermally assisted magnetic recording [156].

In chapter 4, a more stable and robust combination of parameters was selected for the interaction among classical spins in a chain to yield several metastable magnetic states upon manipulation of a terminal spin. At a conceptual level the uncontrollable thermal field influence was replaced by an exactly controllable spin-field interaction energy. The accumulated magnetic work through rotation even lead to topologically stable configurations in one dimension.

We showed that finite magnetic chains, coupled by exchange, RKKY, or dipolar interactions and manipulated at their boundary by controlled external fields, admit a quantized energy spectrum of non-collinear spin states. The spectrum properties were found to be influenced by multiple parameters, such as chain geometry, material of the elements, as well as the shape anisotropy of the particles. The quantized energy spectrum simultaneously corresponded to one-dimensional topologically protected configurations in the form of magnetic helices with integer winding numbers. The results opens up several new perspectives for future investigations of quantization effects, observed in classical energy spectra. Furthermore, the generation of nontrivial spiral states due to boundary manipulation may be compared to the spiral states that have been created via the inclusion of DM interaction in the past: It may raise the question, if boundary spin rotation and the associated accumulation of magnetic energy in the form of work emulates the parametric enhancement of the DM coupling constant for magnetic surfaces with inversion symmetry breaking.

In chapter 5, an equation for the evolution of pure quantum states was proposed on theoretical foundations that effectively describes the decoherence regime of a semi-classical master equation of Lindblad-type for coupled quantum spins.

The proposed equation retained some quantum features, as eigenstates of a coupled system of quantum spins were subjected to the decoherence dynamics of the system. Furthermore, it was argued based on simple reasoning for numerical integration schemes of higher order, such as the famous RK4 scheme, that the linear implementation of the equation of motion yields a performance advantage over previous linear and nonlinear implementations, as the normalization procedure for

the mixed state (convex combination of the propagated pure states) was performed neither analytically nor within the numerical integration scheme, but was performed *after* the integration procedure as an operation for the evaluation of the expectation value. Despite the unfavorable nonlinear expression of an analog equation, originally published by Gisin [91] we'd like to conclude with the remark that a nonlinear evolution when applied only to the convex combination of pure states is not in contradiction with fundamental laws of physics such as special relativity [85], the second law of thermodynamics [126] or the stochastic interpretation of the density operator put forward by John von Neumann and re-emphasized by Diósi [155]. It also doesn't lead to exotic predictions for quantum computations, as predicted by Llyod and Abrahams [127].

In summary, the proposed equation can describe both quantum and classical features for coupled magnetic spin degrees of freedom, as it relies on a diagonalization of the energy eigenbasis and manifested decoherence of the off-diagonal elements of an associated density matrix state. This makes it a potentially interesting object of study for the evolution one- and two-dimensional magnetic systems, such as those presented in chapter 3 and chapter 4, used for classical computations by interpolating between quantum and classical spin dynamics.

Bibliography

[1] A. Neumann, D. Altwein et al.: *Influence of long-range interactions on the switching behavior of particles in an array of ferromagnetic nanostructures*, New J. Phys. **16**, 083012 (2014)

[2] M. Plumer, J. van Ek and D. Weller: *The Physics of Ultra-High-Density Magnetic Recording*, Springer, Berlin (2001)

[3] O. Hellwig, J. K. Bosworth, E. Dobisz, D. Kercher, T. Hauet, G. Zeltzer, J.D. Risner-Jamtgaard, D. Yaney and R. Ruiz: *Bit patterned media based on block copolymer directed assembly with narrow magnetic switching field distribution*, Appl. Phys. Lett. **96**, 052511 (2010)

[4] T. Albrecht et al.: *Bit patterned media at 1 Tdot in*$^{-2}$ *and beyond*, IEEE Trans. Magn. **49** (2), 773-778 (2013)

[5] A. Kikitsu, T. Maeda, H. Hieda, R. Yamamoto, N. Kihara and Y. Kamata: *5 Tdots in*^{2} *bit patterned media fabricated by a directed self-assembly mask*, IEEE Trans. Magn. **49** (2) 693-698 (2013)

[6] B. Pfau, C. M. Günther, E. Guehrs, T. Hauet, H. Yang, L. Vinh, X. Xu, D. Yaney, R. Rick, S. Eisebitt and O. Hellwig: *Origin of magnetic switching field distribution in bit patterned media based on pre-patterned substrates*, Appl. Phys. Lett. **99** (6), 062502 (2011)

[7] C. Brombacher, M. Grobis, J. Lee, J. Fidler, T. Eriksson, T. Werner, O. Hellwig and M. Albrecht: *L1*$_0$ *FePtCu bit patterned media*, Nanotechnology **23** (2), 025301 (2012)

[8] O. Hellwig, A. Berger, T. Thomson, E. Dobisz, Z. Z. Bandic, H. Yang, D. S. Kercher and E. E. Fullerton: *Separating dipolar broadening from the intrinsic switching field distribution in perpendicular patterned media*, Appl. Phys. Lett. **90** (16), 162516 (2007)

[9] T. Hauet, E. Dobisz, S. Florez, J. Park, B. Lengsfield, B. D. Terris and O. Hellwig: *Role of reversal incoherency in reducing switching field and switching field distribution of exchange coupled composite bit patterned media*, Appl. Phys. Lett. **95** (26), 262504 (2009)

[10] C. Ross: *Patterned magnetic recording media*, Annu. Rev. Mater. Res. **31**, 203-235 (2001)

[11] B. Terris: *Fabrication challenges for patterned recording media*, J. Magn. Magn. Mater. **321** (6), 512-517 (2009)

[12] B. Terris: *Patterned media for future magnetic data storage*, Microsyst. Technol. **13**, 189-196 (2007)

[13] M. Wellhöfer, M. Weissenborn, R. Anton, S. Pütter and H.P. Oepen: *Morphology and magnetic properties of ECR ion beam sputtered Co/Pt films*, J. Magn. Magn. Mater. **292**, 345-358 (2005)

[14] H. Stillrich, C. Menk, R. Fromter and H.P. Oepen: *Magnetic anisotropy and spin reorientation in Co/Pt multilayers: Influence of preparation*, J. Magn. Magn. Mater. **322** (9-12), 1353-1356 (2010)

[15] A. Neumann, C. Thönnißen, A. Frauen, S. Heße, A. Meyer and H.P. Oepen: *Probing the magnetic behavior of single nanodots*, Nano Lett. **13**, 2199-2203 (2013)

[16] S. Krause, G. Herzog, T. Stapelfeldt, L. Berbil-Bautista, M. Bode, E.Y. Vedmedenko and R. Wiesendanger: *Magnetization Reversal of Nanoscale Islands: How Size and Shape Affect the Arrhenius Prefactor*, Phys. Rev. Lett. **103**, 127202 (2009)

[17] M. Alexandrou, P. W. Nutter, M. Delalande, J. de Vries, E. W. Hill, F. Schedin, L. Abelmann and T. Thomson : *Spatial sensitivity mapping of Hall crosses using patterned magnetic nanostructures*, J. Appl. Phys. **108** (4), 043920 (2010)

[18] Y. Cornelissens and F. Peeters: *Response function of a Hall magnetosensor in the diffusive regime*, J. Appl. Phys. **92** (4), 2006 (2002)

[19] B. Webb and S. Schultz: *Detection of the magnetization reversal of individual interacting single-domain particles within Co-Cr columnar thin-films*, IEEE Trans. Magn. **24** (6), 3006-3008 (1988)

[20] W. Wernsdorfer, E. B. Orozco, K. Hasselbach, A. Benoit, B. Barbara, N. Demoncy, A. Loiseau, H. Pascard and D. Mailly: *Experimental Evidence of the Néel-Brown Model of Magnetization Reversal*, Phys. Rev. Lett. **78**, 1791-1794 (1997)

[21] A. Kobs, *Magnetogalvanic effects in ferromagnets of reduced dimensions*, PhD Thesis, Universität Hamburg (2013)

[22] M. B. Stearns: *3d, 4d and 5d elements, alloys and compounds*, Landolt-Börnstein-Group III: Condensed Matter, Numerical Data and Functional Relationships in Science and Technology (**19a**) (Berlin: Springer), 24-141 (1986)

[23] C. Hurd: *The Hall Effect in Metals and Alloys*, (New York: Plenum) doi:10.1007/978-1-4757-0465-5 (1972)

[24] P. Langevin: Magnétisme et théorie des électrons, Annales de Chimie Physique **5**, 70-127 (1905)

[25] F. Schwabl: *Statistische Mechanik*, Springer-Verlag (3. Edition), Berlin and others, 2006

[26] E.B. Davies: *Markovian Master Equations*, Commun. math. Phys. **39**, 91110 (1974)

[27] L. Landau, E. Lifshitz: *On the theory of the dispersion of magnetic permeability in ferromagnetic bodies*, Phys. Zeitschrift d. Sowjetunion **8**, 153 (1935)

[28] A. A. Khajetoorians, J. Wiebe, B. Chilian, and R. Wiesendanger: *Realizing all-spin-based logic operations atom by atom*, Science **332** (6033), 1062-1064 (2011).

[29] L. Zhou, J. Wiebe, S. Lounis, E. Vedmedenko, F. Meier, S. Blügel, P. H. Dederichs, and R. Wiesendanger: *Strength and directionality of surface RudermanKittelKasuyaYosida interaction mapped on the atomic scale*, Nat. Phys. **6**, 187-191 (2010).

[30] M. Menzel, Y. Mokrousov, R. Wieser, J. E. Bickel, E. Vedmedenko, S. Blügel, S. Heinze, K. von Bergmann, A. Kubetzka, and R. Wiesendanger: *Information Transfer by Vector Spin Chirality in Finite Magnetic Chains*, Phys. Rev. Lett. **108**, 197204 (2012).

[31] B. Behin-Aein, D. Datta, S. Salahuddin, and S. Datta: *Proposal for an all-spin logic device with built-in memory*, Nat. Nanotechnol. **5** (4), 266-270 (2010).

[32] E. Mengotti, L. J. Heyderman, A. F. Rodríguez, F. Nolting, R. V. Hügli, and H.-B. Braun: *Real-space observation of emergent magnetic monopoles and associated Dirac strings in artificial kagome spin ice*, Nat. Phys. **7**, 68-74 (2011)

[33] L. Onsager: *Crystal Statistics. I. A Two-Dimensional Model with an Order-Disorder Transition*, Phys. Rev., **65**, 117 (1944).

[34] C. Yang: *The Spontaneous Magnetization of a Two-Dimensional Ising Model*, Phys. Rev. **85**, 808 (1952).

[35] L. P. Kadanoff: *Scaling laws for ising models near* T_c, Physics (Long Island City, N.Y.) **2**, 263 (1966).

[36] J. P. Morgan, A. Stein, S. Langridge, and C. H. Marrows: *Thermal ground-state ordering and elementary excitations in artificial magnetic square ice*, Nat. Phys. **7**, 75-7 (2011).

[37] A. Schumann, P. Szary, E. Y. Vedmedenko, and H. Zabel: *Magnetic dipole configurations in honeycomb lattices: order and disorder*, New J. Phys. **14**, 035015 (2012).

[38] M. Ewerlin, D. Demirbas, F. Brüssing, O. Petracic, A. A. Ünal, S. Valencia, F. Kronast, and H. Zabel: *Magnetic Dipole and Higher Pole Interaction on a Square Lattice*, Phys. Rev. Lett. **110**, 177209 (2013).

[39] A. Fernandez-Pacheco, D. Petit, R. Mansell, R. Lavrijsen, J. H. Lee, and R. P. Cowburn: *Controllable nucleation and propagation of topological magnetic solitons in CoFeB/Ru ferrimagnetic superlattices*, Phys. Rev. B **86**, 104422 (2012).

[40] M. van Kampen et al.: *On the realization of artificial XY spin chains*, J. Phys. Condens. Matter **17** (2), L27 (2005).

[41] H. Heuser: *Lehrbuch der Analysis, Teil 1.*, Teubner (12.Edition), Stuttgart/Leipzig, 1998.

[42] N. Mikuszeit, L. Baraban, E.Y. Vedmedenko, A. Erbe, P. Leiderer, and R. Wiesendanger: *Quasiantiferromagnetic 120° Néel state in two-dimensional clusters of dipole-quadrupole-interacting particles on a hexagonal lattice*, Phys. Rev. B **80**, 014402 (2009).

[43] K. Bernot, L. Bogani, A. Caneschi, D. Gatteschi, and R. Sessoli: *A Family of Rare-Earth-Based Single Chain Magnets: Playing with Anisotropy*, J. Am. Chem. Soc. **128** (24), 7947-7956 (2006).

[44] W. Wernsdorfer: *Molecular Magnets: A long-lasting phase*, Nat. Mater. **6** (3), 174-176 (2007).

[45] A. A. Khajetoorians, J. Wiebe, B. Chilian, S. Lounis, S. Blügel, and R. Wiesendanger: *Atom-by-atom engineering and magnetometry of tailored nanomagnets*, Nat. Phys. **8** (6), 497-503 (2012).

[46] R. Skomski et al.: *Nanomagnetic skyrmions*, J. Appl. Phys. **111**, 07E116 (2012).

[47] S. Bedanta, E. Kentzinger, O. Petracic, W. Kleemann, U. Rücker, Th. Brückel, A. Paul, S. Cardoso, and P. P. Freitas: *Modulated magnetization depth profile in dipolarly coupled magnetic multilayers*, Phys. Rev. B **74**, 054426 (2006).

[48] B. Braunecker, P. Simon, and D. Loss: *Nuclear magnetism and electron order in interacting one-dimensional conductors*, Phys. Rev. B **80**, 165119 (2009).

[49] J. Klinovaja, P. Stano, A. Yazdani, and D. Loss: *Topological Superconductivity and Majorana Fermions in RKKY Systems*, Phys. Rev. Lett. **111**, 186805 (2013).

[50] E. Y. Vedmedenko and N. Mikuszeit: *Multipolar Ordering in Electro- and Magnetostatic Coupled Nanosystems*, ChemPhysChem **9** (9), 1222-1240 (2008).

[51] U. Nowak: *Thermally activated reversal in magnetic nanostructures*, Annu. Rev. Comput. Phys. IX, 105-151 (2001).

[52] U. Nowak, R. W. Chantrell, E. C. Kennedy: *Monte carlo simulation with time step quantification in terms of langevin dynamics*, Phys. Rev. Lett. **84** (1):163-166 (2000)

[53] E. Y. Vedmedenko and D. Altwein: *Topologically Protected Magnetic Helix for All-Spin-Based Applications*, Phys. Rev. Lett. **112**, 017206 (2014)

[54] R. Wiesendanger: *Spin mapping at the nanoscale and atomic scale*, Rev. of Mod. Phys. **81** (4), 1495-1550 (2009)

[55] E. Zaarur, Y. Peleg, R. Pnini: *Quantum mechanics*, Schaum's Easy Oulines Crash Course, McGraw Hill (USA), (2006)

[56] A.N. Bogdanov; D.A. Yablonskii: *Thermodynamically stable "vortices" in magnetically ordered crystals. The mixed state of magnets*, Sov. Phys. JETP. **68**: 101103 (1989)

[57] N. Nagaosa, Y. Tokura: *Topological properties and dynamics of magnetic skyrmions*, Nat. Nanotechnology. **8** (12), 899911 (2013)

[58] N. Romming; et al.: *Writing and deleting single magnetic skyrmions*, Science **341**: 636639. (2013)

[59] L. V. Dzemiantsova, G. Meier and R. Röhlsberger: *Stabilization of magnetic helix in exchange-coupled thin films*, Sci. Rep. **5**, 16153 (2015)

[60] *History of Hydropower*, Department of Energy. energy.gov. (Office of Energy Efficiency Renewable Energy), **url**: https://www.energy.gov/eere/water/history-hydropower, Retrieved on May 4, 2017.

[61] H. Schneider (May 8, 2013): *World Bank turns to hydropower to square development with climate change*. The Washington Post, Retrieved on May 9, 2013.

[62] W.F. Brown, Jr.: *Micromagnetics*, New York: Wiley (1963)

[63] A.P. Popov; M.G. Pini: *Magnetic helices as metastable states of finite XY ferromagnetic chains: An analytical study*, Journ. of Magn. and Magn Mat. **451**, (319-326) (2018)

[64] A. Neumann, N. Franz, G. Hoffmann, A. Meyer and H.P. Oepen: *Fabrication of Magnetic Co/Pt Nanodots Utilizing Filled Diblock Copolymers*, Surf. Sc. Journ., **4**, (Suppl 1: M5) 55-64 (2012)

[65] G. E. Moore: *Cramming more components onto integrated circuits.*, Electronics **38** (8), 114-117 (1965)

[66] MLA style: *The Nobel Prize in Physics 2007*. NobelPrize.org. Nobel Prize Outreach AB 2018. Wed. 28 Mar 2018, **url**: https://www.nobelprize.org/prizes/physics/2007/summary/

[67] A. Fert: *Nobel Lecture: Origin, development, and future of spintronics*, Rev. Mod. Phys. **80**, 1517 (2008)

[68] G. Schaller: *Non-Equiblibrium Master Equations*, Lecture Notes, Technische Universität Berlin (2014)

[69] S.Loth et al.: *Measurement of fast electron spin relaxation times with atomic resolution*, Science **329** (5999), 1628-1630 (2010)

[70] E. Vedmedenko: *Competing interactions and pattern for-mation in the Nanoworld* (Wiley, Weinheim, 2007)

[71] D. E. F. Biesinger et al.: *Intrinsic Metastabilities in the Charge Configuration of a Double Quantum Dot* , Phys. Rev. Lett. **115**, 106804 (2015).

[72] F. Bloch: *Nuclear Induction*, Phys. Rev. **70**, 460 (1946)

[73] H. D. Zeh: *On the Interpretation of Measurement in Quantum Theory*, Found. of Phys. **1**, 6976 (1970)

[74] W. H. Zurek: *Decoherence and the transition from quantum to classical – REVISITED*, Phys. Today **44**, 36 (1991)

[75] R. P. Feynman and F. L. Vernon: *The theory of a general quantum system interacting with a linear dissipative system*, Ann. Phys. (N. Y.) **24**, 118-173 (1963)

[76] O. Caldeira and A. Leggett: *Influence of Dissipation on Quantum Tunneling in Macroscopic Systems*, Phys. Rev. Lett. **46**, 211 (1981).

[77] S. Nakajima: *On Quantum Theory of Transport Phenomena —Steady Diffusion—*, Prog. of Theor. Phys. **20**, 948 (1958).

[78] R. Zwanzig: *Ensemble Method in the Theory of Irreversibility*, Journ. of Chem. Phys. **33** (5), 1338 (1960).

[79] G. Lindblad: *On the generators of quantum dynamical semigroups*, Commun. Math. Phys. **48**, 119-130 (1976)

[80] P. Ullersma: *An exactly solvable model for Brownian motion: IV. Susceptibility and Nyquist's theorem*, Physica **32** (1), 90-96 (1966)

[81] P. Riseborough et al.: *Exact results for a damped quantum-mechanical harmonic oscillator*, Phys. Rev A **31** (1), 471-478 (1985).

[82] J. von Neumann: *Wahrscheinlichkeitstheoretischer Aufbau der Quantenmechanik*, Gött. Nachr. **1**, 245-272 (1927).

[83] V. Belavkin: *A continuous counting observation and posterior quantum dynamics*, J. Phys. A Math. **22**, 1109-1114 (1989).

[84] V. Belavkin: *A Quantum Particle Undergoing Continuous Observation*, Phys. Lett. A **140**, 359-362 (1989).

[85] N. Gisin: *Stochastic quantum dynamics and relativity*, Helv. Phys. Acta **62**, 363-371 (1989).

[86] H. Goldstein: *Class. Mech.*, Pearson (3. Edition), London (2013)

[87] Am. Inst. Electr. Engrs., p.253 (10/1955)

[88] T. L. Gilbert: *IEEE Trans. Magn. **40**, 3443 (2004)*, IEEE Trans. Magn. **40**, 3443-3449 (2004).

[89] D. J. Wineland and H. Dehmelt: *The Uncertain Energy of an Excited State*, Bull. of Am. Phys. Soc. **20**, 637 (1975).

[90] T. W. Hänsch and A. Schawlow: *Opt. Commun. **13**, 68 (1975).*, Opt. Commun. **13** (1), 68-69 (1975).

[91] N. Gisin: *A simple nonlinear dissipative quantum evolution equation*, J. Phys. A: Math. Gen. **14**, 2259-2267 (1981).

[92] R. Wieser: *Comparison of Quantum and Classical Relaxation in Spin Dynamics*, Phys. Rev. Lett. **110**, 147201 (2013).

[93] C. M. Bender and S. Boettcher: *Real Spectra in Non-Hermitian Hamiltonians Having PT-Symmetry*, Phys. Rev. Lett. **80**, 5243(1998).

[94] G. Gamow: *Zur Quantentheorie des Atomkernes*, Z. Physik **51**, 204-212 (1928).

[95] L. Landau: *The Theory of a Fermi Liquid*, Soviet Phys. JETP. **3**, 920 (1957).

[96] B. Penget al.: *Parity-time-symmetric whispering-gallery microcavities* Nature Physics **10** (5), 394-398 (2014).

[97] H. Carmichael: *An Open Systems Approach to Quantum Optics*, **18** (Springer Berlin Heidelberg, 1993)

[98] J. Dalibardet al.: *Wave-function approach to dissipative processes in quantum optics*, Phys. Rev. Lett. **68**, 580 (1992).

[99] K. Molmer et al.: *Monte Carlo wave-function method in quantum optics*, Journ. of Opt. Soc. **10**, 524-538 (1993).

[100] M. B. Plenio and P. L. Knight: *The quantum-jump approach to dissipative dynamics in quantum optics*, Rev. of Mod. Phys. **70** (1), 101-144 (1998).

[101] C. Kittel: *On the Theory of Ferromagnetic Resonance Absorption*, Phys. Rev. **73** (2), 155-161 (1948).

[102] M. Paulsson et al.: *Modeling inelastic phonon scattering in atomic- and molecular-wire junctions* Phys. Rev. B **72**, 201101 (1-4) (2005).

[103] V. Weisskopf and E. Wigner: *Berechnung der natürlichen Linienbreite auf Grund der Diracschen Lichttheorie*, Z. Phys. **63** (1-2), 54-73 (1930).

[104] M. Esposito and F. Haake: *Overdamping by weakly coupled environments*, Phys. Rev. A **72**, 063808 (1-9) (2005).

[105] R. Wieser: *Description of a dissipative quantum spin dynamics with a Landau-Lifshitz/Gilbert like damping and complete derivation of the classical Landau-Lifshitz equation*, Eur. Phys. J. B **88** (77), 1-8 (2015)

[106] G. Redfield: *The Theory of Relaxation Processes*, Adv. Magn. Res. **1**, 1-32 (1965).

[107] D. Werner : *Funktionalanalysis*, Springer (6. edition), Berlin (2007).

[108] W. H. Presset al.: *Numerical recipe* (Press Syndicate of the University of Cambridge, 1988, 1992).

[109] H. Kleinert: *Critical Properties of ϕ^4-Theories*, World Scientific, Singapore (2009).

[110] N.G. Van Kampen: *Stochastic processes in physics and chemistry*, North Holland (3. edition) (2007)

[111] R.R. Howard: *Dynamic Probabilistic Systems, **1**: Markov Chains.*, John Wiley and Sons, New-York (1971)

[112] A.D. Fokker, M. Planck: *Die mittlere Energie rotierender elektrischer Dipole im Strahlungsfeld*, Ann. Phys. **348** (4. Folge 43), 810820 (1914). ; M. Planck: *Über einen Satz der statistischen Dynamik und seine Erweiterung in der Quantentheorie*, Sitz.ber. Preuß. Akad. **24**:324-341 (1917).

[113] J.E. Moyal: *Stochastic processes and statistical physic*, J.R. Stat. Soc. London, Ser. B **11**, 150-210 (1949)

[114] H.A. Kramers: *Brownian motion in a field of force and the diffusion model of chemical reactions*, Physica. **7** (4): 284304 (1940)

[115] W. Walter: *Gewöhnliche Differentialgleichungen: Eine Einführung*, de Gruyter (7.Edition), Boston/Berlin (2010)

[116] K. Ito: *Stochastic integral*, Proc. Imp. Acad. **20**(8), 519-524 (1944).

[117] R.L. Stratonovich: *A New Representation for Stochastic Integrals and Equations.*, SIAM J. Control **4**, 362-371 (1966).

[118] W.F. Brown: *Thermal Fluctuations of a Single-Domain Particle*, Phys. Rev. Lett. **130** (5), 1677-1686 (1963)

[119] W. Pauli: *Über den Zusammenhang des Abschlusses der Elektronengruppen im Atom mit der Komplexstruktur der Spektren*, Zeit. Phys. **31**: 765783 (1925)

[120] H. Brune: *Nanomagnetism: Probing Magnetism at the Nanoscale* Nat. Nanotech. **2** (11): 674 (2007)

[121] R.O. Jones: *Density functional theory: Its origins, rise to prominence, and future*, Rev. Mod. Phys. **87**, 897-923 (2015)

[122] M. Bode et al.: *Chiral magnetic order at surfaces driven by inversion asymmetry*, Nature **447** (7141), 190193 (2007)

[123] J. von Neumann: *Mathematical Foundations of Quantum Mechanics* (1932), Princeton University Press, Princeton (1955)

[124] A. Einstein: *Zur Elektrodynamik bewegter Körper*, Ann. d. Phys. **322** (10), 891-921 (1905)

[125] T. Tania, M. J. de Oliveira: *Dynamic phase transition in the kinetic Ising model under a time-dependent oscillating field*, Phys. Rev. A **41** (8), 4251-4354 (1990)

[126] A. Peres: *Nonlinear variants of Schrödingers equation violate the second law of thermodynamics*, Phys. Rev. Lett. **63**, 1114 (1989).

[127] D. S. Abrahams and S. Lloyd: *Nonlinear Quantum Mechanics Implies Polynomial-Time Solution for NP-Complete and P Problems*, Phys. Rev. Lett. **81** (18), 3992-3995 (1998)

[128] R. Glauber: *Time-Dependent Statistics of the Ising Model*, J. Math. Phys., **4**, 294 (1963).

[129] O. Idigoras, P. Vavassori: *Mean field theory of dynamic phase transitions in ferromagnets*, Physica B **407** (9), 1377-1380 (2012).

[130] Y. Yuksel, E. Vatansever, H. Polat:*Dynamic phase transition properties and hysteretic behavior of a ferrimagnetic coreshell nanoparticle in the presence of a time dependent magnetic field*, J. Phys.: Condens.Matter **24**, 436004 (2012).

[131] A. Berger: *Magnetization reversal in granular thin films*, Physica B **407** (9), 1322-1329 (2012).

[132] O. Hovorka, J. Pressesky, G. Ju, A. Berger, and R. W. Chantrell: *Distribution of switching fields in magnetic granular materials*, Appl. Phys. Lett. **101**, 182405 (2012).

[133] G. Stokes, Katz, Victor J.: *The History of Stokes Theorem*, Mathematics Magazine. **52** (3): 146156 (1979)

[134] T. Holstein, H. Primakoff: *Field Dependence of the Intrinsic Domain Magnetization of a Ferromagnet*, Phys. Rev. **58**, 1098-1113 (1940)

[135] V.L. Safonov: *Micromagnetic grain as a nonlinear oscillator*, J. Magn. Magn. Mater. **195**, 523-529 (1999)

[136] P. Ostborn: *Renormalization of oscillator lattices with disorder*, Phys. Rev. E **79**, 051114 (2009).

[137] Thomas Risler, Jacques Prost, and Frank Jülicher: *Universal critical behavior of noisy coupled oscillators: A renormalization group study*, Phys.Rev. E **72**, 016130 (1-18) (2005).

[138] X. Wang and H. Neal Bertram: *Field and temperature-dependent attempt frequency for dynamic-thermal reversal of interacting magnetic grains*, J. Appl. Phys. **92**, 4560 (2002)

[139] V. L. Ginzburg und L.D. Landau: *"Collected papers"*, Zh. Eksp. Teor. Fiz. **20**, 1064-1082 (1950), Oxford: Pergamon Press 546 (1965)

[140] K. Wilson: *The renormalization group: Critical phenomena and the Kondo problem*, Rev. Mod. Phys. **47** (4), 773-840 (1973).

[141] P. Weiss: *L'hypothèse du champ moléculaire et la propriété ferromagnétique*, J. Phys. Theor. Appl. **6**, 661 (1907).

[142] R. L. Schilling, Lothar Partzsch: *Brownian Motion. An Introduction to Stochastic Processes.*, De Gruyter, Berlin/Boston (2012)

[143] K. Kraus: *States, Effects and Operations: Fundamental Notions of Quantum Theory*, Springer Verlag (1983)

[144] M.-D. Choi: *Linear Algebra and its Applications.*, Elsevier BV. **10** (3): 285290 (1975)

[145] E.C.Stoner, E.P. Wohlfarth: *A mechanism of magnetic hysteresis in heterogeneous alloys*, Phil. Trans. of Roy. Soc. A: Mathematical, Physical and Engineering Sciences. **240** (826): 599642 (1946)

[146] M. Pratzer et al.: *Atomic-Scale Magnetic Domain Walls in Quasi-One-Dimensional Fe Nanostripes*, Phys. Rev. Lett. **87** (12):127201 (1-4) (2001)

[147] W. H. Press, S. A. Teukolsky, W. T. Vetterling and B. P. Flannery: *Numerical Recipes in C. The Art of Scientific Computing.*, Cambridge University Press, 2. Edition, Cambridge and others (1992)

[148] M. Ertas, B. Deviren, M. Keskin: *Dynamic phase transitions and dynamic phase diagrams of the spin-2 BlumeCapel model under an oscillating magnetic field within the effective-field theory*, J. Magn. Magn. Mater. **324**, 704-710 (2012).

[149] D. Werner, *Funktionalanalysis.*, Springer, 7.Edition, Berlin (2011)

[150] M.A. Ruderman; C. Kittel: *Indirect Exchange Coupling of Nuclear Magnetic Moments by Conduction Electrons* Physical Review. **96**: 99 (1954); T. Kasuya: *A Theory of Metallic Ferro- and Antiferromagnetism on Zener's Model*, Prog. of Theor. Phys. **16**: 45-57 (1956) and K. Yosida: *Magnetic Properties of Cu-Mn Alloys* , Phys. Rev. **106** (5): 893-898 (1957)

[151] H. Tutu and N. Fujiwara: *Landau Theory of Dynamic Phase Transitions and Systematic Perturbation Expansion Method for Getting Phase Diagrams*, J. Phys. Soc. Jpn. **73**, 2680-2696 (2004).

[152] R. Kikuchi: *On the Minimum of Magnetization Reversal Time*, J. of Appl. Phys. **27** (11), 1352-1357 (1956)

[153] W. Rudin: *Functional analysis.*, McGraw-Hill Science/Engineering/Math., 2. Edition (1991)

[154] W. H. Press, S. A. Teukolsky, W. T. Vetterling and B. P. Flannery.: *Numerical Recipes in C++. The Art of Scientific Computing.*, Cambridge University Press (2. Edition), Cambridge (2002)

[155] L. Diósi. *Nonlinear Schrödinger equation in foundations: summary of 4 catchesNonlinear Schrödinger equation in foundations: summary of 4 catches*, J. Phys.: Conf. Ser. **701** 012019 (2016)

[156] *HAMR Technology*, **url**: https://www.seagate.com/www-content/ti-dm/tech-insights/en-us/docs/TP707-1-1712US$HAMR.pdf$ (Technology Paper), retrieved Jan. 2020

Eidesstatliche Versicherung/Declaration on oath

Hiermit versichere ich an Eides statt, die vorliegende Dissertationsschrift selbst verfasst und keine anderen als die angegebenen Hilfsmittel und Quellen benutzt zu haben.

Hamburg, den 28.11.2021

Danksagung (acknowledgment)

I want to conclude this thesis by saying thank you to a couple of people.

First of all, I'd like to thank Prof. Dr. Roland Wiesendanger for giving me the opportunity to work in his group for several years, for supporting my Ph.D. project during that time and for participating in the "Prüfungskommission" for my disputation.

I'd like to express enormous gratitude towards PD Dr. Elena Vedmedenko for unconditional support of my work, including considerable patience despite several setbacks and various forms of good advice during the supervision of my Ph.D. project and for reviewing my Ph.D. thesis as a referee.

Special thanks go to Prof. Dr. Alexander Lichtenstein for accepting my request to review my Ph.D. thesis as a second referee.

I'd like to thank Dr. Thore Posske for his participation as a member of the "Prüfungskommission" and for improving the overall quality of this manuscript through helpful advice.

Also, I feel grateful towards Prof. Dr. Günter Sigl for participating in the "Prüfungskommission" and for being its chairman.

In particular, I'd like to thank former colleague Dr. Mario Krizanac for fruitful collaborations and vital discussions concerning physics, science and beyond.

I also want to thank Dr. André Kubetzka, M.Sc. Alexander Schäffer, Dr. Levente Rósza, Dr. Julian Hagemeister and M.Sc. Jannis Neuhaus for some helpful and stimulating discussions.

Finally, I want to give the highest appreciation to my family and friends for great moral and emotional support during the entire period of my Ph.D. work.